SAMPLE SAVING TECHNIQUES FOR SOLUTION X-RAY SCATTERING STUDIES OF BIOLOGICAL MACROMOLECULES

A Dissertation

Presented to the Faculty of the Graduate School

Of Cornell University

In Partial Fulfillment of the Requirements for the Degree of

Doctor of Philosophy

by

Andrea Michelle Katz

August 2018

SAMPLE SAVING TECHNIQUES FOR SOLUTION X-RAY SCATTERING STUDIES OF BIOLOGICAL MACROMOLECULES

Andrea Michelle Katz, Ph. D.

Cornell University 2018

Small-angle X-ray scattering (SAXS) provides structural information about biomolecules in solution. The resulting insight increases our understanding of biological processes and can aid in structure-based drug design. However, SAXS experiments require tens of microliters of sample at mg/mL concentrations, making the technique unsuitable for molecules that cannot be produced in large quantity. This dissertation introduces three new techniques for sample efficient SAXS experiments.

The first details the fabrication and use of fixed path length sample cells for cryoSAXS experiments, as well as their challenges. The cells have rigid walls with low scatter and high X-ray transmission, and allow SAXS measurements from less than two microliters of sample. Although fractures in the vitrified samples produce irreproducible scatter at the lowest angles, the technique is robust and applicable to molecules with maximum dimension less than ~160 Å.

The second method implements a coaxial, continuous flow diffusive mixer for low sample volume time-resolved SAXS on the 10 ms - 3 s timescale. The mixer's geometry allows the use of a larger, higher flux beam than is compatible with most continuous flow SAXS mixers, shortening the acquisition time and reducing sample consumption. A custom beamline setup reduces background scatter to further improve data quality. Each measurement uses less sample than a conventional static SAXS experiment. A study of RNA folding initiated by Mg^{2+} is presented as an example of the utility of this technique.

The final method employs a chaotic advection mixer for time-resolved SAXS measurements on slowly diffusing systems. This device incorporates a miniaturized static mixer to efficiently mix

two liquids in the laminar flow regime. An improved beamline setup delivers a higher flux beam than can be used with the diffusive mixer, minimizing acquisition time and sample consumption. This mixer uses an order of magnitude less sample than turbulent flow SAXS mixers, and about twice the sample needed for a conventional static SAXS measurement. Time-resolved SAXS measurements of the binding of trypsin and aprotinin, a well-studied protein pair, are presented as a proof of principle.

BIOGRAPHICAL SKETCH

Andrea Katz was born in Arlington, Texas to Andy and Lynda Katz. Her passion for science began in eighth grade, when her teacher assigned a report on a constellation. She climbed up onto her roof to get a better view of Canis Major, and was instantly hooked on astronomy. In high school, she worked at the planetarium at the Fort Worth Museum of Science and History and helped out at public star parties. She attended Trinity University, where she studied Physics and Astronomy. Under the guidance of Dr. Gordon MacAlpine, she undertook a research project mapping the carbon abundance in the Crab Nebula, and even got to go on an observing trip to MDM Observatory on Kitt Peak. During her final summer at Trinity, Andrea did an REU at the University of Washington, where she worked with Dr. Boris Blinov's quantum computing group. Here, she discovered a love for working with her hands and building components of the experiment herself. This inspired her to switch directions, and after graduating from Trinity in 2011, she came to Cornell's Applied Physics department for graduate studies. She joined Dr. Lois Pollack's research group, where she has had wonderful opportunities to develop new methods and instrumentation to study interesting, important biological molecules. Andrea loves Ithaca, and when not in the lab, she can be found hiking in the gorges, cross country skiing, or playing fiddle on The Commons for summer contra dances.

To my family

ACKNOWLEDGEMENTS

First and foremost, I would like to thank my advisor, Lois Pollack, who has been a fantastic mentor, advisor, and friend to me throughout my time here. I am grateful for her wise guidance and perpetual optimism even in the face of great challenges. Working with her has made me not only a better scientist, but a better person.

I sincerely thank the Pollack Lab members that I have overlapped with during my time at Cornell: Suzette Pabit, Steve Meisburger, Josh Blose, Chris Jones, Huimin Chen, Yujie Chen, Josh Tokuda, Julie Sutton, George Calvey, Alex Plumridge, Alex Mauney, Jose San Emeterio, Yen-Lin Chen, and Derrick Lin. All of them contributed to interesting and valuable discussions about the projects I worked on, and provided support and friendship to make my time here at Cornell wonderful. Yujie spent countless patient hours teaching me to pipette and work with biomolecules. Suzette and Steve taught me how to do SAXS experiments and set up a beamline. Suzette and Alex P are sample wizards and contributed many mL of molecules for study in the new methods described here. George, my partner both in and out of the lab, taught me most of what I know about engineering and design, was always willing to help me work through difficult concepts, and spent hours designing and building all sorts of cool new instrumentation with me.

I have been fortunate to have many great collaborators during my time here. Many thanks to Jesse Hopkins, who worked on cryoSAXS methods development with me during the first half of my graduate career. I learned a lot from his expertise with cryocooling, clever uses of the ring clamp, and gentle sense of humor. Matt Warkentin and Rob Thorne also contributed experimental help and lots of useful advice for the cryoSAXS project. Robb Welty, from Washington University, made the rRNA samples for the diffusive mixing experiment. I am grateful to Juraj Knoska, from CFEL, for making the 3D printed chaotic advection inserts, for good advice on mixer design, and for friendship and help with several XFEL beamtimes!

I would also like to thank Sol Gruner and Harold Craighead for their advice, for serving on my committee, and for their critical reading of this manuscript.

Most of my graduate research has been supported by the National Science Foundation, through grants DBI-1152348 (CryoSAXS), 123136 (BioXFEL STC), and DGE-1144153 (Graduate Research Fellowship Program). The RNA folding projects described in Chapter 4 were supported by the National Institutes of Health, through RO1-GM085062. The NIH also supported my early graduate work on nucleic acid condensation through R01-GM099450 and R01-GM076121.

This work made use of several Cornell shared facilities, all of which were essential to the success of my project. All SAXS experiments were carried out at the Cornell High Energy Synchrotron Source (CHESS), which is supported by the NSF award DMR-1332208. We also received much assistance from MacCHESS, which is supported by NIGMS award GM-103485. None of these measurements could have been carried out without staff scientists Arthur Woll and Richard Gillilan. Their hard work helping with beamline setup, SPEC issues, and equipment troubles is greatly appreciated. Richard also supplied some of the essential equipment for the chaotic advection mixer experiment, including KF bellows, a fast switching valve, and pieces of the vacuum chamber.

The cryoSAXS sample cells were partially fabricated at the Cornell NanoScale Facility (CNF), an NNCI member supported by NSF Grant ECCS-1542081. CNF staff Rob Ilic, Daron Westly, and Mike Skvarla helped with etch recipes and cleaning procedures, and provided lots of useful advice. The capillaries used to make the microfluidic mixers and the single crystal X-ray slit blades were polished on a wheel owned by the Cornell Center for Materials Research, which is supported by the National Science Foundation under Award Number DMR-1120296.

All of the machined parts described in this dissertation were made by George Calvey and me in the LASSP student machine shop. I could not have done any of the work described here without the

help of shop advisor Nathan Ellis. His patient teaching helped me learn to machine things I never dreamed I could make, and his jovial manner always brightened my day.

I would also like to thank all of the scientists who supported me as I grew up and guided me to where I am today: Eighth grade teacher Lois Dean, whose constellation project started me on this journey. High school physics teacher Jay Atman, whose excruciatingly difficult homework assignments taught me how to think and who allowed an astronomy-mad freshman to join physics club, which was really only for juniors and seniors. Fort Worth Astronomical Society presidents Harry Bearman and Trista Opperman, and planetarium director Linda Krouse, who taught me to use my telescope and allowed me to feel engaged in science from the time I was 14. Gordon MacAlpine, my undergraduate research advisor, who took on an entire extra section of Physics 101 my freshman year just so that I could take the class, worked closely with me on Crab Nebula research, and shared lots of great advice on science and life. Trinity physics professor Dennis Ugolini, who was a great mentor for me and taught me how to write like a physicist. Fellow physics student and good friend Megan Holtz, who not only helped me with my classwork but also made both Trinity and Cornell a great experience. I am glad I followed her to Cornell AEP!

Special thanks to my parents, Andy and Lynda, whose love and support made this whole journey possible. They encouraged me every step of the way, from the Bathtub Science Experiments book that we worked through when I was small to the 16” diameter telescope that Dad and I built in our garage. I would not have made it here without them. Thanks to the Calvey and Morris families, who have taken me in and given me a wonderful extended family. And especially thanks to George, who makes every day amazing no matter how mundane. I am so glad I’ve been able to share my time at Cornell with him, and I look forward to wherever life takes us.

TABLE OF CONTENTS

LIST OF FIGURES

LIST OF TABLES

CHAPTER 1

INTRODUCTION

1.1 Biological motivation

All biological functions necessary for life have their roots in processes carried out by ~nm size macromolecules such as proteins and nucleic acids [1]. These tiny molecular machines fill roles ranging from defense against foreign particles, to signaling across cell membranes, to regulation of metabolism. Knowledge of how these molecules function can give insight into countless biological processes and lead to better treatment and prevention of disease.

The field of structural biology uses the relationship between molecular structure and function to gain insight into how biological macromolecules carry out their roles. Structural details can help biologists fine-tune their understanding of a known biological process or can provide the first clues into how function is carried out [1]. For example, before Watson's and Crick's famous proposal of DNA's double helical structure, it was known that DNA was a source of genetic information, but the mechanism of storage and transcription were uncertain. From the double helical structure, Watson and Crick were able to infer how genetic material could be stored and copied [2].

1.2 Techniques for determination of high resolution molecular structures

Many techniques exist for determining the structure of biological macromolecules with high resolution. While these are not explored in this work, a brief explanation is necessary for context. Medium to high-resolution structural techniques include X-ray crystallography, electron microscopy, nuclear magnetic resonance, and solution scattering. The most prolific of structural techniques is X-ray crystallography, with over 100,000 structures deposited in the Protein Data Bank [3]. X-ray

diffraction from a crystal of macromolecules can be inverted to give an atomically detailed picture of 3-D molecular structure, molecular interactions, and even the structure of water [4]. However, it is challenging to grow crystals that diffract to high resolution, and membrane proteins in particular are difficult to crystalize. Additionally, molecules within a crystal can only sample a portion of their conformational space, and the crystallization conditions and crystal contacts may bias the molecules' structure [5]. Therefore, while crystallography provides a wealth of structural information, complementary solution-based techniques are needed to visualize the structures of molecules that are difficult to crystalize, as well as to guarantee an accurate structure from a crystallized molecule.

Cryo-electron microscopy and nuclear magnetic resonance provide high resolution characterization of the structure of biological molecules in solution. In cryo-electron microscopy, a thin film of solution containing the molecule of interest is rapidly frozen and probed with an electron beam. Due to the weak signal from a single molecule, many thousands of images of molecules in random orientations are combined during post processing to form a structure. While the method is rapidly growing and can successfully solve the structure of complex particles such as the ribosome with bound tRNA [6], it is currently limited to large particles (>200 kDa), and structures are less accurate than those obtained with crystallography [7].

Nuclear Magnetic Resonance (NMR) spectroscopy is another solution technique that reveals average inter-atomic distances and bond angles [8]. However, data collection is slow and sample consumption is high, and due to the difficulty in data analysis, application of NMR methods are limited to relatively small molecules (<50 kDa) [9]. The result is that the number of published structures solved by NMR has stagnated relative to the number solved by crystallography [10]. Therefore, while NMR and cryo-electron microscopy can provide high resolution structures of biomolecules in solution, a different kind of technique is necessary to avoid limitations introduced by molecule size and difficult data analysis.

1.3 Introducing SAXS, a powerful, low resolution structural technique

Small Angle X-ray Scattering (SAXS) provides low resolution information about the structure of molecules in solution. While it does not give atomically detailed structures like the techniques listed above, SAXS provides insight into overall molecule size and shape [11]. It can probe molecules and complexes with sizes ranging from a few kDa to GDa [12], and can give insight into molecular folding studies [13], interactions between ions and biomolecules [14], and flexible or disordered molecules [12]. Sample preparation, experimental setup, data acquisition and analysis are all relatively straightforward. Additionally, due to the solution nature of the samples and rapid data collection, SAXS lends itself to time-resolved studies, which track the structure of a molecule as it functions [15]–[17]. Therefore, even with its limited spatial resolution, SAXS is a powerful structural technique.

Like other structural techniques, SAXS has its challenges. SAXS samples are susceptible to radiation damage [18]. To avoid this, it is often necessary to flow the sample through the x-ray beam, reducing the radiation dose that each individual molecule experiences [19]. This increases sample consumption to ~30 µL, which can be prohibitive for some molecules. With time-resolved SAXS experiments, the sample requirements can be even greater: stopped flow measurements require at least 600 µL per shot [20]! Additionally, the short acquisition times and thin sample streams generally required for time-resolved SAXS result in noisy data.

The goal of this thesis is to introduce new instrumentation and methodology for performing SAXS experiments with low sample volume, high signal-to-noise data, and vastly reduced radiation damage. Chapter 2 provides a formulation of SAXS theory and a more detailed discussion of what information SAXS gives us, along with the challenges it presents. Chapter 3 focuses on new instrumentation developed to perform SAXS experiments on frozen samples (cryoSAXS). Chapter 4 describes a new mixer and beamline setup for continuous flow time-resolved SAXS, and presents data on two RNA systems. Chapter 5 moves on to a chaotic advection SAXS mixer for viscous samples or large molecules, and includes results from a protein pair binding study.

CHAPTER 2

SMALL-ANGLE X-RAY SCATTERING

2.1 What is SAXS?

2.1.1 In a nutshell…

Small-angle X-ray scattering (SAXS) is a low resolution structural technique used to study molecules in solution. In a SAXS experiment, an aqueous solution of biomolecules is bombarded by a collimated beam of X-rays. The biomolecules scatter the photons, which are recorded with an area detector. Measurement of the scattered intensity as a function of scattering angle provides information about the general size and shape of the molecule, its overall level of compactness, and its interactions with neighboring molecules [11]. While it does not provide the atomic level structural detail obtainable from techniques like X-ray crystallography, the solution nature of the sample provides an opportunity to study molecules at different buffer conditions and sample concentrations, elucidating information about structure-function relationships under these different circumstances [21]. It also lends itself to studying the time-dependent structures of molecules as they perform their functions [17], and can be used to validate molecular models.

2.1.2 X-ray sources for SAXS experiments

SAXS experiments can be performed using small X-ray sources such as rotating anodes. Improved anode sources, X-ray optics and detectors [22], [23], and complete commercial in-house systems such as the Bruker NanoSTAR or the Rigaku BioSAXS 2000 make SAXS an increasingly accessible in-lab technique. However, due to the relatively weak flux of home sources, high throughput SAXS experiments must be performed at high brightness synchrotron X-ray sources.

Synchrotron sources have orders of magnitude more X-ray flux (10^{13} ph/s on some synchrotron SAXS beamlines [24], [25] versus 10^{6}-10^{7} ph/s at home sources [23], [26]). Therefore, high signal-to-noise data can be collected in a much shorter amount of time at a synchrotron source. A sample that requires a full day of illumination at a home source can be measured in seconds at a synchrotron [23]. Therefore, despite the greater availability of home sources, most SAXS experiments rely on synchrotron radiation [11]. Almost every major synchrotron facility has a beamline dedicated to SAXS experiments on biological molecules [27].

2.1.3 Experimental setup and procedure

A schematic of a typical SAXS setup is shown in Figure 1. X-rays from the source are incident on a highly absorbing aperture, which defines the beam size to be used for the experiment. This aperture can take the form of either a pinhole or two crossed slits, and is usually made from tungsten or tantalum due to their high X-ray attenuation [28]. Because this aperture by definition clips the beam, it produces parasitic scatter, which must be removed by a second aperture. This guard aperture reduces the beamline's background and is necessary for high signal-to-noise data. Recently, "scatterless" slits and pinholes made of single crystal silicon, germanium, or tantalum have been used as the beam defining aperture to reduce parasitic scatter and the need for guard slits ([28], scatterless slits available from Xenocs SAS, Sassenage, France, scatterless pinholes from Incoatec GmbH, Geesthacht, Germany).

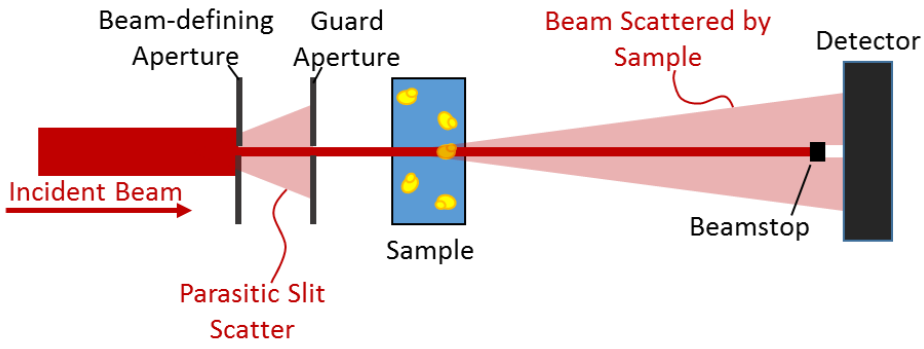

Figure 1. Schematic of beamline setup for a typical SAXS experiment.

After passing through the apertures, the X-rays are incident upon the sample, a solution of biological molecules. The sample is most often held in a cell made of extremely thin walled glass or polyimide, which have low X-ray attenuation. Photons scattered by the sample are recorded on a 2D area detector. The majority of the beam passes directly through the sample and encounters a beamstop. This can be made of either a lead-backed pin diode or a semitransparent material such as a molybdenum foil. In either form, the beamstop provides a way to measure the transmitted intensity over the course of each image without overexposing the detector with direct beam. The entire length of the X-ray flight path, from upstream of the beam defining aperture to the detector, can be under vacuum to reduce the background scatter.

In a SAXS experiment, only the scatter from the biomolecules is of interest. However, scatter is also produced by the guard aperture, the sample cell walls, and even the solvent that the molecules are in. It is therefore necessary to measure the background scatter to subtract out these unwanted components and obtain only the scatter from the molecules. Figure 2 illustrates this process.

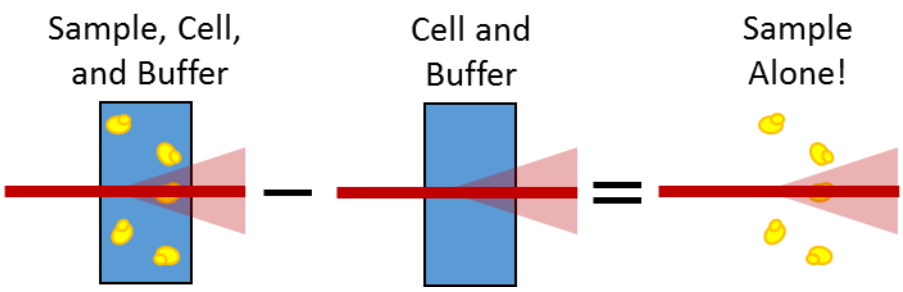

Figure 2. Illustration of the principle of background subtraction for SAXS experiments.

A robust SAXS procedure consists of the acquisition of background scattering profiles immediately before and after acquiring the scattering profile of the molecule-containing solution. Comparison of the pre-and-post background images, which should agree precisely, provides a way to diagnose whether there are issues such as beam drift or sample cell contamination that could produce a misleading scattering profile.

2.2 Using SAXS to study biological molecules

2.2.1 Basic mathematical formulation

A cartoon of X-ray scattering at the molecular level is shown in Figure 3. When the electrons within a molecule are excited by the electric field of an incident X-ray beam, they reradiate a spherical wave [14]. To compute the amplitude of this scattered wave, we must consider the phase differences between all waves scattered in the same direction. This direction is characterized by the scattering angle, 2θ, or by the momentum transfer between the X-ray and molecule, **q**, which is related to the scattering angle according to

$$|\boldsymbol{q}| = q = \frac{4\pi sin\theta}{\lambda} \quad (1)$$

where λ is the wavelength of the X-rays. For the small angles of interest in this work, $q \propto \theta$.

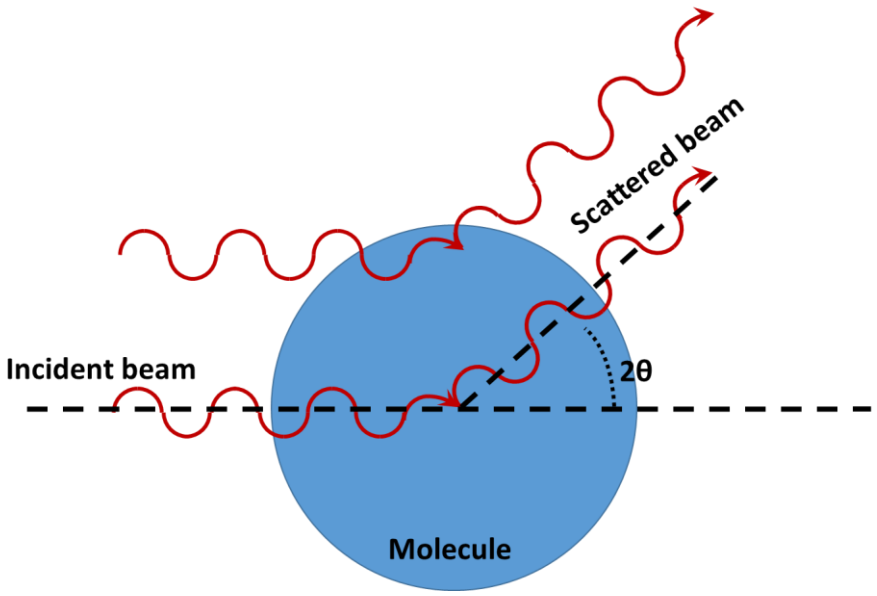

Figure 3. Schematic of X-rays hitting a molecule. Interaction between the molecule and the beam results in scattered photons.

Each atom in the molecule has a scattering factor, $f(\boldsymbol{q})$. If we consider our molecule to be a cluster of N atoms, the total scattering amplitude $F(\boldsymbol{q})$ has the following form [14], [29]:

$$F(\boldsymbol{q}) = \sum_{n=1}^{N} e^{i\boldsymbol{q}\cdot\boldsymbol{r}_n} f_n(\boldsymbol{q}) \tag{2}$$

Here, $\boldsymbol{r}_n$ is the position of the nth atom in the molecule.

Experimentally, we cannot measure the scattering amplitude, but rather the scattered intensity:

$$I(\boldsymbol{q}) = F(\boldsymbol{q})F^*(\boldsymbol{q}) = \sum_{n=1}^{N}\sum_{m=1}^{N} e^{i\boldsymbol{q}\cdot\boldsymbol{r}_{nm}} \mathrm{f_n}(\mathbf{q})\mathrm{f_m}(\mathbf{q}) \tag{3}$$

where $\boldsymbol{r}_{nm} = \boldsymbol{r}_n - \boldsymbol{r}_m$ is the distance between the mth and nth atom.

Because SAXS is a bulk solution method, the molecules in a sample are free to rotate and will at any given time represent all possible rotational orientations [29]. Therefore, what we actually observe is the spherical average of the intensity:

$$< I(q) > \propto \sum_{n=1}^{N} \sum_{m=1}^{N} f_n(q) f_m(q) \, {\sin qr_{nm}}/{qr_{nm}} \quad (4)$$

In practice, scattered photons recorded on the detector are added up in rings around the incident beam (with increasing radius corresponding to increasing q) to form a plot of integrated intensity as a function of q. The resulting 1-D plot is referred to as a scattering profile.

Scattering profiles provide information about the global size, shape, and compactness of the biomolecule, as detailed below. Figure 4a) shows example scattering profiles for a small RNA molecule before and after mixing with magnesium, which folds the molecule to a compact state [30].

2.2.2 Basic interpretation of scattering profiles

Because the scattering amplitude is the Fourier transform of the electron density distribution, most of the scattered radiation from a molecule of size d occurs at angles smaller than $q = \pi \backslash d$ [11]. Therefore, if a SAXS experiment collects data out to a maximum angle of q_{max}, that data provides information about the molecule with distance resolution equal to $\pi \backslash q_{max}$. Scattering intensities from molecules in solution decay rapidly with angle, and therefore only low resolution information is available [11].

Despite this low resolution, SAXS has much to tell us much about the size, shape, and compactness of the molecule of interest. For example, the scattering at the very lowest angles provides a measure of the radius of gyration, R_g, which is the mean square distance between all pairs of electrons in the molecule. For very low scattering angles ($q < 1.3/R_g$), the scattered intensity can be approximated by a Gaussian form [14]:

$$< I(q) > = I_0 e^{-q^2 R_g^2/3} \quad (5)$$

where I_0 is the scattering in the forward direction ($q = 0$). For monodisperse, noninteracting systems, a plot of $ln < I(q) >$ versus q^2 is linear and has a slope that is proportional to R_g^2. This is called a Guinier plot, and provides the R_g even if the molecular weight is unknown [29]. This parameter provides information about folding and compaction, and can be used to select plausible models for the molecule. Guinier plots are also useful as indications of interparticle interactions in the sample: a Guinier plot that trends upwards at low q suggests aggregation, while a low q downturn in a Guinier plot is a sign of intermolecular repulsion [11], [31]. Figure 4b) shows Guinier plots for the example rRNA system.

While the R_g measures the molecule's overall size, I_0 holds information about the molecular weight, since it is proportional to the total number of particles illuminated at once. It is possible to calculate the molecular weight of the sample from I_0 by applying an absolute calibration derived from a comparison of the theoretical and experimental scattering of water [31]; however, this result is only meaningful for ideal, noninteracting samples (with a linear Guinier plot). Changes in I_0 accompany sample aggregation and association [32], with I_0 doubling when a sample transitions from monomers to dimers. It is important to note that I_0 cannot be directly measured, due to overlap with the incident (unscattered) beam, and must be extrapolated from the observed low angle scatter.

The higher angle portions of the scattering curve (beyond the Guinier region) contain additional information about molecular structure. A common approach in folding studies is to create a Kratky plot of $I(q)q^2$ vs. q. Such a plot emphasizes features reflected in the higher angle data. Kratky plots of folded, compact molecules display a peak in the mid-q region, while unfolded or disordered

molecules have Kratky plots with less pronounced or non-existent peaks [14], [33]. Figure 4c) shows example Kratky plots for rRNA.

Another, more intuitive way to interpret SAXS data is use a Fourier transform to convert the scattered intensity into back into real space information. Because we measure the spherically averaged intensity, we cannot compute the actual electron density distribution of the molecule from its scattering profile. Instead, we obtain the pair distance distribution function, P(r), which is spherically averaged and describes the relative distribution of the interatomic distances present [31]. It is sensitive to the molecular shape, with shapes such as spheres and rods having drastically different P(r) functions [11]. The P(r) function also provides another means to measure the R_g, which is often more accurate than the Guinier method since it uses the entire curve [31]:

$$R_g{}^2 = \frac{\int P(r) r^2 dr}{2 \int P(r) dr} \tag{6}$$

Figure 4d) shows P(r) plots for rRNA.

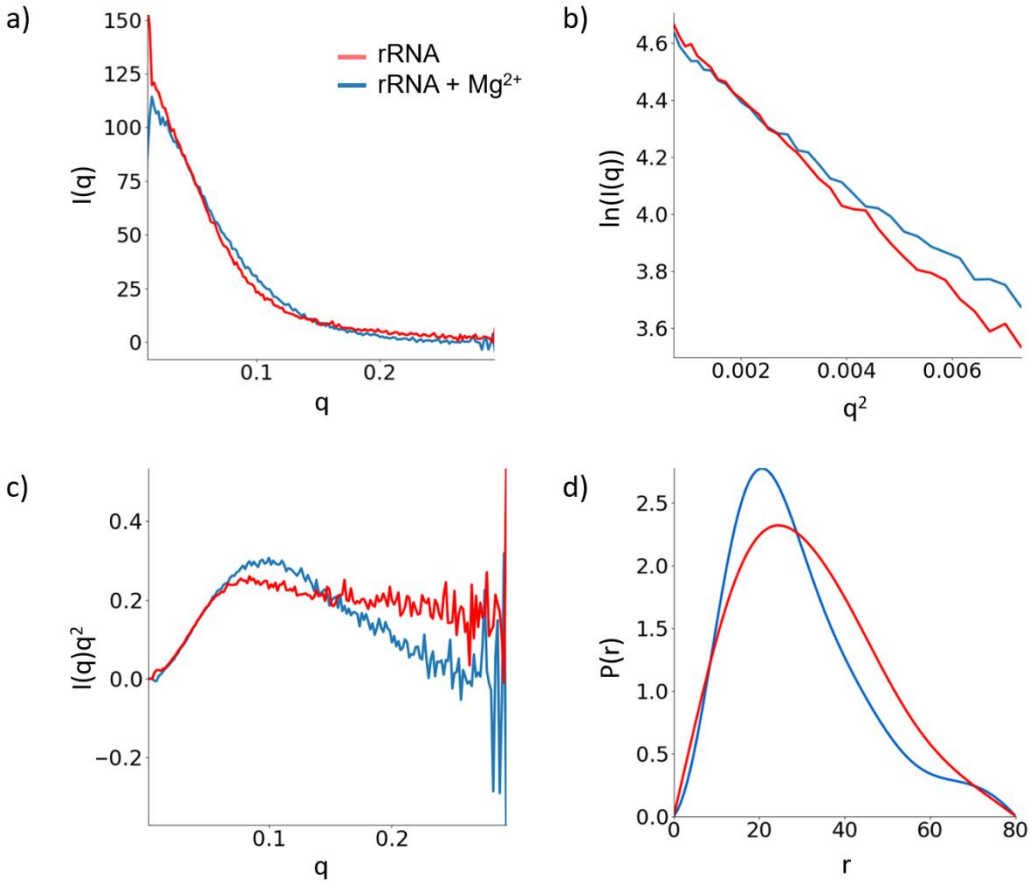

Figure 4. Example of basic SAXS data interpretation for rRNA, both before and 300 ms after mixing with Mg^{2+} (unpublished data). a) Scattering profiles for both states. The significantly different shapes of the profiles reflect large scale structural changes in the molecule. The non-Gaussian shape of the profiles at the very lowest q is the result of parasitic scatter from the apertures and sample cell used in the experiment. b) Guinier plots derived from the profiles in a). The shallower slope of the line for the post-mixing sample suggests a smaller radius of gyration. c) Kratky plots for the same molecules. Before mixing, the rRNA is unfolded, as shown by the absence of a mid q peak. After mixing, the rRNA becomes more compact. d) Radial distance distribution plots show a shift towards shorter length vectors after mixing.

2.2.3 Reconstructing a 3-D structure from a 1-D SAXS profile

In addition to the parameters that can be extracted from the basic scattering profile, many algorithms can be used to reconstruct low resolution 3-D structures from 1-D scattering profiles [34]. The first of these methods represented the scattering profile as a spherical harmonic expansion of the molecular surface [34], [35]. Determining the coefficients of the harmonics through least-squares

fitting procedures gives insight into the molecule's shape. However, this technique can only be applied to molecules whose shape closely resembles a sphere, and cannot be used to study extended molecules or those with multiple domains or cavities [34].

Scattering data can also be fit using models in which the molecule's electron density is approximated by a cluster of beads. The fit can be accomplished using various Monte Carlo-like procedures. Dalai GA2 [36], [37] uses a genetic algorithm, while the popular DAMMIN and DAMMIF programs utilize simulated annealing and a compactness criterion [38], [39]. An example of a reconstruction using DAMMIF is shown in Figure 5.

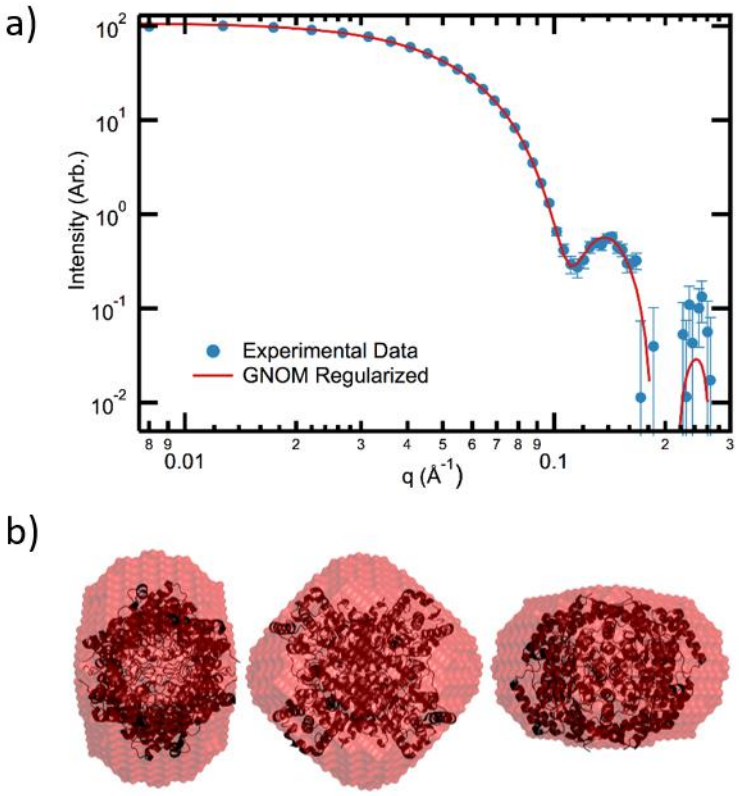

Figure 5. Example of SAXS reconstructions. a) Measured (blue) and fit (red) scattering profile for a standard SAXS protein, Glucose Isomerase. b) 3-D structures calculated by DAMMIF (red) superimposed over the molecule's crystal structure (black) from PDB 1xib [40]. Figure adapted from Hopkins, Katz, et al. [41].

When using any of these methods to reconstruct a 3-D structure from 1-D SAXS data, it is important to remember that such a reconstruction will never be unique. Careful analysis requires the comparison of many different reconstructions from the same profile to identify "structural partners" which have different shapes but produce the same scattering profile [34]. Reconstructions also fail to capture the structural ensembles that exist during a time-resolved experiment [42] or for a disordered or flexible molecule. In these cases, the reconstruction reflects the average state of the molecules.

2.2.4 Reconstructing a SAXS profile from a structural model

It is also possible to create a SAXS profile from an existing structural model and compare this simulated profile to experimental data [21]. While this method cannot conclusively validate a model, it can prove a model incorrect or incomplete, and aid in refinement [31]. Several SAXS profile reconstruction methods exist. Perhaps the most popular is CRYSOL, which computes a simulated SAXS profile from atomic coordinates while accounting for the hydration layer around the molecule [43].

2.2.5 Ensemble modeling

One of the strengths of SAXS as a solution method is the ability to study flexible or disordered molecules, or systems that are evolving with time. With these samples, an ensemble of structural conformations is present at any given time. Standard 3-D reconstructions fail to represent such a system, and instead only reflect the average structure [42]. Therefore, an ensemble approach is needed to capture the variety of states present in a sample of disordered or flexible molecules.

In the Ensemble Optimization Method (EOM), the experimental SAXS profile is assumed to arise from the average of an unknown number of different structures all present within the sample [12], [44]. First, a large number of structural conformer models are generated. A genetic algorithm selects

a subset of the models whose computed scattering profiles (generated with CRYSOL) best recapitulate the data [44]. This technique can provide numerous insights into flexible systems not attainable through routine 3-D reconstructions. For example, it has been used to detect inter-domain motions in proteins, which play important functional roles but are hard to observe with other techniques [44].

2.3 Challenges Associated with SAXS

2.3.1 Radiation damage leads to high sample consumption

One of the greatest challenges in a SAXS experiment is the need for monodisperse samples free of aggregation [31], [45]. Radiation damage can cause aggregation, unfolding, and fragmentation [18], and is therefore a critical issue for SAXS. X-rays with the energies and intensities used in synchrotron SAXS experiments react with water molecules to produce free hydroxyl and hydroperoxl radicals that attach to the biomolecules in the sample [18], [46]. The radical-activated molecules can aggregate by covalent or non-covalent bonds [18], [47]. This aggregation distorts the profile and thus prevents the determination of accurate structural parameters from SAXS data.

Many strategies exist to reduce radiation damage. Different biomolecules show a variety of modes and rates of damage [48], so damage prevention efforts must be carefully tested and tailored on a case-by-case basis. Small molecules such as glycerol or DTT act as radical scavengers or influence long range protein-protein interactions and can be added to the buffer to reduce damage [18], [31]. In cases where these additions are incompatible with the sample or fail to eliminate radiation damage, the beam can be attenuated or defocused, though this results in a lower scattering intensity and overall loss of data quality [46]. Cryocooling the samples greatly reduces radiation damage [45] but increases the experimental difficulty (this new method, cryoSAXS, is thoroughly discussed in Chapter 3).

The most common solution to prevent radiation damage is to increase the irradiated sample volume so that each individual molecule receives a lower X-ray dose. This is accomplished by either flowing or translating the sample through the beam [46], [49], [50]. These strategies require relatively large sample volumes, between 10 and 30 μL depending on the setup [19], [49], [50]. Therefore, while flowing or translating the sample does effectively reduce radiation damage, the large volumes required can preclude the study of expensive samples or those that are difficult to produce in large quantities.

2.3.2 Time-resolved SAXS requires even more sample volume for high signal-to-noise data

Most time-resolved SAXS experiments rely on either stopped-flow or continuous flow mixers [51]. In a stopped-flow experiment, two or more solutions are rapidly mixed and injected into an observation chamber. The flow is stopped, holding the sample within the chamber, and measurements are acquired as the mixture evolves in time. To obtain high time resolution at short time points, extremely short X-ray exposure times are required. These are by nature very noisy, so the experiment must be repeated many times, and the frames with corresponding times from each run averaged to produce a high signal-to-noise scattering profile. Since stopped-flow mixers use hundreds of microliters of sample per shot [20], this process quickly becomes very sample-expensive. The signal-to-noise problem also persists at long time-points, when radiation damage to the stationary sample becomes a problem. It is necessary to attenuate the X-ray beam, reducing the data's signal strength.

In a continuous flow mixing experiment, two solutions are rapidly mixed, then travel a set delay length over which the reaction progresses before encountering the X-ray beam. These devices can mix by diffusion or with turbulence. Diffusive mixers operate at low sample flow rates, but a very thin ribbon of sample is required for rapid diffusion. Therefore, a very small X-ray beam is needed to maintain low background [16], and long acquisition times are necessary for high signal-to-noise data [42]. Sample volumes quickly add up even at low flow rates, especially when measuring many time points. Turbulent mixers eliminate the need for the small sample thickness and produce higher signal-

to-noise data, but require high sample flows to mix efficiently. Recent advances have significantly reduced the sample volume consumed by a turbulent SAXS mixer to 2-3 mg of sample per time point [52]. However, this is still an order of magnitude more than used for a static SAXS sample.

This thesis addresses the challenges discussed above by presenting three new methods that enable high signal-to-noise SAXS data acquisition with reduced radiation damage and low sample consumption.

CHAPTER 3

CRYOSAXS: ULTRA LOW VOLUME EXPERIMENTS ON VITRIFIED SAMPLES

The work in this chapter was carried out in close collaboration with Jesse Hopkins. Much of this chapter is closely based on Ref [41].

3.1 Motivation and background

As described in Chapter 2, radiation damage is a challenge associated with SAXS experiments, and can cause aggregation, unfolding, and fragmentation of the biomolecules in the sample. The relatively high energy, high flux X-ray beams used for synchrotron SAXS (~10 keV, 10^{12} ph/s) react with water molecules in the sample to produce free hydroxyl and hydroperoxl radicals that can attach to the biomolecules [18], [46]. Once radical-activated, the biomolecules can aggregate via covalent or non-covalent bonds [18], [47]. The SAXS profile from an aggregated sample is different from the profile obtained from a monodisperse sample of the same biomolecules. Therefore, SAXS data from damaged samples gives misleading structural information, so avoiding radiation damage is essential for any SAXS experiment.

A common, successful strategy to avoid damage is to spread out the radiation dose by continuously flowing or oscillating samples through the beam. However, the resulting large sample volumes prohibit SAXS studies of molecules that are expensive or challenging to produce in large quantities.

Radiation damage is not specific to SAXS. It is also a challenge in X-ray crystallography [53] and electron microscopy [54]. In these techniques, a successful approach to reduce damage is to

cryocool the sample to around 100 K prior to exposure to the X-ray or electron beam. Radical diffusion is practically eliminated in frozen solvent, and large-scale structural relaxations are prevented [45]. Cryocooled crystallography samples can withstand a factor of 20-150 times more radiation than room temperature crystals [45], [55]. Therefore, it follows logically that performing SAXS on cryocooled samples would also reduce radiation damage. Additionally, a damage-resistant, cryocooled SAXS sample would not need to be translated through the beam, so a smaller sample volume would be sufficient.

While early studies recognized the utility of cryocooling in SAXS experiments [56], [57], they lacked the reproducible background subtraction necessary for studying small biological macromolecules. A significant portion of the overall scattering signal is contributed by the solvent, and this must be accurately subtracted out to obtain the scattering profile of the molecule. Background subtraction is particularly challenging in a cryocooled sample, which contracts upon freezing. As a result, the length of solution that the X-rays pass through (the X-ray path length) may vary between different samples, and these path length variations can lead to differences in the amount of solvent scattering to be subtracted out from the molecule's SAXS profile. To further complicate the issue, any solvent inhomogeneities that occur during the cryocooling can produce large and irreproducible scatter that interferes with background subtraction [45].

A significant step forwards in cryoSAXS development was performed by the Pollack and Thorne groups at Station G1 at the Cornell High Energy Synchrotron Source (CHESS) [45]. As in earlier work [57], they added a cryoprotectant solution to their SAXS samples to obtain a homogenous solvent after cryocooling. Cryoprotectants form a homogenous, vitrified glass at higher temperatures than water, and can enter this state at lower cooling rates [58], so the risk of crystalline ice formation or other irregularities that could interfere with background subtraction were reduced. Here, the authors undertook a systematic study to identify the optimum cryoprotectant and cryoprotectant concentration to efficiently vitrify the sample without producing unwanted effects on the biomolecule. After

identifying the optimal cryoprotectant solution, they rapidly cooled ~1 µL samples contained in a thin walled polyimide cylinder with the X-ray beam passing along the cylinder's central axis. They observed no radiation damage to a sample of glucose isomerase, and recorded high signal-to-noise SAXS data from an illuminated volume of 13-25 nL [45]. However, the variable X-ray path length of the samples and buffers required a complicated data analysis procedure involving subtraction of both the solvent scatter and the contribution from the beamline background. For the samples used in this work, background subtraction errors could be corrected analytically; however, the authors note that this is not ideal for general SAXS work [45]. The background subtraction problem needed to be further addressed before cryoSAXS could become a widely applicable technique.

The following sections describe the fabrication and implementation of fixed path length sample holders for cryoSAXS. The constant X-ray path length simplifies the background subtraction procedure and allows a data collection protocol more similar to that used in standard SAXS, using only a couple of microliters of sample.

3.2 Fixed path length sample cells for static cryoSAXS experiments

3.2.1 Concept

A redesigned cryoSAXS sample cell was needed to improve upon the background subtraction challenges observed in previous work. The sample cell must satisfy the following conditions:

1. A robust cryoSAXS sample cell needs to have a constant and repeatable X-ray path length. Therefore, it must have extremely strong X-ray windows, which do not bend or deflect even under stresses caused by changes in the sample's volume upon cryocooling.
2. These windows must also be thin enough to present low X-ray absorption, and sufficiently smooth to avoid generating excessive amounts of parasitic scatter.

3. The windows must be tall and wide enough for the X-ray beam to pass through unimpeded.
4. The X-ray path length should be long enough to generate a strong SAXS signal.
5. The sample cell must have low thermal mass so that it can cool quickly. This is essential for sample vitrification.
6. The sample cell must be easy to load and clean, and relatively straightforward and inexpensive to fabricate.

A simple design which meets these criteria is a millimeter scale, open-topped silicon box, which holds a droplet of sample. One set of the box's parallel walls serves as the X-ray windows, while the other set acts as supports. The dimensions of the box can be varied to achieve the desired X-ray path length and window size. Silicon is also an ideal material for the X-ray windows: it is rigid, has relatively low absorbance, and is relatively inexpensive. Additionally, numerous fabrication techniques exist for producing high aspect ratio silicon structures [59].

To fabricate silicon sample cells that fulfill all of the above criteria, we used anisotropic wet etching, a low cost technique that can produce smooth, high aspect ratio silicon surfaces [60]–[62], such as those desired for the X-ray windows. A common chemical etchant is potassium hydroxide (KOH). It preferentially etches silicon's (110) planes over the (111) planes, with selectivities of several hundred to one [60], [61]. Therefore, KOH etching creates extremely high aspect ratio (as much as 600:1 [59]) vertical (111) features on a (110) oriented wafer. These tall, thin features can be incredibly smooth, with an r.m.s. roughness of a few nm [63], and therefore are perfect candidates for cryoSAXS X-ray windows.

3.2.2 Design

The anisotropic nature of KOH etching makes it difficult to design a conventional rectangular box to form the sample cell. However, on a (110) wafer, there are two sets of vertical {111} planes oriented at 70.52° relative to each other [64]. Therefore, it is possible to etch an open-topped, parallelepiped-shaped box with sides formed from intersecting {111} planes. The etch mask shown in Figure 6 defines this structure: one set of planes form the X-ray windows (horizontal lines) and a second set forms rigid support walls (skew lines). Due to the anisotropic nature of the etch, additional features appear that are not explicitly defined in the mask (discussed below).

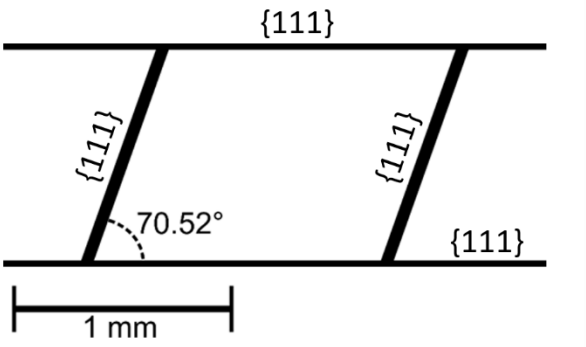

Figure 6. Single unit of the etch mask used to produce the fixed path length cryoSAXS sample cells. This mask was tiled continuously across the wafer to prevent degradation of exposed corners by KOH. Adapted from Ref [41].

Because KOH rapidly degrades exposed convex corners [65], [66], the etch mask shown in Figure 6 was tiled horizontally across the wafer, with no break in the horizontal lines, and a repeat distance of 5 mm. A single, ~75 mm diameter wafer fit 13 horizontal rows, which could be etched into approximately 160 sample holders.

The X-ray windows as defined in the etch mask are 30 μm thick and spaced 1 mm apart. The side supports are 56 μm thick (measured perpendicular to their edges) and are 1.36 mm apart. These final dimensions represent compromises between rigidity (thick windows) and low X-ray absorption

(thin windows), and between high X-ray signal strength (large sample volume) and fast cooling rates (small volume).

3.2.3 Fabrication protocol

All fabrication steps were carried out at the Cornell NanoScale Science and Technology Facility (CNF).

The silicon wafers used in this study are double-side polished (110) wafers with a 76.2 mm diameter and a thickness of 740 mm (Product 310D129987, Virginia Semiconductor, Fredericksburg, VA). Bare wafers were RCA cleaned [67] and rinsed with deionized water to remove dust and contaminants. After cleaning, a chemical vapor deposition furnace was used to coat the wafers with ~100 nm of low stress silicon nitride, which is nearly impervious to KOH. To pattern the wafer, the nitride was first coated with a negative photoresist (AZ nLOF 2020, AZ Electronic Materials, Branchburg, NJ). A contact aligner (MA6, Suss MicroTech, Garching bei München, Germany) was used to align a quartz photomask patterned with the etch mask shown in Figure 6 (produced with a DWL2000 mask writer, Heidelberg Instruments Mikrotechnik, Heidelberg, Germany) to the flat of the wafer, which runs along {111} planes. After exposure and development, the pattern was cleaned and de-scummed (CV200RFS oxygen plasma asher, Yield Engineering Systems, Inc., Livermore, CA). The majority of the nitride coating, which was not protected by this photoresist mask, was removed with a tetrafluoromethane reactive ion etch (PlasmaLab 80+ RIE system, Oxford Instruments, Abingdon, UK). After stripping the photoresist mask, the wafers were RCA cleaned a second time. This left a clean wafer with a complete silicon nitride etch mask.

The processed wafers were etched for 16 hours in a 45%(w/w) KOH solution (Product 3143, Avantor, Center Valley, PA) with 500 nL/L of Triton X-100 ultra-grade surfactant (93443, Fluka, Buchs, Switzerland) added to minimize surface roughness. The etch vessel was contained in a

temperature-regulated ultrasonic bath at 333 K, and covered to limit evaporation. The ultrasonic bath aids in the dissipation of bubbles produced during the etch, further enhancing feature smoothness.

Following the etch, wafers were immediately placed in a beaker of warm, deionized water (333 K). This prevented precipitate debris from crashing out of solution during a rapid temperature change. The wafers were transferred to progressively cooler beakers of water every 2 minutes, for a total of ten rinses. The etched wafers were RCA cleaned a third time, followed by a 30 s dip in 0.8% hydrofluoric acid and a thorough rinse with deionized water. Individual sample cells were cleaved from the completed wafer with a diamond-tipped scribe.

3.2.4 Etched sample cell geometry

As mentioned above, features not present in the etch mask are created in the finished sample cell due to the anisotropic nature of the KOH etch. Figure 7 a) shows a top-down view of a cartoon sample holder. While the features defined in the etch mask are present, there are additional sloping walls inside of the parallelepiped. Figure 7 b) shows the same cartoon sample cell rotated by 30° to provide a different perspective on the sample cell. The sloping walls, while unintentional, provide additional rigidity to the cell. They also take up some of the space inside of the box, reducing the sample cells' volume to ~640 μL. As shown in Figure 7 c), they do not interfere with the path of the X-ray beam. Figure 7 d) shows a top-down optical image of an actual sample cell.

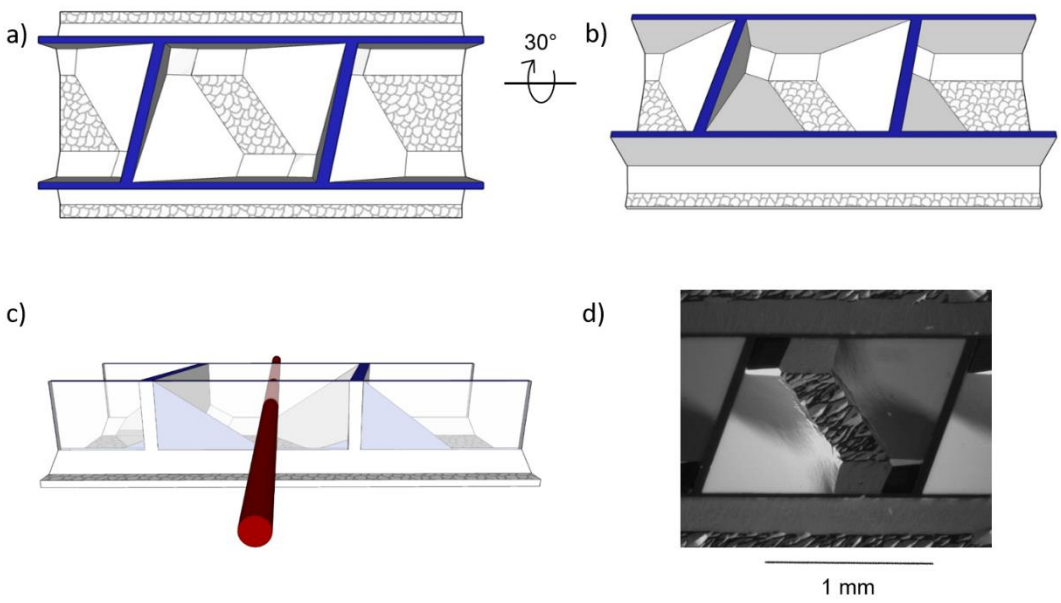

Figure 7. Illustration of sample cell geometry. a) Top-down view of a cartoon sample cell. Blue represents the nitride etch mask. b) The same cartoon cell, rotated by 30°. c) Illustration of the X-ray path through the sample cell. The walls of the cell have been made semitransparent to show that the X-ray beam (red) does not intersect the sloping features inside of the box. d) Top-down image of a real sample cell. Figure adapted from Ref [41].

3.2.5 Characterization of etched X-ray windows

The finished X-ray windows were measured to be about 620 µm tall and 27 µm thick using an optical microscope. The etch mask originally defined the windows to be 30 µm thick; a 1.5 µm underetch occurred. The etch selectivity is 413:1, which agrees with previously reported values [60], [61]. Figure 8 shows a scanning electron microscope image of the end of a sample cell to illustrate the high aspect ratio of the windows.

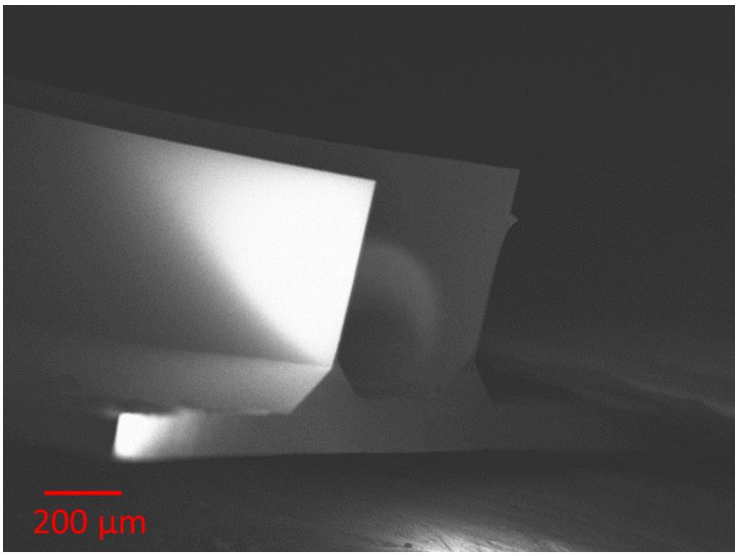

Figure 8. X-ray windows standing tall at the end of a sample cell.

Supra 55VP and Ultra 55 scanning electron microscopes (Carl Zeiss Microscopy GmbH, Jena, Germany) were used to examine the surface roughness of the X-ray windows. Figure 9 a) and b) show SEM images of the X-ray windows before and after the etching and cleaning protocols were optimized. Figure 9 a) shows rough walls covered with precipitate and bits of silicon debris. After implementing the ultrasonic bath and warm water rinse protocols described above, the walls are much smoother, with only isolated debris present, as shown in Figure 9 b). To further characterize the surface roughness, windows were examined with an Icon atomic force microscope (Veeco Instruments, Plainview, NY), as shown in Figure 9 c). The r.m.s. roughness is 1.27 nm over 100 μm^2.

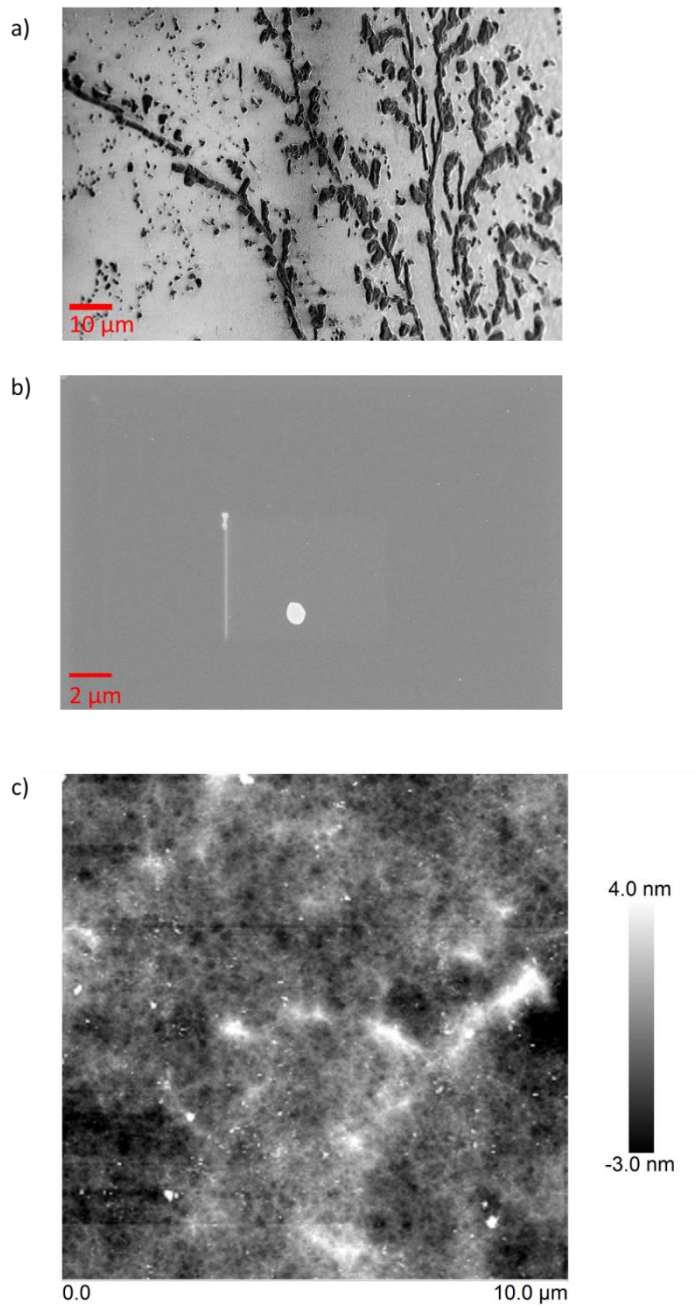

Figure 9. Characterization of X-ray windows. a) SEM image of X-ray windows with unoptimized etch procedure, showing abundant debris and rough surface. b) Windows produced in an optimized etch. They appear smooth in this SEM measurement. The white spot in the middle is a piece of debris, included for focus. c) AFM image of optimized window, adapted from the Supporting Information of Ref [41].

To further characterize the X-ray windows, scattering patterns from the empty silicon sample cells were collected at Station G1 at CHESS. Figure 10 compares the scatter from a sample cell at

room temperature to that from polystyrene, another commonly used SAXS window material. The beamline background scatter is also included for comparison. The scatter from the etched sample cell is less than that from polystyrene at low q, and barely above the scatter from the beamline background, as is expected from such a smooth window surface. Filling the sample cell with buffer at room temperature results in high signal-to-noise data, demonstrating sufficiently long X-ray pathlength. Additionally, the two parallel X-ray windows transmitted about 71% of the ~10.5 keV beam, only slightly below the ~80% transmission of the thin-walled quartz capillaries commonly used for room temperature SAXS experiments [19].

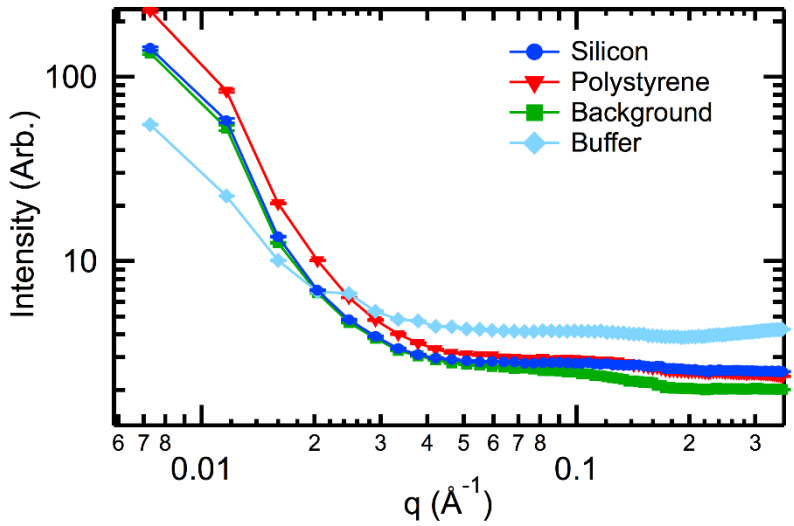

Figure 10. Comparison of scattering from an etched sample cell to another common X-ray window material, polystyrene, and to the beamline background. All profiles were acquired at room temperature. All profiles are normalized by the transmitted beam intensity. Adding buffer to the sample cell results in measurable, high signal-to-noise data. The reduced low q scatter when buffer is present is also observed in other types of SAXS sample cells, and may result from the buffer filling in rough interfaces on the inside of the X-ray windows, slightly reducing their scatter. Figure adapted from Ref [41].

Though the X-ray windows are incredibly smooth and produce very little low q scatter, there are slight variations in the scattering profile from cell to cell, or from different positions in the same sample cell, as shown in Figure 11. This could be due to slight changes in window surface quality, or from differing amounts of parasitic scatter being absorbed by the sample cell's base and interior

features. Therefore, it is important that the X-ray beam passes through the same position on the same X-ray window to ensure proper background subtraction when using these sample cells.

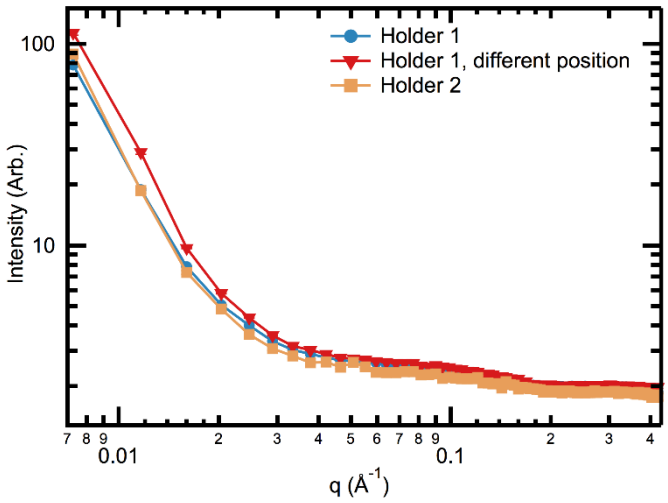

Figure 11. Comparison of scattering profiles from different sample cells or from locations 100 µm apart in the same sample cell. Adapted from [41]

3.3 CryoSAXS data collection in the silicon sample cells

3.3.1 Beamline setup

Figure 12 shows the modified SAXS setup used to collect cryoSAXS data from samples held in the etched silicon cells. A set of tungsten slits placed approximately 1 m upstream of the sample created a 50 µm^2 beam. Two additional sets of tungsten beam guard slits were employed to eliminate parasitic scatter from this initial aperture. Vacuum flight tubes both upstream and downstream of the sample position further reduced parasitic background scatter. A 140 µm thick molybdenum foil was used as a semitransparent beamstop, which served the dual purpose of blocking the direct beam and providing a measure of transmitted counts to normalize the images by. Images were collected with a Pilatus 100K detector (Dectris, Baden, Switzerland).

The X-ray energy was 10.53 keV (1.18 Å), and the flux downstream of the beam-defining slits was measured to be 6.5 x 10^9 ph s^{-1}. The sample-to-detector distance was calibrated with silver behenate powder [68] (from The Gem Dugout, State College, PA, which no longer exists. An equivalent product is B0398, from TCI America, Portland, OR), and varied slightly between beamtimes, but was generally ~1570 mm, resulting in a q range from 0.008 to ~0.3 $Å^{-1}$.

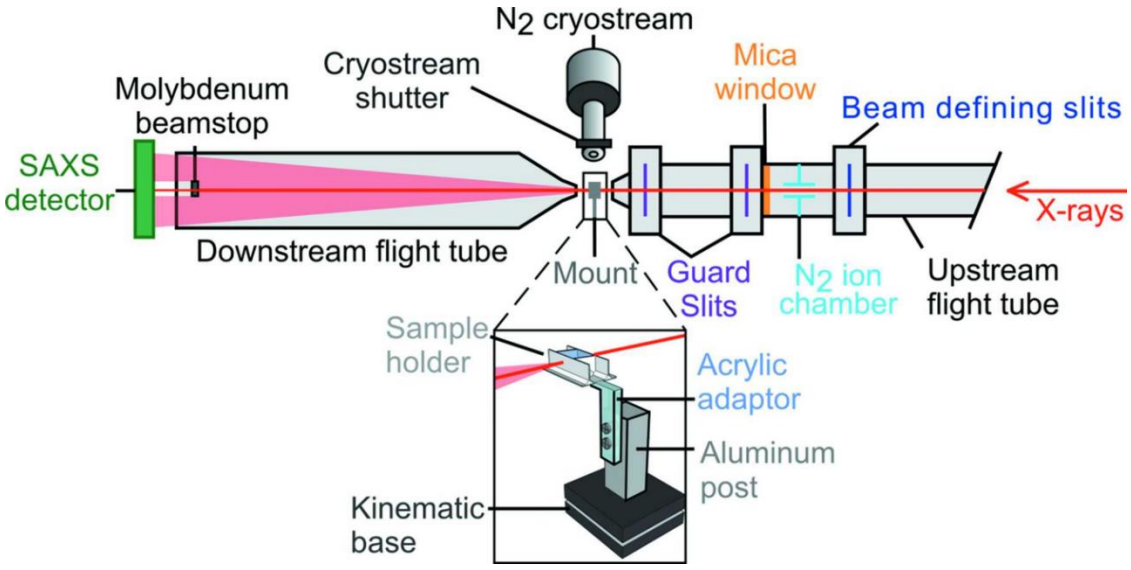

Figure 12. Schematic of the cryoSAXS beamline setup. Inset shows a cartoon sample holder mounted on a kinematic base for repeatable positioning. From [41].

The introduction of an air gap at the sample location facilitated the positioning of a cryostream (700 series, Oxford Cryosystems Ltd, Oxford, UK) for cryocooling the sample to 100 K. An airblade cryostream shutter (credit: Tiit Lukk) was used to ensure rapid and reproducible sample freezing.

To mount the etched cells for cryoSAXS experiments, each individual cell was glued to a lasercut acrylic adaptor for thermal isolation, and secured to a magnetic kinematic base (KB1X1, Thorlabs, Newton, NJ) as shown in the inset of Figure 12. The kinematic base ensured reproducible positioning for the sample cell when it was removed and replaced after cleaning or loading a new sample. This is necessary to keep the scattering from the sample cell constant and to ensure proper

background subtraction. Figure 13 shows the success of the kinematic base in enabling reproducible background scatter.

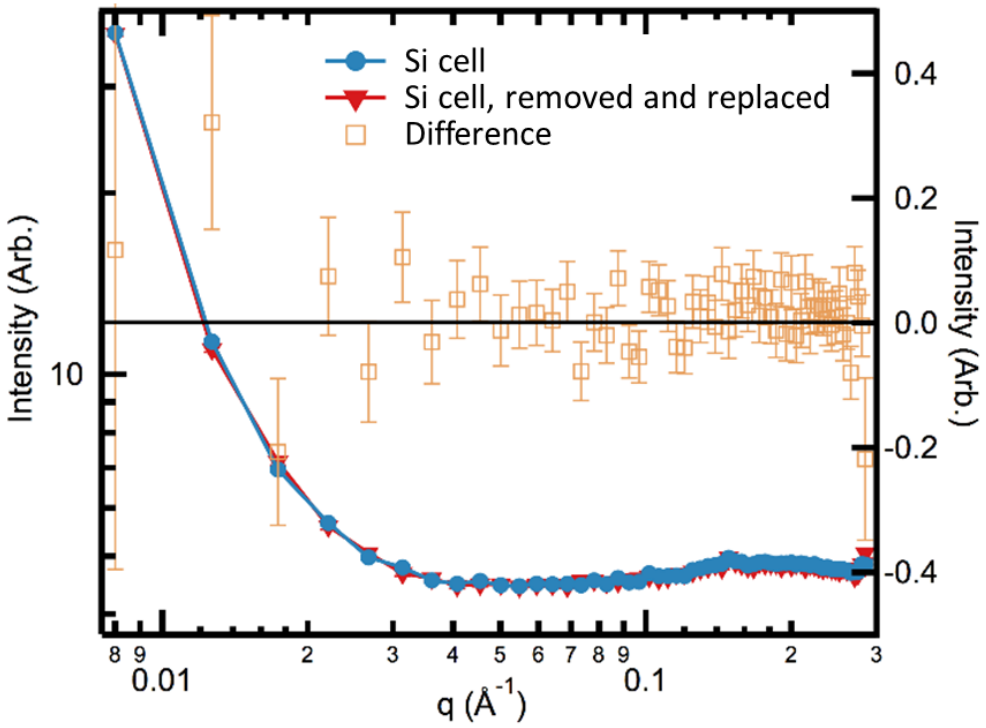

Figure 13. Scattering profiles from the same sample cell before and after removing and replacing it in the beam path. The scattering is unchanged, showing the success of the kinematic base in reproducibly positioning the sample cell. Adapted from [41].

3.3.2 Sample preparation and cryoprotectant selection

Previous work screened several cryoprotectants for use in cryoSAXS experiments [45]. An ideal cryoprotectant must be efficient at preventing the formation of crystalline ice or other nonhomogeneities during freezing while also having no adverse effects on the macromolecule's structure and solubility. Additionally, choosing a cryoprotectant which gives good X-ray contrast (the difference in electron density between the molecules and their solvent [11]) will result in the highest signal-to-noise data. Polyethylene glycol with average molecular weight 200 (PEG 200) at a concentration of 45% (w/w) was found to be the best of those cryoprotectants tested previously [45]. Another cryoprotectant candidate, propylene glycol (PG), was untested in the earlier study, but

provides higher X-ray contrast and is a more effective cryoprotectant by weight. A concentration of 36% (w/w) is sufficient for vitrification of the samples tested here. Due to its lower electron density and the lower required concentration, using PG as a cryoprotectant instead of PEG 200 results in a 17% increase in X-ray contrast. Additionally, the lower viscosity of 36% (w/w) PG makes the solution easier to pipette and clean. All of these characteristics made PG the cryoprotectant of choice for these experiments, though samples were also screened in PEG 200 for comparison.

Samples were prepared according to the protocol described in Ref [45]. First, a double-strength cryoprotectant solution was made, containing either 730 mg/mL of PG or 946 mg/mL of PEG 200, and the same molality of other components as the buffer normally used for the biomolecule. This double-strength solution was combined with solutions containing the molecule, or the molecule's buffer, in a 1:1 ratio using positive displacement pipettes. This created matching molecule and buffer samples with a 36% (w/w) PG or 45% (w/w) PEG 200 concentration.

3.3.3 Data collection at 100 K

First, an empty sample cell mounted on the kinematic base was positioned in the air gap and scanned in to ensure that the X-ray beam was passing through the center of the sample cell. The centered mount was removed from the beamline and the sample cell loaded using a 7000 Series 25 s gauge blunt tipped Modified Microliter syringe (Hamilton Company, Reno, NV) mounted on a PHD 2000 syringe pump (Harvard Apparatus, Holliston, MA).

The syringe pump sample loading system ensured that the cell was filled with a reproducible volume each time. This was essential to obtaining consistent scattering profiles, since small changes to sample volume resulted in differing amounts of high q scatter, even if the sample meniscus was hundreds of microns away from the main beam, as shown in Figure 14. This may be due to the samples absorbing different amounts of parasitic scatter. Placing an X-ray aperture immediately before the

sample cell could solve this problem, potentially simplifying the experiment; however, this was not explored due to the success of the syringe pump loading method.

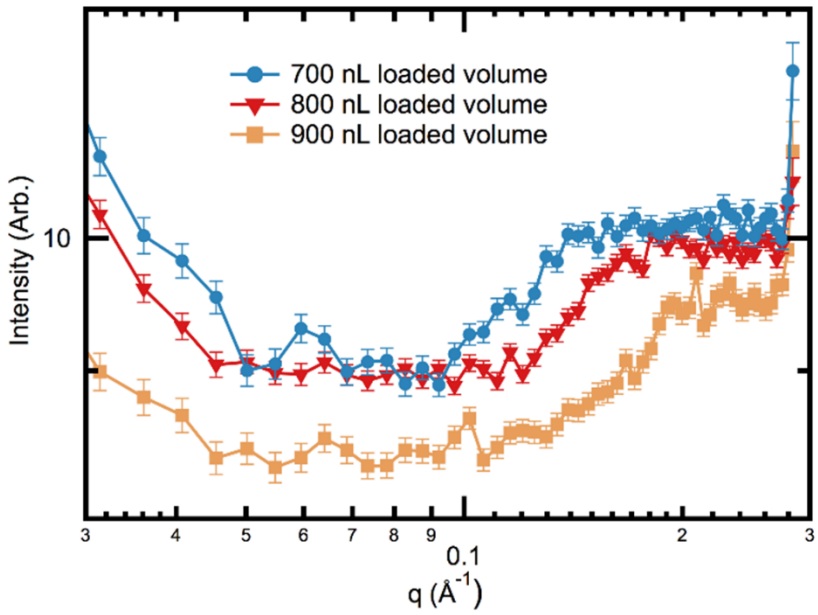

Figure 14. The effect of different sample volumes on the scattering profile. The figure only shows part of the *q* range to emphasize high *q* discrepancies between the different volumes. This effect persists at room temperature, even when the sample meniscus is hundreds of microns away from the beam, and occurs regardless of whether the sample is composed of water or a cryoprotectant solution. Adapted from [41].

The volume of each sample cell is about 640 nL; however, 800 nL of sample were loaded to ensure that the sample cell was completely filled even after sample contraction upon cooling.

To cool the sample in situ, the cryostream was shuttered while the sample mount was replaced on the kinematic base in the beamline, then the cryostream was unshuttered with the cell in place. Cooling rates of about 25 K/s were measured with a 0.01" diameter bare wire E type thermocouple (CHCO-010, Omega Engineering, Stamford, CT) inserted into the sample.

Between 10 and 40 individual, 10 second exposures were averaged together to produce the final scattering profile for each sample, depending on the desired signal-to-noise ratio. After data

collection, the sample cell was removed from the beam, cleaned with filtered, deionized water, and dried with compressed air. To achieve proper background subtraction, scattering profiles from both the molecule-containing solution and the buffer must be measured in the same sample cell, with the X-ray beam passing through the same position as ensured by the kinematic base.

3.3.4 Scattering produced from cryocooled samples

Upon cooling to 100 K, most samples prepared in either cryoprotectant suddenly and dramatically fracture, as shown in Figure 15. These fractures most likely occur to relieve stresses built up as a result of the sample contracting while in contact with the rigid sample cell. Fracturing has been observed in solutions cooled in many geometries of rigid sample cells [69]–[72], so it is not surprising to observe it here as well. The sample cell itself is unharmed by the cooling process.

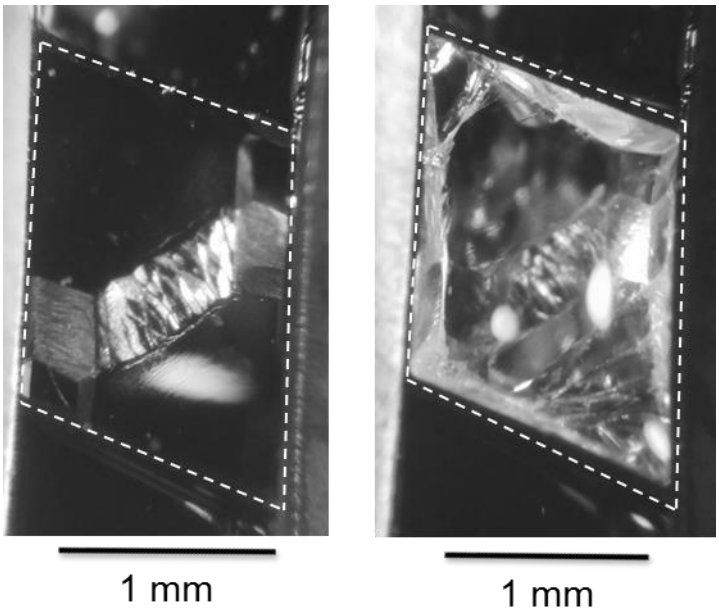

Figure 15. Fractures which occur upon cryocooling. The left image is a top-down view of a sample cell containing a drop of buffer before cryocooling, while the right image shows the fractures observed at 100 K. Dashed white lines show the top of the vertical walls of the sample cell.

Unfortunately, these fractures can cause significant additional scattering, with the magnitude and q range of this contribution depending on the size, orientation, and texture of the fractures. In particular, fractures with interfaces running parallel to the beam path generate significant grazing incidence scatter, which manifests in the image as a bright "jet" emerging from the beamstop. Separately loaded and cryocooled but otherwise identical droplets of sample in the same sample cell can fracture in dramatically different ways, so the fractures cause large, irreproducible, anisotropic contributions to the scattering.

Fractures can be reduced or eliminated by reducing the cooling rate or increasing the final temperature [72], both of which reduce the magnitude of stresses that build up as a result of differential contraction of the sample and sample cell during cooling. Although these protocols yielded cryocooled samples that appeared optically clear, homogenous, and unbroken, these samples produced highly irreproducible and anisotropic scatter at all q values (see Figure 16 for example images). Therefore, elimination of visible fractures is not sufficient for obtaining reproducible scattering profiles from cryocooled samples. In previous work, reproducible scattering profiles were acquired from unfractured, cryocooled samples [45]. These samples were held in flexible holders and could contract freely. It appears that stresses must be further reduced beyond that needed to prevent fractures in order to produce repeatable scattering profiles.

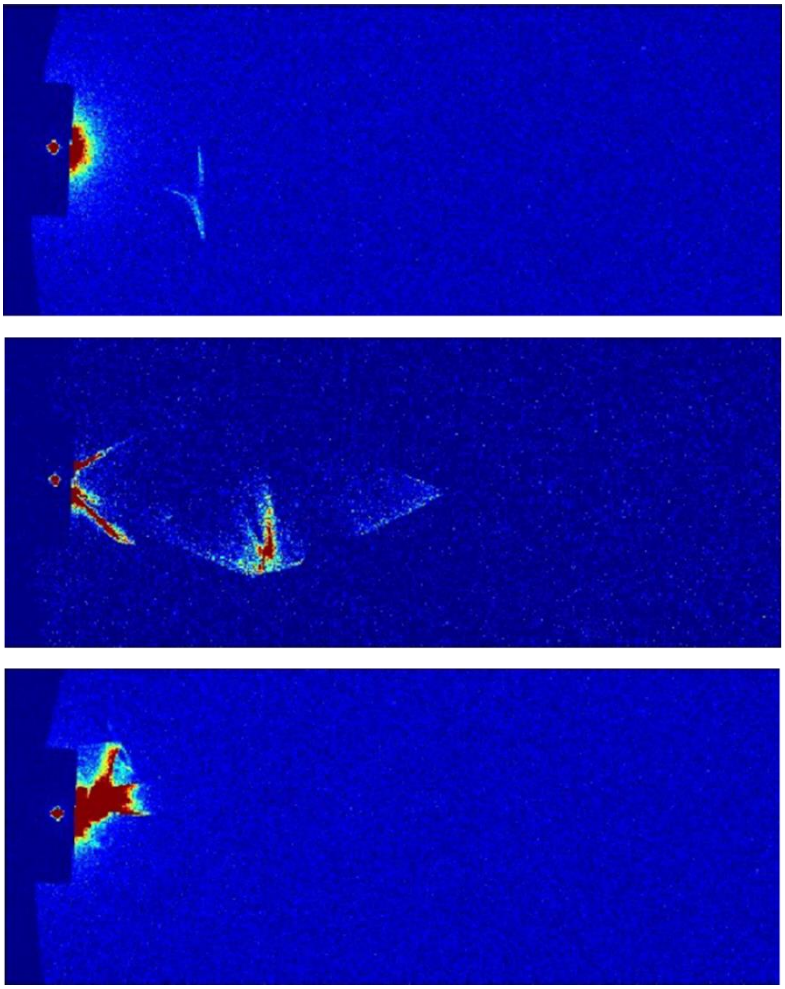

Figure 16. Detector images showing irreproducible, anisotropic scatter caused by optically clear and un-fractured cryocooled samples.

Several changes were made to the sample cells in hopes of reducing stress, with no significant improvement. Varying the sample cell height and width or removing the bottom from the sample cell did not prevent the highly anisotropic, irreproducible scatter. Changing the sample cell geometry to eliminate these stresses while still maintaining the constant X-ray pathlength required for accurate background subtraction is nontrivial, and is an area for future exploration.

While the fractured samples do produce anisotropic, irreproducible scatter, the contribution from the fractures is often localized to an angular slice of the image, unlike the scatter from the optically clear but stressed cryocooled samples, which can encompass large areas of the image.

Therefore, fractured samples are preferable in cryoSAXS. Special data processing techniques, discussed below, can mask the contribution of the fractures to give robust scattering profiles.

3.3.5 Masking technique to eliminate the scattering from fractures

The variability of fractures in separately cooled but otherwise identical samples suggests that any difference in the scattering profiles from different trials of the same sample should be due to the fractures. Therefore, the extent to which the profiles obtained in two different trials agree indicates which parts of the profile reflect the actual scatter from the sample and which parts contain additional scattering from the fractures. It is necessary to collect scattering profiles from at least two trials of each sample to ensure that the sample's underlying scatter is accurately captured.

While the scattering produced by fractured samples is highly irreproducible, there are three general observed behaviors. Some fractured samples produce isotropic scattering similar to that observed at room temperature. Others produce excess isotropic scattering at low q, or display the strong, anisotropic 'jets' mentioned above. These behaviors are not mutually exclusive, and jets can occur over either type of isotropic scattering. Figure 17 a) shows examples of the scattering images produced by fractured samples.

To remove the contribution of scattering from the fractures, it is possible to mask out bright isolated jets in some images, such as those shown in images 2 and 3 of Figure 17 a). The resulting scattering profiles agree well down to q = 0.02 Å^{-1}, as shown in Figure 17 b), suggesting that the unmasked parts of the image are not affected by the fractures and therefore yield accurate scattering profiles from the molecule. However, if the image shows many, overlapping jets and/or bright, excess isotropic low q scatter, like image 1 in Figure 17 b), no mask is sufficient to remove the scatter from the fractures and achieve agreement with profiles from other trials of the same sample.

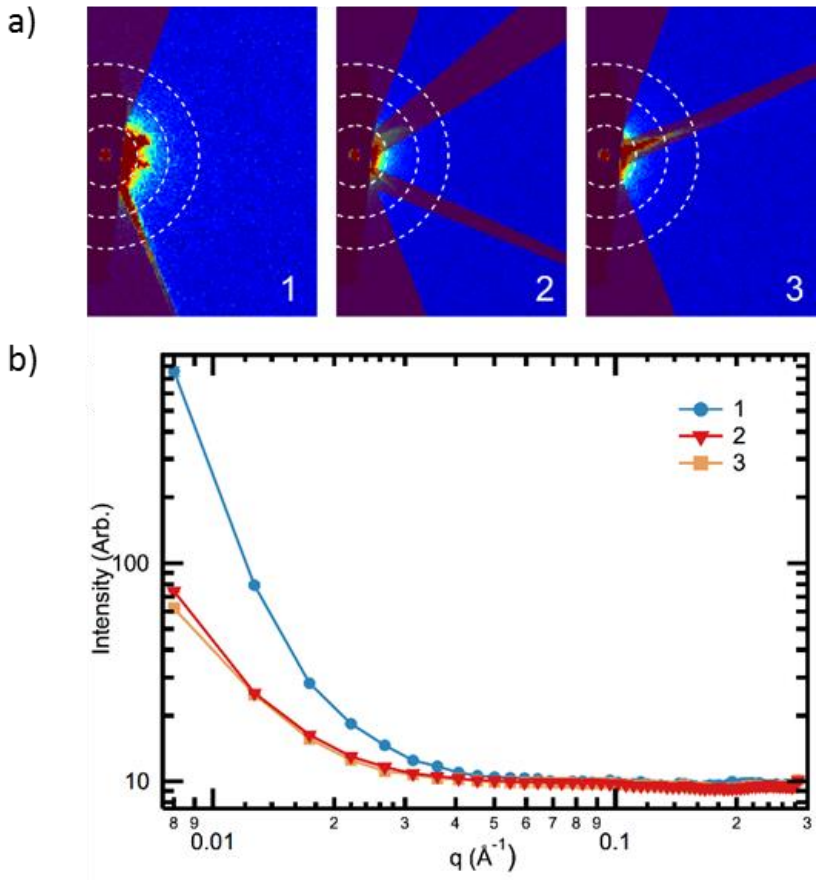

Figure 17. Masking technique to eliminate the contribution from fractures. a) Scattering images showing (1) bright, isotropic scatter with overlying jets, and (2,3) isolated jets. The red overlay represents the mask used to integrate the image in each case. Dashed white lines represent q = 0.01, 0.02, and 0.03 Å^{-1} with increasing radius. b) Integrated scattering profiles for the images shown in a). Image 1 was integrated despite the visible presence of jets that have not been masked out. No mask is sufficient to bring the scattering profile from Image 1 into agreement with the other profiles. Figure adapted from Ref [41].

After masking, the lack of agreement of otherwise identical scattering profiles below q = 0.02 Å^{-1} likely results from isotropic scattering from the fractures. Unfortunately, this contribution cannot be removed by masking. This minimum q value places some limitations on the size of the largest molecule that can be studied with cryoSAXS. According to the Shannon sampling theorem, full information is contained in the scattering profile as long as the minimum q value is less than the Shannon increment:

$$q_{min} < \pi / D_{max} \quad (7)$$

where D_{max} is the maximum dimension of the molecule [11]. For a minimum q value of 0.02 Å^{-1}, D_{max} is 157 Å. Therefore, while cryoSAXS in these rigid sample cells is suitable for small macromolecules such as some proteins or nucleic acids, it may not provide enough information about complexes or larger particles such as viruses. Further work is needed to reduce the contribution of scattering from the fractures and increase the applicability of cryoSAXS to a larger range of molecule sizes.

3.3.6 CryoSAXS scattering profiles of standard SAXS molecules

The new methodology and sample cells described above were used to study two protein molecules that frequently serve as SAXS standards: lysozyme and glucose isomerase.

Samples prepared in PEG 200 were difficult to dispense in precise volumes: the increased viscosity of the solutions made it challenging to accurately load the sample, even using the syringe pump setup described above. Samples prepared in PG dispensed more easily, depositing a reproducible volume for accurate background subtraction.

Unfortunately, each cryoprotectant studied had an undesirable effect on one of the samples. The lysozyme prepared in PG aggregated upon cryocooling, as shown in Figure 18. Cryocooled lysozyme prepared in PEG 200 did not aggregate in previous work [45] or in this study, but the viscous solution made reproducible background subtraction impossible. On the other hand, cryocooled glucose isomerase behaved well when prepared in PG, but when prepared in PEG 200, the scattering from sample-containing solution was lower than the scattering from the buffer at higher q, even when accounting for difficulties in background subtraction. This behavior was not observed in the same solutions at room temperature, and could result from changes in the hydration layer of the molecules upon cryocooling. These two examples demonstrate another challenge for cryoSAXS: each molecule

may need to have the cryoprotectant and buffer solution carefully tailored to its chemistry for a cryoSAXS experiment. A search of buffer conditions over a wide range of pH and buffering ingredient did not produce any conditions which prevented aggregation of lysozyme upon cryocooling in PG. Developing a method to test cryoprotectant compatibility ahead of the cryoSAXS experiment is necessary to make cryoSAXS a widely applicable technique.

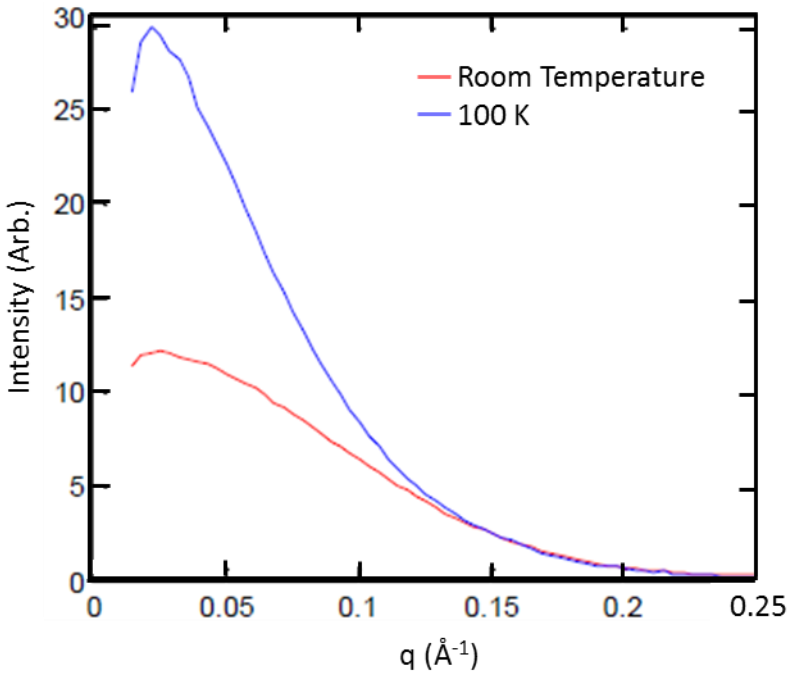

Figure 18. Comparison of scattering profiles from lysozyme in a 36% (w/w) PG solution at room temperature and at 100 K.

Fortunately, cryocooled glucose isomerase in PG was well behaved and provided an opportunity to test these fixed pathlength sample cells. Scattering profiles at room temperature and at 100 K agreed with either other well down to q = 0.02 Å^{-1}, and they also agreed with previous data acquired in the flexible, windowless holders from Ref [45]. Figure 19 shows these scattering profiles, along with DAMMIF reconstructions of glucose isomerase using both the room temperature and 100 K data. These envelope reconstructions agree well with both each other and the crystal structure. Background subtraction was robust and performed in the standard SAXS analysis manner, without the

added complications employed in earlier work [45]. No radiation damage was observed in this work, even after 50 minutes of continuous data collection.

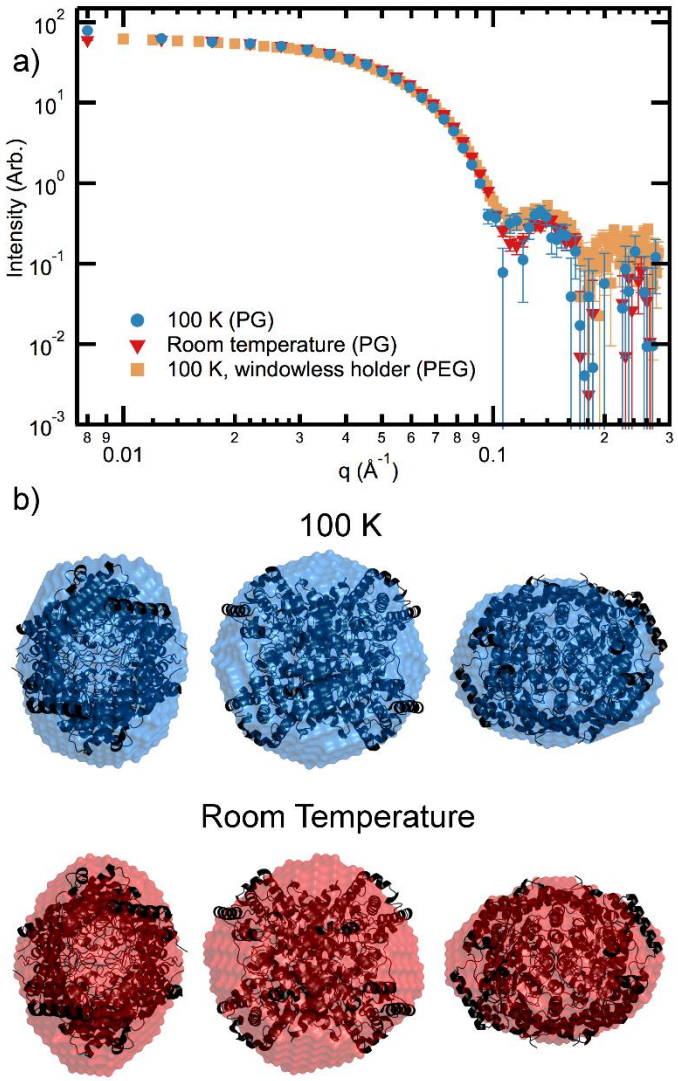

Figure 19. CryoSAXS of glucose isomerase. a) Scattering profiles obtained from glucose isomerase in the silicon sample cells at both room temperature and 100 K. The scattering profile of glucose isomerase in the windowless sample holder and PEG 200 cryoprotectant used in earlier work [45] is also included. b) Envelope reconstructions of glucose isomerase in the silicon sample cells at room temperature and 100 K, superimposed over the crystal structure (PDB 1XIB [40]). Figure from Ref [41].

3.4 Outcome and challenges

The fixed path length, silicon sample cells dramatically simplify background subtraction for cryoSAXS experiments, making the technique more robust and accessible. No radiation damage was observed, and the required sample volume was lowered to 1.6 µL (two 800 nL trials). Therefore, cryoSAXS could increase the applicability of SAXS to scarce or radiation-sensitive samples.

Fractures in the sample do irreproducibly and anisotropically impact the scattering profile, but the scattering from these fractures can often be masked out to extract the underlying scattering profile of the molecule. It is necessary to acquire at least two scattering profiles from each sample to ensure that the scattering contribution from the fractures has been adequately removed. Additionally, the largest molecule size that can be studied with cryoSAXS is limited by low q scatter from the fractures. Optimization of the sample cell design and freezing protocol to reduce stress upon cryocooling could eliminate these fractures, increasing the number of molecules that can be studied with cryoSAXS and further simplifying cryoSAXS data analysis.

Interactions between the molecules and cryoprotectant or between the molecules themselves during cryocooling may cause aggregation or other difficulties during a cryoSAXS experiment; this challenge exists regardless of sample holder geometry. An improved understanding of the physics and chemistry of these cryocooled solutions is necessary to ensure a well-behaved sample. Additionally, the differences in hydration layer due to the presence of the cryoprotectant and during cryocooling must be considered when modeling cryoSAXS data with calculated SAXS profiles such as those produced by CRYSOL [41]. Future understanding of these interactions will enable the collection and utilization of high signal-to-noise cryoSAXS data from small sample volumes with no observable radiation damage. High pressure cryocooling, which allows vitrification of aqueous samples without the use of cryoprotectant, is a promising area for future exploration which may help to eliminate many of these experimental challenges [73].

CHAPTER 4

HIGH SIGNAL-TO-NOISE TIME-RESOLVED SAXS FROM SMALL SAMPLE VOLUMES

The work described in this chapter was performed in close collaboration with George Calvey. Alex Plumridge, Suzette Pabit, and Robb Welty made the tP5abc and rRNA samples. Alex Plumridge analyzed the tP5abc data.

Detailed drawings for the custom parts described in this chapter can be found at Cornell's eCommons (http://hdl.handle.net/1813/57588). All custom parts were designed and drawn by George Calvey and me.

4.1 Introduction

4.1.1 Why time-resolved SAXS?

Solution-methods like SAXS offer great advantages: the molecules in the sample are not confined to a crystal structure or biased into certain conformations by the presence of their crystal contacts. They are free to explore conformational space. Therefore, SAXS is particularly well suited for characterization of the structural dynamics that accompany folding, ligand binding, or complex formation.

Combining SAXS with microfluidic mixing technology allows experimenters to initiate a molecular reaction in a rapid and controlled manner, for example, by combining a biomolecule with a ligand or reactant which induces folding. Scattering profiles can be acquired at various delay times after mixing to observe the ensemble of conformational states present. Time-resolved SAXS data provide insight into the structures of transient intermediate states and their lifetimes. This information

can be used to tune molecular models, gain fundamental understanding of biochemical processes, or design new drugs that target and bind to intermediate states.

4.1.2 Continuous flow time-resolved SAXS and associated challenges

As described in previous chapters, the majority of time-resolved SAXS experiments utilize either stopped flow or continuous flow mixing technology. Due to the large sample consumption of stopped flow SAXS [20], its utility in studying precious samples is limited. Therefore, this section will focus on continuous flow time-resolved SAXS mixers and methodology.

Most continuous flow mixers used for SAXS experiments mix via diffusion. A schematic of a very successful type of SAXS mixer implemented by Pollack and coworkers [15] is shown in Figure 20. The mixer consists of three inlet flow channels, which are combined into a fourth outlet channel. A solution containing the biomolecule of interest flows through the central inlet channel, and a reactant solution flows through the others. When the three flows meet, the central sample stream is hydrodynamically focused into a thin jet surrounded by reactant solution [15], [74]. The reactant can then rapidly diffuse across the sample jet, initiating the reaction. The reacting mixture evolves in time as it precedes down the outlet channel. Therefore, by probing with the X-ray beam at various distances past the focusing point (delay lengths), it is possible to acquire data at a range of timescales after the reaction began (delay times). The jet need only be focused in one dimension, so it is possible to obtain a long (~1 mm) X-ray path length by orienting the beam perpendicular to the plane of the mixer.

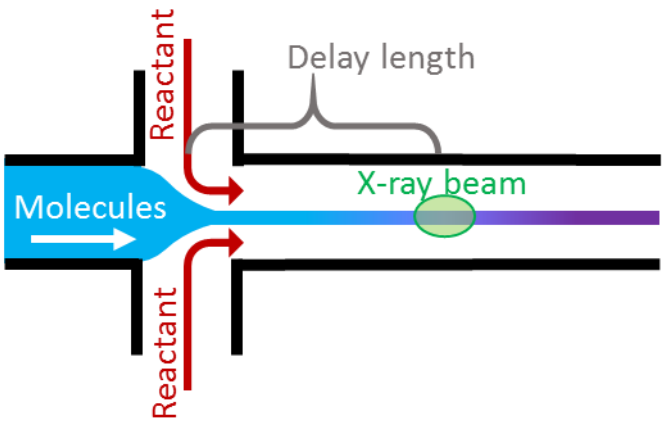

Figure 20. Schematic of the type of mixer used by Pollack et al [15], [16], [51]. This is a two-dimensional device with rectangular channels. The molecule-containing solution is hydrodynamically focused into a thin jet by solution containing the reactant. The X-ray beam is directed into the plane of the page to maximize the X-ray pathlength, since the jet does not need to be focused in this dimension.

Continuous flow SAXS has been successful in studying protein and RNA folding [15]–[17], [51] on timescales as short as sub-millisecond. However, some experimental challenges exist. First, though the X-ray path length can be ~mm long, the sample jet is extremely thin in the perpendicular dimension. To reduce excess solvent background scattering, the beam must also be made very thin by either capillary focusing or by reducing the size of the beam-defining aperture, both of which lower the X-ray flux. To achieve high signal-to-noise measurements with this lower flux, longer data collection times are needed [42]. Though continuous flow mixers have relatively low sample flow rates, the required volumes quickly add up over these long collection times, especially when acquiring data at multiple time delays.

Continuous flow mixing experiments also require careful evaluation of the timing dispersion, or the spread in the amount of time that the reaction has been allowed to precede for each molecule that passes through the X-ray beam. There are several sources of timing dispersion present in a continuous flow mixer. The first is premixing, in which the molecules on the outside of the sample stream are exposed to the reactant sooner than the molecules on the inside when the flows are first being combined. The second comes from the flow profile of the mixture flowing down the channel:

faster in the center and slower against the walls. These sources of timing dispersion can be reduced by carefully engineered modifications to the mixer. The addition of a sheath flow between the reactant and molecule solutions ensures that the molecule solution does not meet the reactant until the sample stream is thinned out, reducing premixing [75]. Similarly, adding a sheath flow between the sample and the X-ray windows keeps the molecule-containing jet in the center of the channel and reduces parabolic flow dispersion [51]. However, these changes complicate the fabrication and operation of the mixer by requiring more inlets and more pumps to run them.

Additionally, the diffusive processes that facilitate mixing in the device shown in Figure 20 must be carefully considered when designing a mixing experiment and when analyzing the data. First, diffusion continues throughout the thinned sample jet in the combined flow outlet channel. Therefore, as the delay time increases, more reactant diffuses into the sample jet. This changing reactant concentration can complicate data analysis. Secondly, while the larger biomolecules take longer to diffuse than the reactant, at long timepoints (~1 second) the molecules diffuse out of the central jet, reducing sample concentrations and decreasing signal strength [17].

This chapter describes the fabrication and implementation of a new continuous flow SAXS mixer, adapted from time-resolved crystallography experiments, which addresses these challenges. Its geometry is compatible with a larger, higher flux x-ray beam, enabling high signal-to-noise data collection in a shorter amount of time. It induces rapid focusing to eliminate premixing, and the sample flow is fully sheathed to reduce parabolic flow dispersion. Additionally, the design keeps both the reactant and biomolecule concentration consistent at different delay times, simplifying analysis.

4.1.3 Mixer inspiration and concept

The mixer used in these experiments was inspired by a design implemented by Calvey and coworkers in time-resolved serial crystallography experiments at X-ray free electron lasers [76]. A

simplified schematic of this mixer is shown in Figure 21 a). Like the mixer presented in Figure 20, Calvey's device uses hydrodynamic focusing to create a thin sample jet across which the reactant can rapidly diffuse. However, the latter device has several advantages that make it ideal to adapt to SAXS.

This mixer is comprised of concentric glass capillary tubes and is cylindrically symmetric, in contrast to the 2D geometry more common to continuous flow SAXS mixers. This geometry vastly simplifies the fabrication process (there are no clean room etching or lithography procedures, and one simple epoxy step seals the device) as well as the operation. In Calvey's mixer, the sample jet is symmetrically sheathed by reactant solution on all sides, minimizing flow dispersion. To maintain a symmetric sheath in a 2D device would require at least five pumps: one for the sample, two for the horizontal sheath flows, and two for the vertical sheath flows. (Each sheath channel needs its own pump to ensure that the sheath does not flow preferentially in one channel and create an off-center jet.) With the cylindrical geometry, only two pumps are needed: one for sample, and one for reactant. Therefore, there is much less equipment to set up and run at the beamline, increasing the robustness of the experiment.

An additional advantage of Calvey's device is its constricted focusing region, which causes the sample jet to thin very rapidly, virtually eliminating premixing [76]. It also reduces the amount of reactant solution needed to thin the sample jet sufficiently for fast diffusion.

4.2 Mixer principle and fabrication

This section is derived from the Supporting Information of Ref [77].

4.2.1 Concept and principles of new SAXS mixer

Figure 21 b) illustrates the adaptation of this device to SAXS experiments. The new SAXS mixer can be divided into three functional regions. The *focusing region* of the device is the same as in the parent mixer: biomolecule-containing solution flowing out of the inner sample supply capillary is focused down into a thin jet (6-12 μm wide) by a coaxial flow of reactant-containing solution. Both the sample and its coaxial reactant sheath are forced into a constriction: a 30 μm inner diameter capillary. The flow profile develops quickly and minimizes pre-mixing as described in [76].

The constriction forms the *mixing region* of the device. Here, the reactant diffuses rapidly across the thin sample jet. The sample biomolecules, due to their larger size, do not diffuse appreciably out of the central jet.

The *delay and probe region* is comprised of thin walled polyimide tubing (Code # 145, Microlumen, Oldsmar, Florida) with ~370 μm inner diameter. The sample jet slows and expands as it moves from the constriction to the delay and probe region, creating a larger X-ray path length, approximately 80-150 μm depending on flow parameters. This larger sample jet diameter enables the use of a bigger, brighter X-ray beam than the one previously used with traditional continuous flow SAXS mixers. The gain in diameter more than compensates for the loss in X-ray pathlength relative to a 2D device, so high signal-to-noise data collection can occur more quickly, using smaller amounts of precious sample.

The expanded sample jet also reduces diffusion, so that the average reactant concentration along the sample jet remains roughly constant. This greatly simplifies interpretation and analysis of the data. Similarly, the large size of the sample jet prevents the biomolecules from diffusing out of it as quickly, maintaining the sample concentration at delay times as long as several seconds.

Because diffusion is significantly reduced downstream of the constriction, the sample is considered to be fully "mixed" when it enters the expanded region. Therefore, the delay time for this mixer is defined to be the time elapsed between the exit of the sample from the outlet of the constriction to its intersection with the x-ray beam. Different delay times can be accessed by either moving the mixer relative to the beam or changing the flow rates.

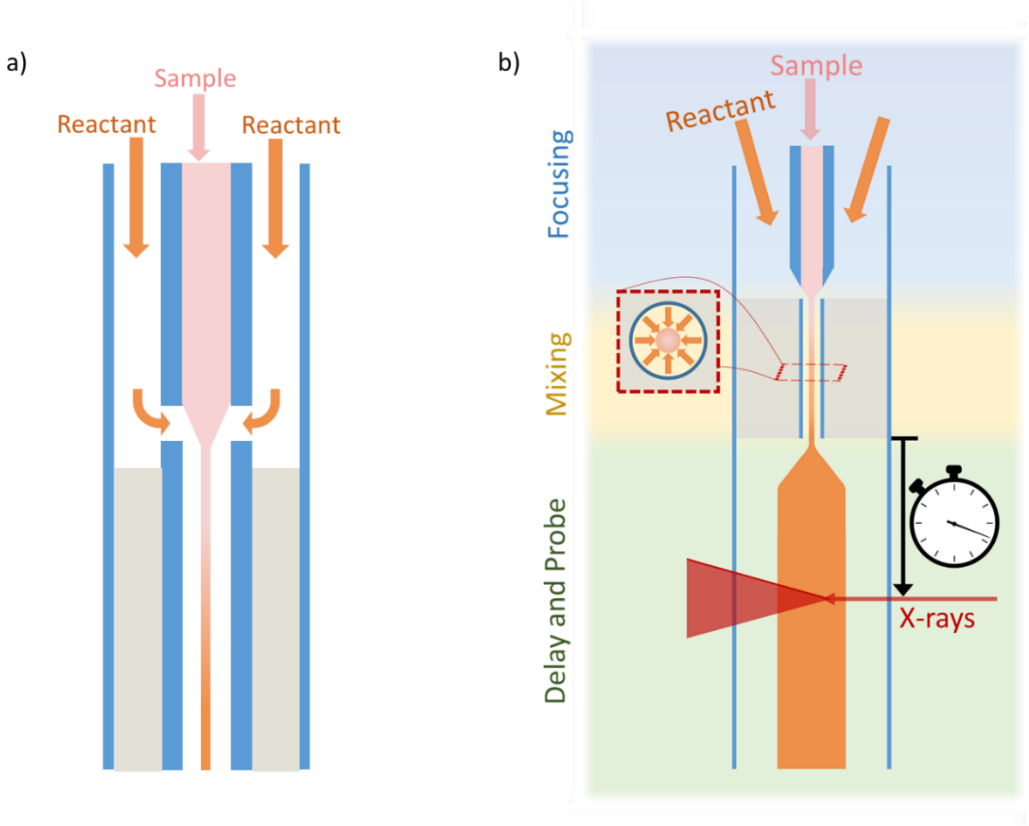

Figure 21. Simplified schematics of the new SAXS mixer and its inspiration. a) The crystallography mixer developed by Calvey et al. [76]. Sample and reactant solutions traveling in concentric capillary tubes are combined into a single constricted outlet channel, where the reactant diffuses quickly across the focused sample jet. UV curable epoxy (shown in gray) bonds the capillaries together. b) The adaptation of this design to SAXS experiments. The upstream focusing and mixing regions are the same as in the parent mixer. An additional expanded region provides an ideal observation chamber for time-resolved SAXS experiments. Figure adapted from Ref [77].

4.2.2 Timing dispersion: sources and minimization

In any mixing experiment, it is important to consider the sources of timing dispersion and how they impact the observation of structural intermediate states. To understand this effect, it is first necessary to consider the chemical kinetics inside of the mixer.

Within the SAXS mixer, a chemical reaction initiates between the biomolecules and the reactant solution. As in all chemical reactions, the biomolecules in the sample will occupy a mixture of structural intermediate states at any time. Therefore, it is not possible to observe complete occupancy of a transient state. The measured SAXS profile at a given delay time reflects the average of the ensemble of structures present at that time. The ensemble modeling techniques described in Chapter 2 can be used to gain insight into the variety of states that may be present.

While it is not possible to directly observe a transient intermediate state, it is possible to design the experiment to maximize the number of molecules in the sample that may occupy the state at the same time, increasing the chances of detecting the state with ensemble modelling. Boosting the occupancy can be accomplished by minimizing the timing dispersion present in the mixture.

There are many sources of timing dispersion in an experiment utilizing these mixers. First, consider the mixing region of the device. As the sample jet travels down the constriction, biomolecules on the outside of the jet reach a high reactant concentration sooner than those in the middle. A larger diameter sample-containing jet takes longer to reach the desired concentration of reactant in the center (a longer “mixing time”), which means it will have a larger dispersion in the reaction time origin for different biomolecules in the sample, decreasing the occupancy of transient states. Faster mixing can be accomplished by creating a thinner inner jet which favors rapid reactant diffusion, for example by flowing proportionately more reactant solution. However, this decreases the X-ray pathlength and therefore costs signal strength. Therefore, a compromise must be found between fast mixing times and data quality. Choosing flow parameters to achieve a mixing time short relative to the lifetime of the

transient intermediate states improves the chances of detecting these structures. A mixing time of 10s of milliseconds is often sufficient for a 100 ms delay time.

Another source of timing dispersion arises from the parabolic flow profile of the sample in the observation channel, which causes sample in the center of the jet to move faster than the sample at the edges of the jet. This effect is minimized by the presence of the reactant sheath, which prevents any sample molecules from touching the capillary walls, but it must be considered when calculating the range of delay times present in a given measurement.

Finally, due to the finite width of the X-ray beam, a range of delay times are always probed at once. Using a smaller X-ray beam reduces this spread, but at the expense of signal.

For the experiments described below, flow parameters were chosen such that the total timing dispersion (the dispersion from mixing time, flow profile, and beam size added in quadrature) was 10-15% of the delay time. This number was chosen as a compromise between high populations of intermediate states and experiment success.

4.2.3 SAXS mixer fabrication and mounting

A schematic showing the steps of the SAXS mixer fabrication is shown in Figure 22. Most fabrication procedures are identical to those described in Ref. [76].

The first step was to select and polish the polyimide-coated glass capillaries that ultimately form the mixers' outer body (which contains the reactant flow), the sample supply line, and the constriction. 50 µm inner diameter/200 µm outer diameter tubing (TSP050192, Polymicro Technologies, Phoenix, Arizona) was chosen for the sample supply line as a compromise between reducing the sample volume in the line and avoiding clogs. 30 µm ID/150 µm OD tubing (TSP030150, Polymicro Technologies) was used for the constriction, and 280 µm ID/360 µm OD tubing (Z-FSS-

280360, Postnova Analytics, Landsberg am Lech, Germany) was used for the outer mixer body. These capillaries were scribed to length with a diamond scribe. To facilitate symmetric and rapid focusing, the tips of all capillaries were ground flat on an Allied Multiprep polishing system for 8" platens (Allied High Tech Products, Inc., Los Angeles, California), and the downstream tip of the sample supply line was beveled to a point (Figure 22 a).

The second step was to prepare the capillaries for assembly. To hold the capillaries concentric, 0.002" thick polyimide centering spacers (produced by George Calvey using the Schaffer-Nishimura Lab's femtosecond laser. See Ref [76] for pictures and description of the spacers) were installed over the sample supply capillaries and constrictions, as shown in Figure 22 b). Next, the polyimide coating was removed from the downstream end of the outer mixer body to facilitate the curing of the UV epoxy (UV15, Master Bond Inc., Hackensack, New Jersey) used to bond the constriction into place. A handheld butane torch (MT-30, Master Appliance Corporation, Racine, WA) was used to burn off this coating without melting the underlying glass. Then, the constriction and sample supply lines were inserted into either end of the outer mixer body. UV epoxy was dispensed into the gap between the mixer body and the constriction using a 30 gauge needle. The epoxy wicked up the gap, and around the star shaped spacers. Upon reaching the tip of the constriction, it was rapidly cured from both sides with light from a 365 nm LED (LZ1-30UV00-0000, LED Engin Inc., Marblehead, MA) to secure the constriction in place and completely seal the gap around it. The two-sided cure is essential, since the polyimide coating on the constriction is absorbs 365 nm light, and epoxy in the constriction's shadow will not be cured. The bonded capillaries were cut to the desired constriction length with a diamond saw, then the ends were polished flat using the Multiprep polisher. Figure 22 c) shows this point in the assembly process.

To create the observation region, a piece of polyimide medical tubing with 1 mil wall thickness and ~370 μm ID (Code # 145, MicroLumen, Oldsmar, Florida) was fitted over the capillary assembly and sealed in place with Double/Bubble Extra Fast Setting epoxy (Hardman Adhesives), as shown in

Figure 22 d). The mixers were secured to a metal frame to protect them and to facilitate mounting in the beamline (setup discussed below), with standard 10-32 coned fittings (P-728 tee assemblies and P-760 union assemblies, IDEX Health & Science, LLC, Oak Harbor, WA) for connecting to 1/16" tubing from the liquid reservoirs. Figure 23 shows a schematic of fluidic connections and a picture of completed mixers mounted on their frames.

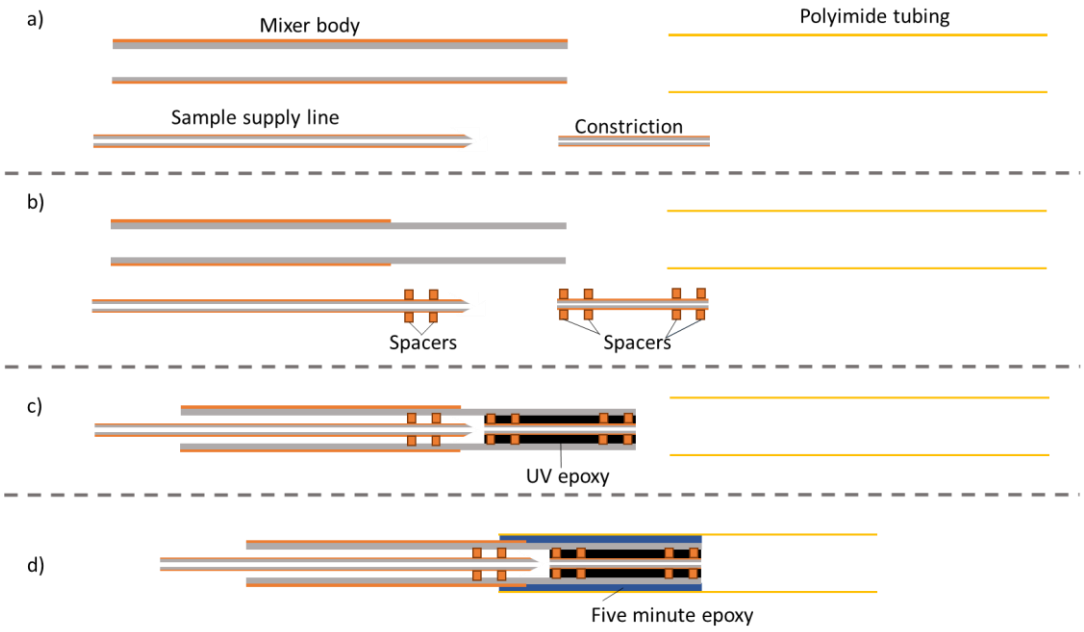

Figure 22. Schematic of key steps in the mixer assembly process. a) The glass capillaries are scribed to length and polished. b) Polyimide centering spacers are installed over the two inner capillaries, and the polyimide coating is removed from part of the outer capillary. c) The inner capillaries are inserted into the outer capillary, and the constriction glued in place with UV epoxy. d) The polyimide tube that will form the observation region is glued over the bonded glass. Figure adapted from the Supporting Information of Ref [77].

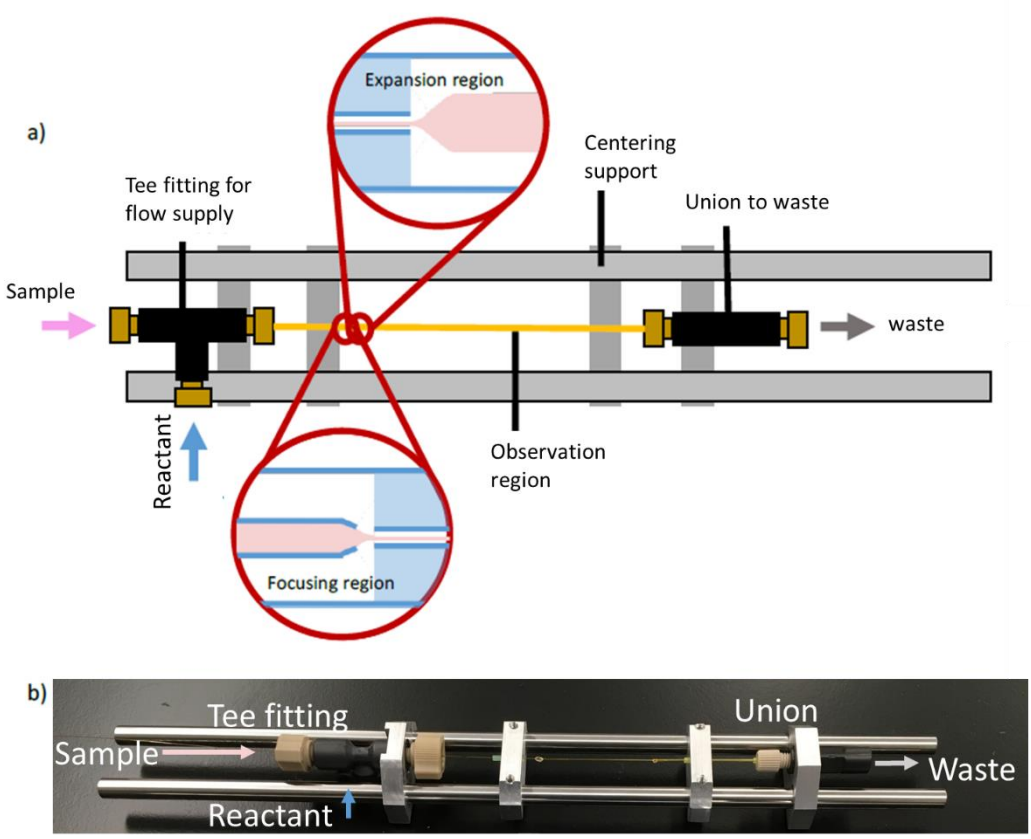

Figure 23. Mounted mixer and fluidic connections. a) Schematic showing components in the final assembly, with insets showing the flow profiles in the focusing and expansion regions. b) Picture of a real mixer, with components and flow paths labelled for reference. The metal support rods are 8 inches long. Figure from the Supporting Information of Ref [77].

4.3 Configuring the beamline

4.3.1 Producing a small, stable X-ray beam

Time-resolved mixing experiments were performed at Station G1 at the Cornell High Energy Synchrotron Source, with several modifications to the standard SAXS setup often used there. As described in Chapter 2, most SAXS experiments use a beam defining aperture in combination with one or more sets of guard slits to reduce parasitic background scatter. The standard G1 SAXS setup is shown schematically in Figure 24 a). A set of tungsten slits (Advanced Design Consulting USA Inc., Lansing, NY, USA) serves as the beam defining aperture, with a second set about 1 m downstream

acting as a guard slit. Due to the slight angular divergence of the beam, by the time the beam reaches the sample, it has expanded to a much larger size than originally set by the beam defining slits. (A beam that was defined to be 50 μm wide at the first slits expanded to about 300 μm wide at the sample position!) Such a large beam increases the timing dispersion. It also creates excess background scatter because it is larger than the sample jet, and therefore scatters off of the reactant solution surrounding the sample jet, or even off of the edges of the sample cell.

To minimize this beam expansion, it is necessary to move the beam defining aperture close to the sample. However, the tungsten beam defining slits produce too much parasitic scatter to use without guard slits. If the beam defining and guard slits are placed close together, the guard slits must be about the same size as the beam defining slits to clean up the low angle parasitic scatter. Not only does this make cleaning up the beam more challenging than when the slits are far apart, but any small motion of the beam creates changing amounts of parasitic scatter from the guard slits, interfering with background subtraction.

Recent advances have allowed the production of X-ray apertures and slits from single crystal materials such as germanium or tantalum [28]. These single crystal surfaces, when polished smooth, produce very low amounts of parasitic scatter. To create a small, stable beam, a "scatterless" 50 μm tantalum pinhole was employed as the beam defining aperture (A017C023, SCATEX, Incoatec GmbH, Geesthacht, Germany). Figure 24 b) shows a modified beamline setup where the pinhole is used as the sole aperture. Figure 24 c) and d) compare detector images taken using both of these setups. The parasitic scatter produced by the tantalum pinhole alone is larger than that from the combination of slits, but is much less than that produced by the beam defining slits alone. It can be used as the sole aperture, placed just a few inches away from the sample position, resulting in a smaller beam and less background scatter from the reactant sheath or the sample cell. Figure 25 shows less mid- and high-q scatter when using the pinhole setup due to this background reduction. Additionally, the lack of a second, closely sized guard aperture prevents changes in parasitic scatter due to small beam motions.

Therefore, the tantalum pinhole creates the small, stable beam necessary for these time-resolved experiments.

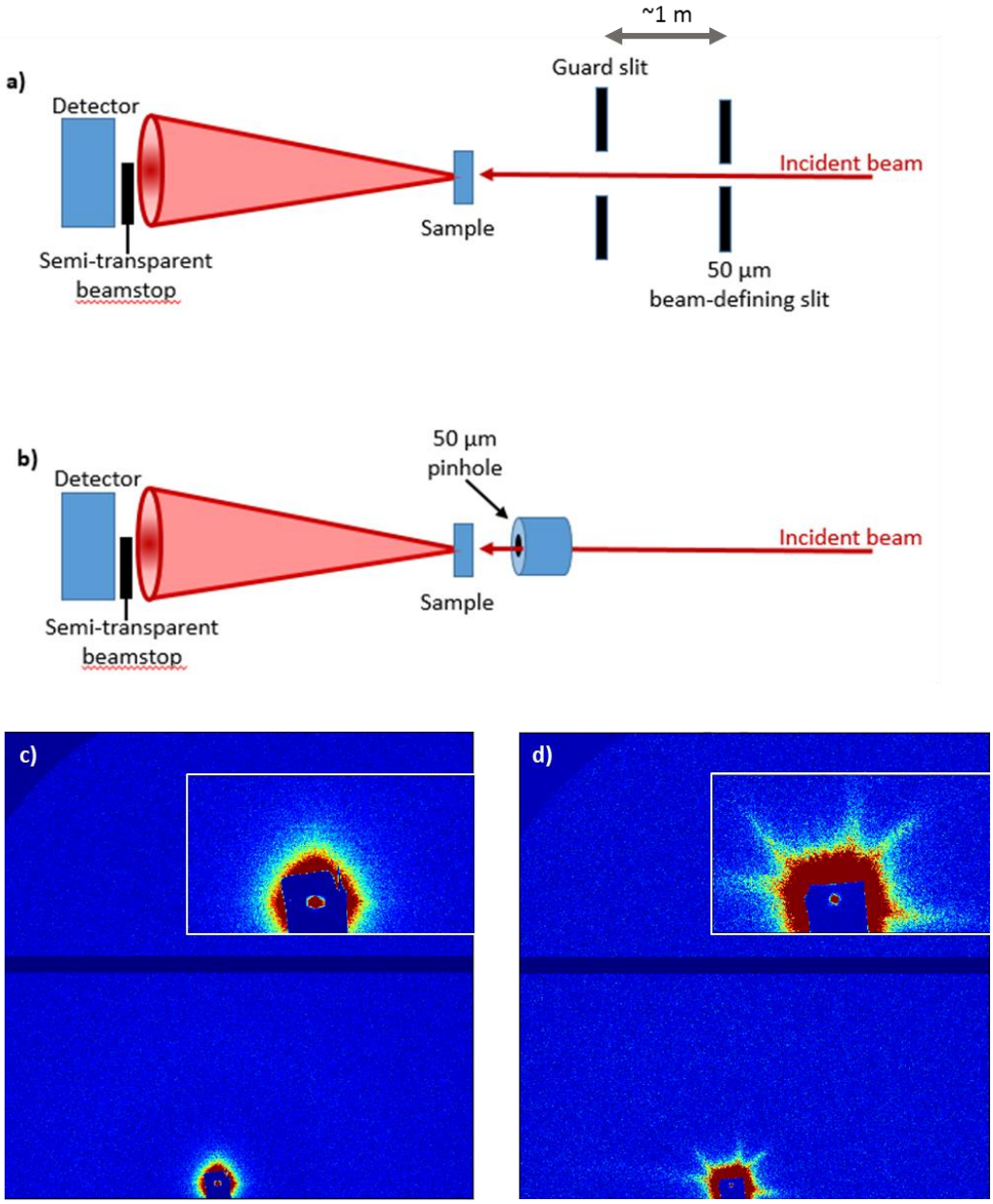

Figure 24. Comparison of beamline setups using two sets of tungsten slits or one "scatterless" tantalum pinhole. a) Schematic of the standard G1 setup, with the two sets of slits. b) Schematic of the modified setup, with the pinhole as the sole aperture. c) Detector image showing the scatter produced by the two sets of slits. Inset shows a closeup of the beamstop. d) Detector image showing scattering produced by the pinhole, with inset closeup of the beamstop. The sample (water in a polyimide sample cell) and exposure times were the same in parts c) and d). Images are normalized by the transmitted intensity.

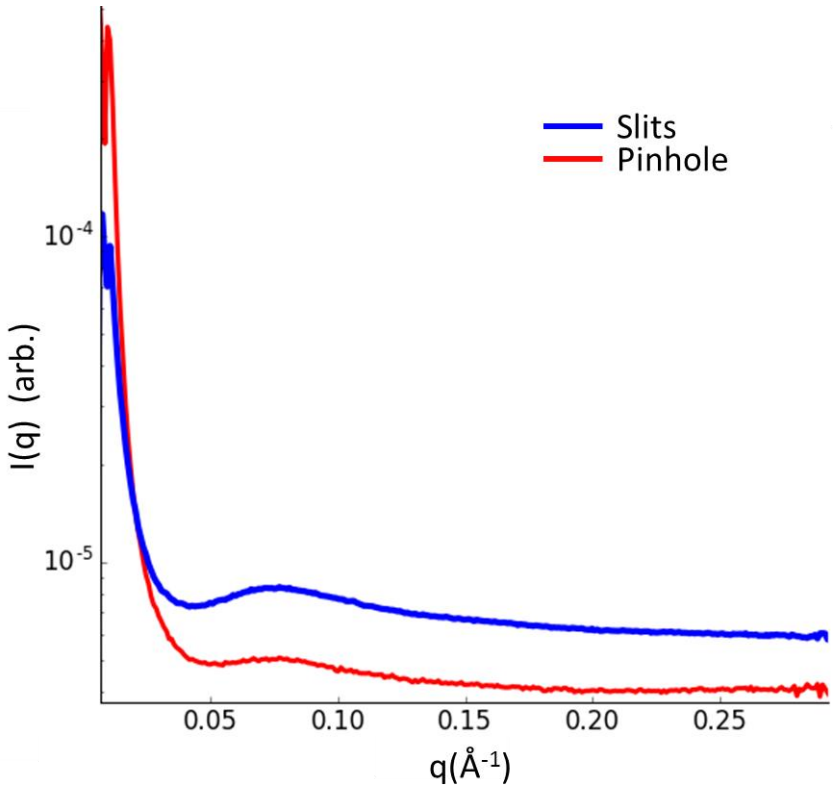

Figure 25. Comparison of transmission-normalized scattering from water in the conventional G1 setup with slits and the modified setup with the pinhole. The intensity is plotted in log scale to emphasize the improvements in high angle background scatter when the pinhole is employed.

4.3.2 Improvements to low angle scatter with a "scatterless" Ge guard slit-blade

While the tantalum pinhole produces a much smaller and more stable beam than the tungsten slits from the standard setup, it is far from a "scatterless" aperture. Detector images (Figure 24 d) show that the pinhole produces very bright low q parasitic scatter as well as bright jets that emerge from the beamstop. These jets can be masked out according to the procedure described in Chapter 3 for CryoSAXS. However, the isotropic bright low q scatter cannot be masked and interferes with the signal from biomolecules.

To reduce this low q scatter, a "scatterless" germanium slit-blade was added to complement the pinhole, Figure 26 a). The slit-blade was produced following a slightly modified version of the

procedure described by Li et al [28]. For this slit, the knife edge surface used to intersect the X-ray beam was polished to an optical mirror surface on an 8” Multiprep electron microscopy polishing wheel (Allied High Tech Products, Inc, Los Angeles, CA). The short attenuation length of germanium (~10 μm at 11.3 keV) makes it a very effective absorber of parasitic scatter. Due to the relatively low intrinsic scatter of the tantalum pinhole, the beam can be effectively cleaned up even when the pinhole and germanium slit-blade are just a few inches apart, as shown by the scattering profiles in Figure 26 b).

The single crystal nature of the guard slit-blade also results in enhanced background stability relative to using the standard tungsten guard slits. The germanium does not produce much parasitic scatter, so the measured scattering profiles are less sensitive to the small changes in beam angle which created different parasitic scattering backgrounds from the tungsten slits used in the standard setup.

Due to the absence of a second, opposing blade, this simple slit-blade only eliminates parasitic scatter in one direction. Therefore, the beam is most effectively used when positioned along the narrow edge of the detector, where the perpendicular parasitic scatter can be masked out without dramatically reducing the detector surface, as shown in Figure 26 c).

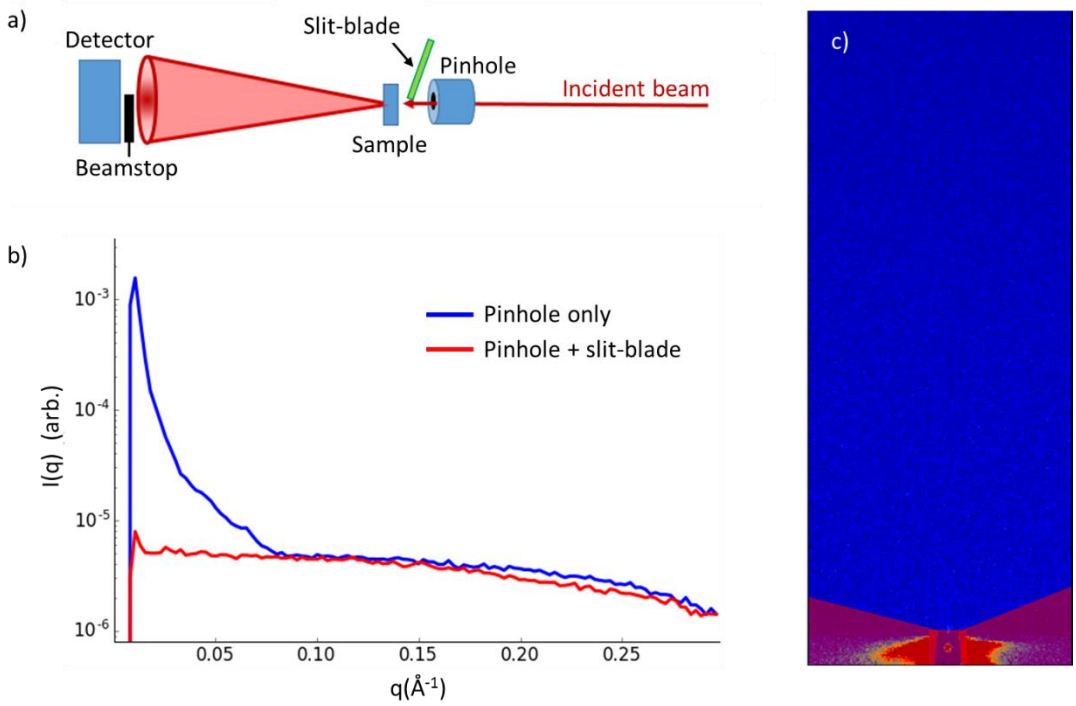

Figure 26. Addition of a germanium slit-blade to improve low angle parasitic scatter. a) Beamline schematic. The slit-blade is angled to reduce grazing incidence scatter off of the flat edge. b) Comparison of background scattering profiles with and without the slit-blade employed. No sample cell was present for these exposures. c) Detector image showing optimum placement of the beam along the narrow edge of the detector, as well as the mask used to remove low *q* scatter not blocked by the slit-blade (red overlay).

4.3.3 In-vacuo positioning of pinhole, slit, and mixer

The majority of previous continuous flow time-resolved SAXS experiments have been performed with the mixer located in a small air gap between vacuum flight tubes, similar to the setup discussed for cryoSAXS experiments above. This makes it easier to fabricate the mixer, since it need not be vacuum compatible, and easier to scan the mixer through the beam to access different delay times. However, the air gap and associated vacuum windows create excess background scatter. Therefore, to achieve optimal conditions, the entire flight path must be under vacuum in a high-signal-to-noise continuous flow setup.

This creates several complications for the experiment. The pinhole, the slit, and the mixer must all be placed under vacuum, with no gaps or windows between them. They must all be separately positionable, under motorized control, from outside of the hutch without breaking vacuum. The mixer must be able to move by relatively large distances (at least 0.5 inch) to access all of the desired delay times.

An overview of the beamline setup engineered to accommodate these three moving parts is shown in Figure 27. A 6 x 6 x 6 inch cubic vacuum chamber (P106861 frame, P106862 blank wall, P106863 KF-40 walls, P107296 KF-50 walls, and P106869 viewing window plate, Ideal Vacuum Products, Albuquerque, New Mexico) was purchased to provide a suitably sized vacuum space for all components, allowing them to access their necessary range of motion.

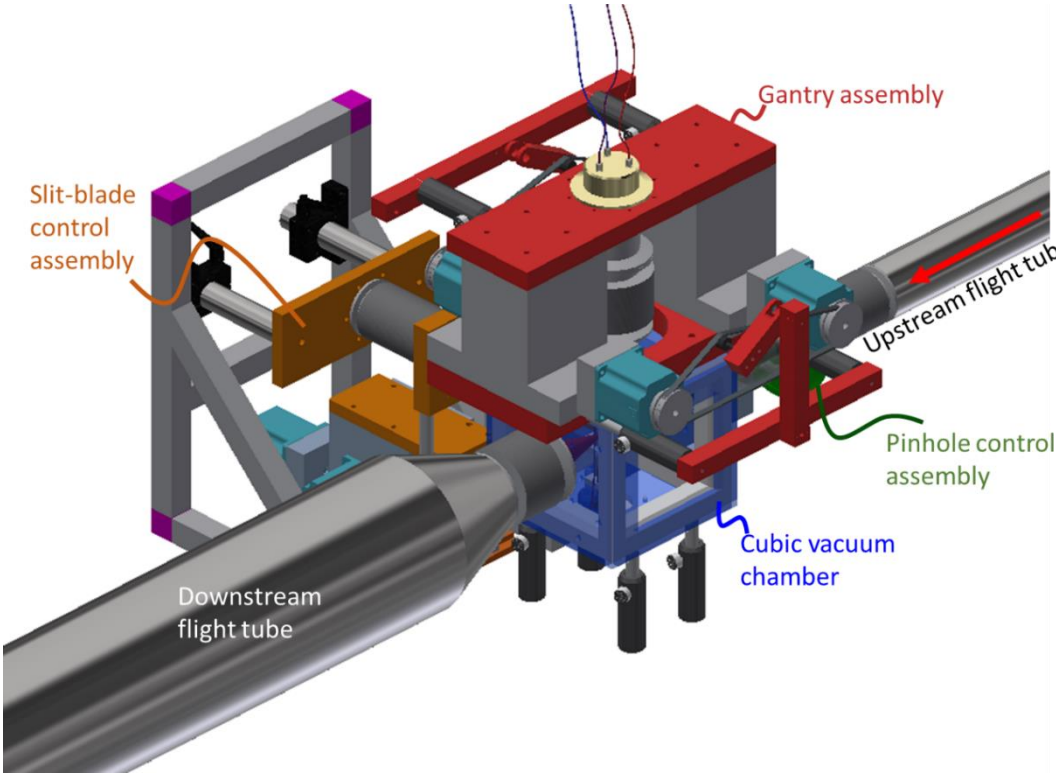

Figure 27. CAD overview of the beamline setup. Different systems are color coded to aid the eye and shown isolated in more detail below. CAD images produced using Autodesk Inventor 2018 (Autodesk, Inc., San Rafael, CA). See http://hdl.handle.net/1813/57588 for more detailed drawings of this assembly.

Figure 28 shows the arrangement of critical components inside the chamber. The slit-blade is mounted on a rod-and-plate assembly for manual 3 axis rough positioning. The slit-blade is located near the center of the chamber, as close to the mixer as possible without the risk of interference. The pinhole is positioned a couple of inches away from the slit-blade. No large dependence of background scatter on the separation between pinhole and slit-blade was observed.

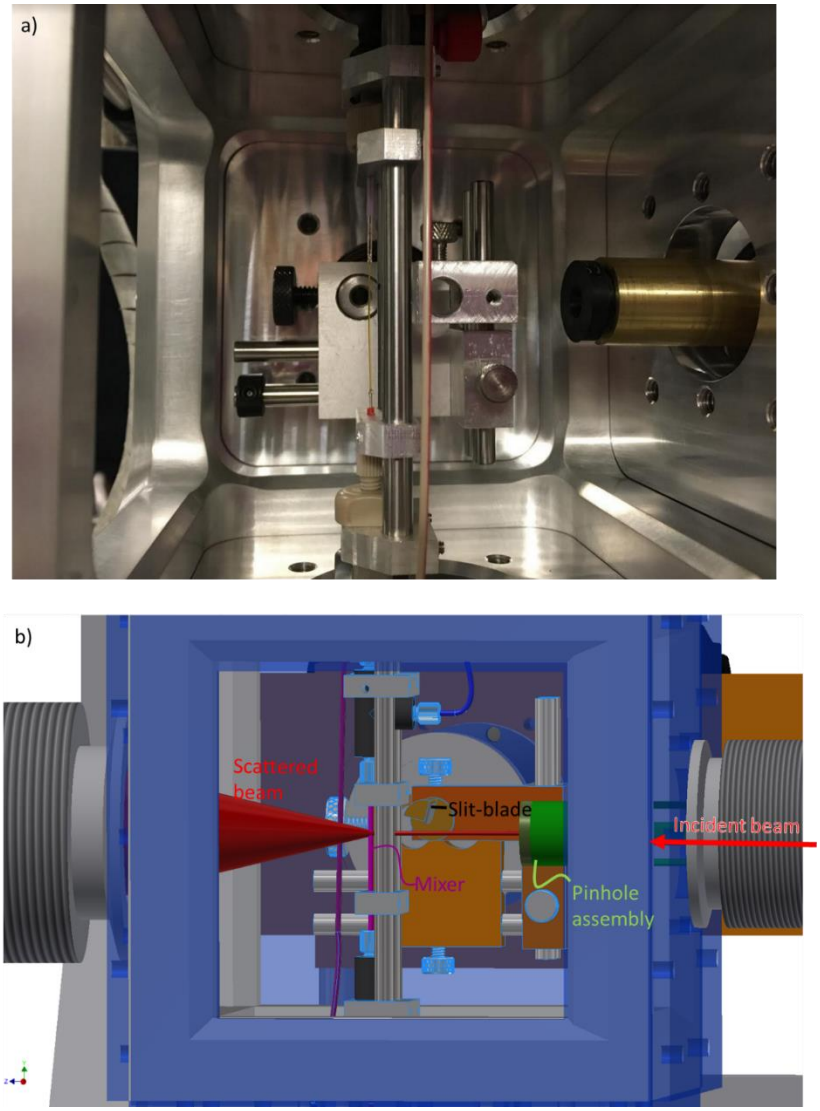

Figure 28. Arrangement of components inside the cubic vacuum chamber. a) Photo of the actual beamline setup. The slit-blade was not installed at the time the photo was taken. b) CAD view of the chamber, with parts labeled. The X-ray beam is drawn in red to guide the eye. See http://hdl.handle.net/1813/57588 for detailed drawings.

A gantry system composed of two CHESS XZ stages driven by stepper motors was used to position the mixer inside the chamber. The gantry is necessary to prevent torques on the XZ stages, which have low bending stiffness. Figure 29 a) and b) shows the gantry assembly. The two XZ stacks are mounted to a thick aluminum plate attached to the top of the cubic vacuum chamber, one on each side. Another plate spans the top of the motor stacks. This plate is drilled to accommodate a vacuum bulkhead connection in the center. A flexible vacuum bellow with KF-50 flanges (drawing number 32249, Metal Flex Welded Bellows, Inc., Newport, VT) connects the bottom of the plate to the cubic vacuum chamber.

To eliminate the risk of the gantry binding up due to unequal motions of stages on either side of the chamber, the two X stages and the two Z stages were coupled together by timing belts. Only one XZ stack is driven electronically; its motion is translated to the other stack through the belts. To prevent slippage of the timing belt and lag when changing motion directions, a threaded track roller was used as a tensioner. Unfortunately, the motor shafts that the timing belt pulleys attach to are slightly bent, resulting in a slight variation in the tension the belt is under at various points in the pulley's revolution. To eliminate this effect, a torsion spring was employed to adjust the height of the track roller to produce constant tension on the timing belt.

The mixer attaches rigidly to a KF50 vacuum stub, (QF50-200-UA, Kurt J. Lesker Company, Jefferson Hills, PA), which bolts to the top of the spanning plate. The flange has been drilled to accommodate standard microfluidic fittings (P-844 and P-840 VacuTight fittings, or P-251 and P-250 Super Flangeless fittings, IDEX Health & Science, Oak Harbor, Washington), which form vacuum-tight liquid feedthroughs through the flange. Figure 29 c) shows the details of the attachment. The mixer can be quickly removed by disconnecting the flange from the gantry. A standard static SAXS sample cell can also be mounted from the same flange, allowing straightforward measure of scattering profiles from the starting or ending states of a reaction.

The gantry can translate the mixer over an inch in the vertical direction without overcompressing the bellow, allowing great flexibility in the range of timepoints that can be probed. Horizontal motion is more limited due to the potential for interference between the mixer support rods and the inside of the bellow, but the mixer can safely be translated over 0.25” in the horizontal direction, which is more than sufficient to position the center of the mixer in the beam

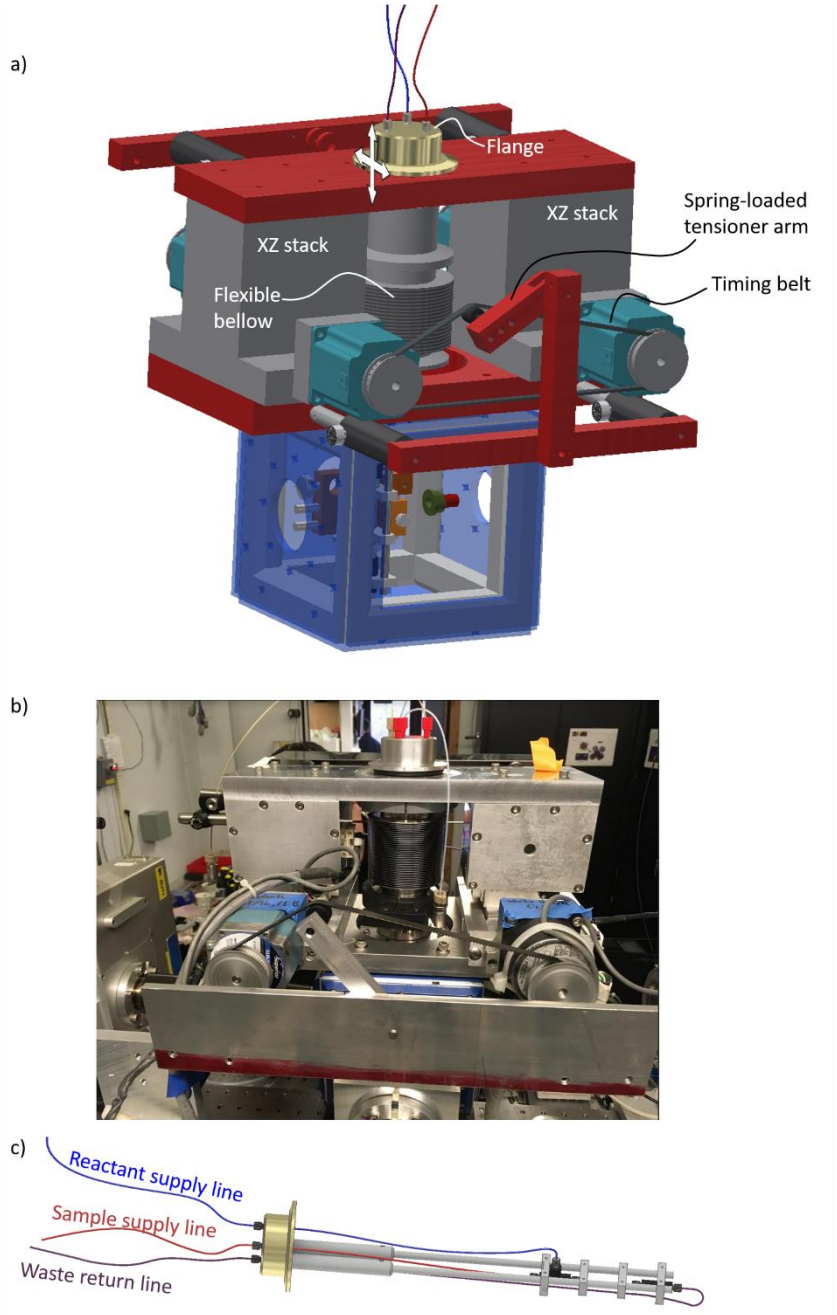

Figure 29. Gantry assembly. a) CAD overview of the assembly showing critical components. The timing belt assembly is repeated on the back side of the gantry to link the opposite set of motors. b) Beamline photo. c) CAD illustration of the connection between the mixer and the KF50 flange. See http://hdl.handle.net/1813/57588 for detailed drawings.

The assemblies that control the positions of the slit-blade and the pinhole are shown in Figure 30.

Each component is controlled by a single XZ motor stack. Both the slit-blade and pinhole attach rigidly

to an aperture mounting plate bolted to their respective motor stacks. These mounting plates are connected to the vacuum chamber by flexible KF-40 vacuum bellows (part number 18913AA-6.8, Metal Flex Welded Bellows, Inc., Newport, VT). The bellows allow the motor stacks to position the slit-blade and pinhole while under vacuum.

The motor stacks have very low stiffness when a torque is applied, and therefore it is important to balance the forces applied to the motor stack. To eliminate torque on the slit-blade stack, an additional KF-40 vacuum bellow connects the other side of the mounting plate to a rigid aluminum brace. The mounting plate therefore feels a vacuum force from either side, allowing the motor stack to move smoothly without experiencing a torque. Eliminating the load on the pinhole's motor stack is straightforward: the mounting plate is connected by the flexible KF-40 bellows to both the cubic vacuum chamber and to the upstream flight tube. The X-ray beam passes directly through the center of the pinhole's mounting plate.

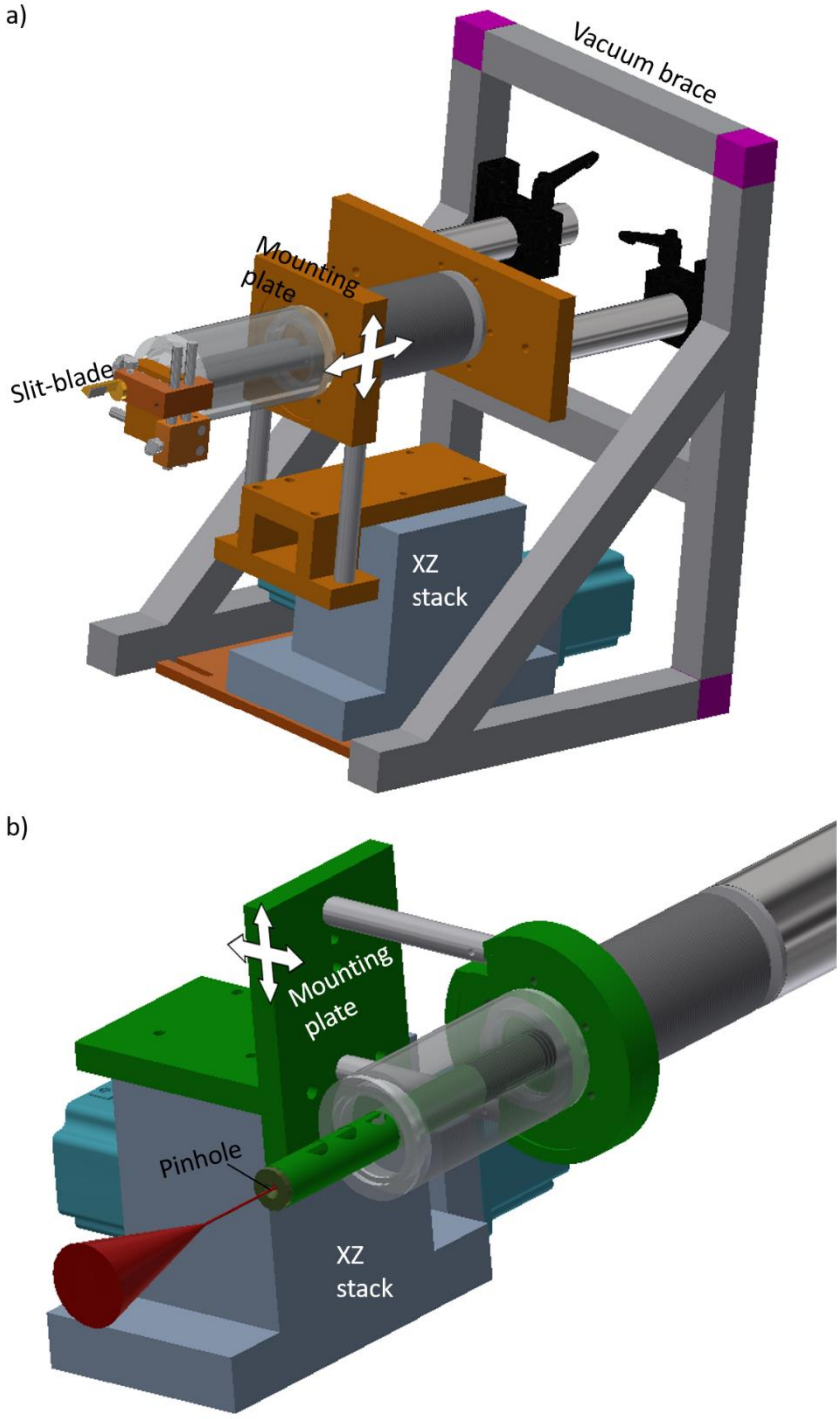

Figure 30. Details of the slit-blade and pinhole control assemblies. a) Slit-blade assembly. The bellow that attaches to the cube has been made transparent to show the connection of the slit-blade to its mounting plate. b) Pinhole assembly, with the bellow that attaches to the cube made transparent to show the pinhole's connection to the mounting plate. See http://hdl.handle.net/1813/57588 for detailed drawings.

4.3.4 Alignment and mixer operation

The first step in setting up the beamline for this experiment was to align the cubic vacuum chamber and flight tube such that the X-ray beam passed through the center of the chamber and hit the semi-transparent molybdenum beamstop with no apertures or mixer in place. The chamber and flight tube were rigidly secured, and the detector positioned such that the transmitted beam was located along the center of the detector's bottom edge. The pinhole was then inserted into the chamber and scanned in to maximize the transmitted beam counts measured by the detector. Then, the guard slit-blade was scanned vertically to find the optimal position where the main beam was not clipped by the guard slit, but the parasitic scatter produced by the pinhole was absorbed. With the apertures aligned, the mixer was scanned in to locate both the center of the mixing channel and the snout of the constriction, which corresponds to time = 0. From there, the mixer could be positioned to access the delay time of interest.

A multichannel pressure controller (OB1, 0-8000 mbar range, Elveflow, Paris, France) and two flow meters (either two MFS2 (0.3-7 µL/min range) or one MFS2 and an MFS3 (2-80 µL/min range) depending on conditions, Elveflow) were used to drive and measure the liquid flows through the mixer. A PID feedback loop between the flow sensors and pressure controller was employed to keep the flowrates as constant as possible, which is important for proper background subtraction. To obtain the background data (scattering from the reactant solution alone), it is possible to set the sample flow rate to 0 µL/min, so that the entire mixing channel is filled only with reactant solution. This is an acceptable solution if the reactant is small and does not contribute appreciably to the background scatter. However, if the reactant scatters more strongly, this method will lead to incorrect subtraction, since there are different amounts of reactant present in the channel depending on whether or not the sample is flowing. In this case, it is more beneficial to use an HPLC-style injection valve (MXP7900, IDEX Health & Science, Oak Harbor, Washington) to switch between flowing sample or buffer through the central channel of the mixer.

4.4 Time-resolved SAXS experiments on rRNA and tP5abc

This new mixing technology was employed to study two small, RNA three-helix junctions which fold in the presence of Mg^{2+}: the GTPase Center of 23S rRNA (referred to as rRNA for the rest of this chapter), and tP5abc, a truncated subdomain from the *Tetrahymena* ribozyme. In both cases, RNA flowing in the central channel was focused into a thin jet by a Mg-containing buffer. These experiments were carried out at Station G1 at CHESS, with a beam energy of 11.18 keV and the beamline setup described above. Scattering images were acquired using an Eiger 1M detector (Dectris, Baden, Switzerland). These data were collected before the implementation of the Ge slit-blade, and used the tantalum pinhole as the sole aperture.

4.4.1 Flow parameters and Mg^{2+} concentrations

This section is based on the supplementary information of Ref [77].

The delay times of interest for these experiments ranged from 10 ms to several seconds. To access such a wide range of timepoints, three different flow schemes were used. In each case, the [Mg] in the reactant solution was adjusted to maintain the desired average [Mg] in the sample jet at the end of the constriction, and therefore throughout the observation region. The final [Mg] for the tP5abc experiments was chosen to be 1 mM. The final [Mg] for the rRNA experiments was 10 mM.

Table 1 shows the flowrates and timing dispersions for each timepoint probed, as well as the [Mg] concentration in the reactant solution, for the tP5abc experiment. The total dispersion listed here is the beam smearing and flow dispersion added in quadrature.

Table 1. Flow parameters and dispersions for the timepoints probed. The [Mg] listed here are for the tP5abc experiment. The rRNA experiment used 10 times higher [Mg]. Table from Ref [77].

	Timepoint (ms)					
	10	30	100	300	1000	3000
Sample Flow Rate (µL/min)	5	5	5	1.7	1.7	1.7
Total flow rate (µL/min)	36.4	17	17	5.7	5.7	5.7
Time in constriction (ms)	3.5	7.5	7.5	22.5	22.5	22.5
Flow Dispersion (ms)	1.1	7.6	19.8	61.5	183.3	531.3
Beam Smearing (ms)	2.5	5.4	5.4	16	16	16
Total dispersion (ms)	±1.4	±4.7	±10	±30	±90	±270
Sample Path Length (µm)	80	148	148	148	148	148
Outer flow [Mg^{2+}] (mM)	2	2	2	1.5	1.5	1.5

Magnesium diffusion was simulated using COMSOL Multiphysics software, version 4.2 (COMSOL, Inc., Burlington, MA). The diffusion coefficient of Mg^{2+} was taken to be (1×10^{-9}) m^2/s, which is intermediate among the range of values reported in the literature [78], [79]. Figure 31 a) shows the simulated [Mg] (averaged over the intersection volume of the X-ray beam and the sample jet) for each delay time. The simulations accounted for both the shape of the intersection volume, and for the cylindrical shape of the sample jet, which results in unequal weighting for different points across the radial profile. Figure 31 b) shows the [Mg] concentration in a radial slice through the sample jet, displaying the concentration extremes experienced by some molecules in the center or on the edges of the jet.

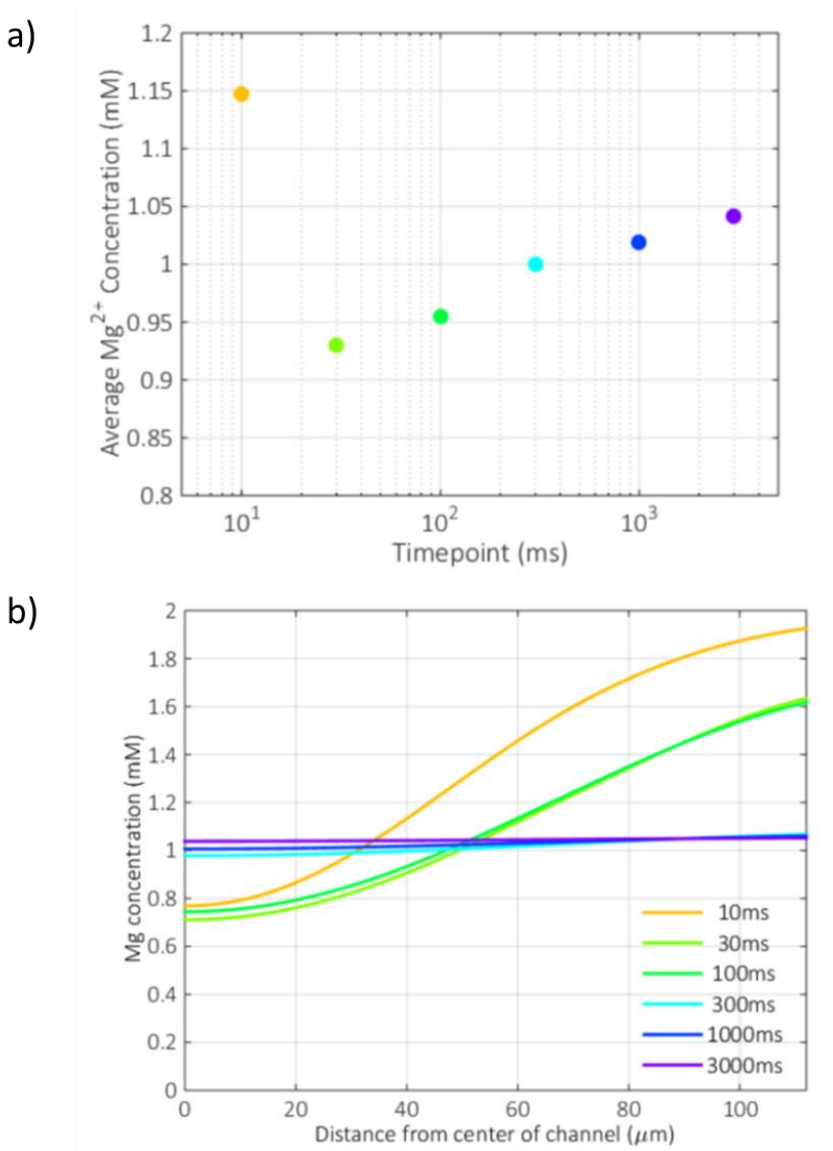

Figure 31. [Mg] in the sample-containing jet for the tP5abc experiment. a) Average [Mg] for all of the delay times probed. b) Radial [Mg] profiles. Note that the sample-containing jet ends at ~40 μm from the center of the channel for the 10 ms delay time, and ~70 μm from the center of the channel for all other delay times. The [Mg]s for the rRNA experiments are higher by a factor of 10, but the profiles have identical shapes. Figure from the Supporting Information of Ref [77].

4.4.2 Assessment of signal to noise and sample consumption

The initial assessment of the mixer's data quality was performed by measuring the initial, "unmixed" state, by flowing the same buffer that the biomolecules were solvated in (containing K^+ as a charge compensating salt, but no Mg^{2+}, which is required to fold this RNA) in the outer channel of the mixer. Figure 32 shows a comparison of these unmixed scattering profiles measured in the mixer with those measured in a static sample cell. In this figure, each profile is the result of 50 s of data collection. The signal to noise ratio of the two profiles is comparable even with the much shorter X-ray pathlength of the mixer, due to the fact the fast flow speed through the mixer (cm/s) meant that no attenuators were needed to prevent radiation damage. In contrast, molybdenum attenuators were required to prevent radiation damage in the static cell. Therefore, despite its much longer X-ray pathlength, the static cell does not produce higher signal-to-noise data than the mixer.

Additionally, the mixer used less sample than the static cell, even for the relatively long acquisition times (250 s) used to obtain the publication quality data in Ref [77]. At the highest sample flow rate, 5 μL/min, 250 s of flow uses a total of 21 μL of sample. In contrast, the static cell requires 30 microliters of sample regardless of the data collection time. Therefore, high signal-to-noise data can be acquired in this mixer, with a sample consumption per delay time lower than that needed for a normal static sample.

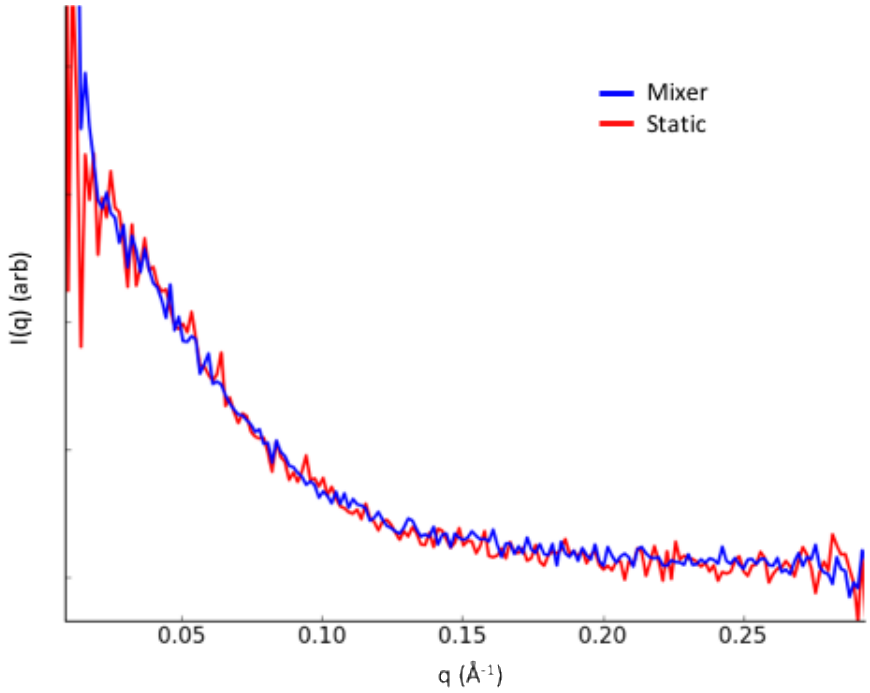

Figure 32. Comparison of scattering from rRNA in the mixer and in a static sample cell. Here, each curve is the result of 50 s of collection. Curves used for analysis shown below resulted from 250 s of collection.

4.4.3 Characterization of setup repeatability and robustness

Two reproducibility tests were employed to ensure proper functioning of the mixer and gantry setup. In the first test, shown in Figure 33 a), the 100 ms delay time was probed at two different times, about an hour apart, with a measurement at the 30 ms delay time in between. Scattering profiles were reproducible between the two trials, despite mixer translation and the elapsed time. The profile for the 30 ms delay time is significantly different, giving even more confidence that the mixer can be reproducibly positioned and does not experience any kind of "drift" in flow conditions.

In the second trial, two different sets of flow conditions that should theoretically produce the same delay time (but at different delay lengths) were probed. Figure 32 b) shows reproducible scattering profiles between these flow conditions. Small differences observed between these profiles may result from uncertainty in the diffusion coefficient for Mg^{2+}.

The reproducibility of the scattering profiles across time, positioning, and flow conditions produced a high level of confidence in the repeatability and robustness of the apparatus.

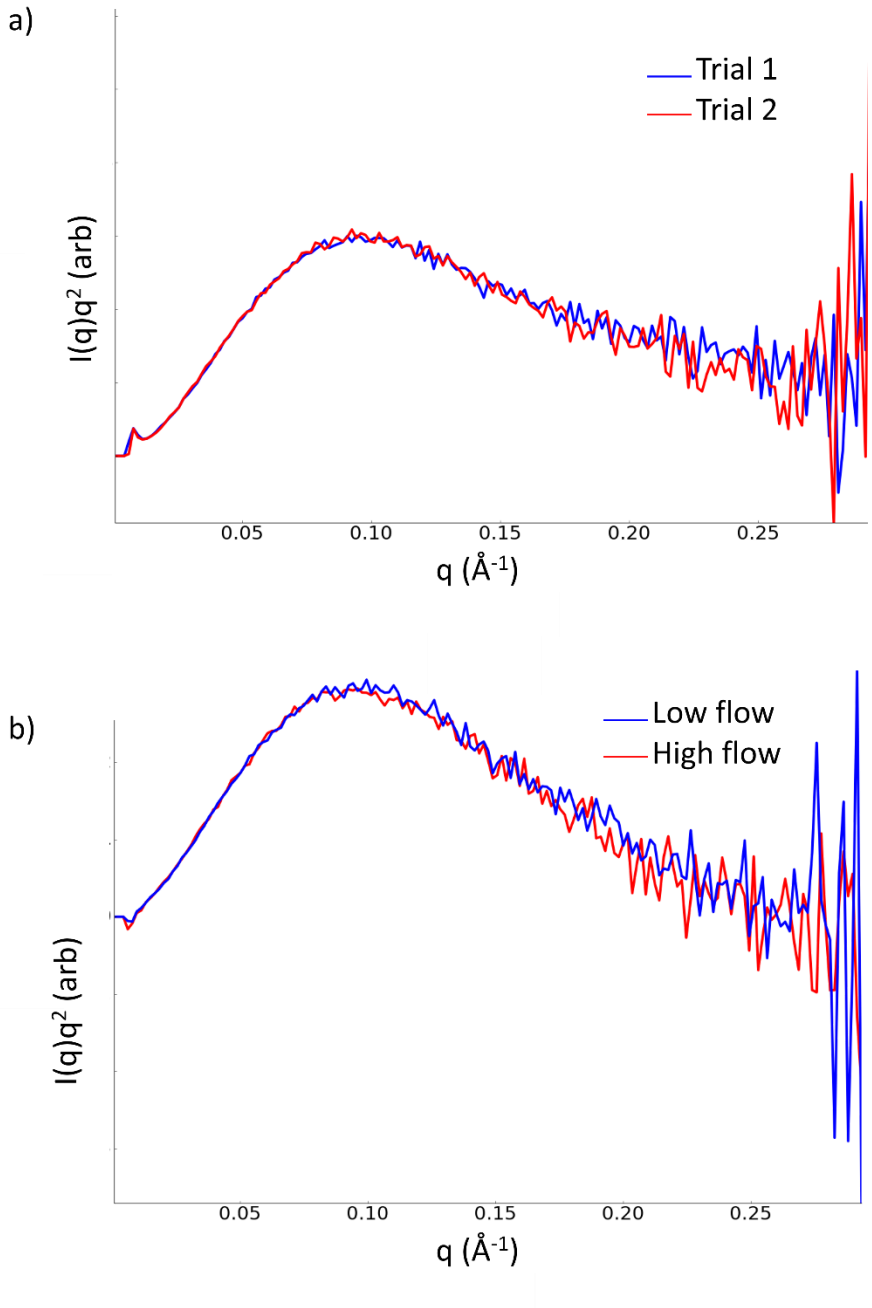

Figure 33. Kratky plots demonstrating reproducibility of scattering profiles from rRNA samples in the mixer. a) Two trials of the 100 ms delay time, separated by ~1 hour and a measurement at a different delay time. b) Profiles with a 300 ms delay time created by two different flow conditions.

4.4.5 Summary of tP5abc results

This thesis focuses on novel instrumentation, and it is beyond the scope to describe in detail the ensemble analysis method used by Alex Plumridge to interpret this data. Nevertheless, Figure 34 gives a brief summary of the results obtained from the tP5abc mixing experiment. The changing shape of the Kratky profiles at different delay times (shown in Figure 34 a)) indicates a rich progression of intermediate states after the addition of Mg^{2+} to the unfolded RNA. An initial electrostatic collapse at the shortest timepoints is followed by an expansion, then a second collapse before reaching the native state. Ensemble analysis compares the scattering profiles from each delay time to those generated by a vast pool of molecular models, and determines a model subset that best fits the data. The chosen atomically detailed structures can be used to gain more insight into the states of the RNA molecules at each delay time, as shown in Figure 34 b). This technique provided insight into the folding mechanism for this three helix junction, a ubiquitous RNA motif. This knowledge may be transferable to other RNAs or help improve our molecular dynamics force fields. The experiment revealed an array of structural intermediate states and their roles in the folding pathway, and provided insight into the role of Mg^{2+} in orchestrating tertiary contact formation and molecular collapses. For a full discussion of these results and their implications for RNA folding, see Reference [77].

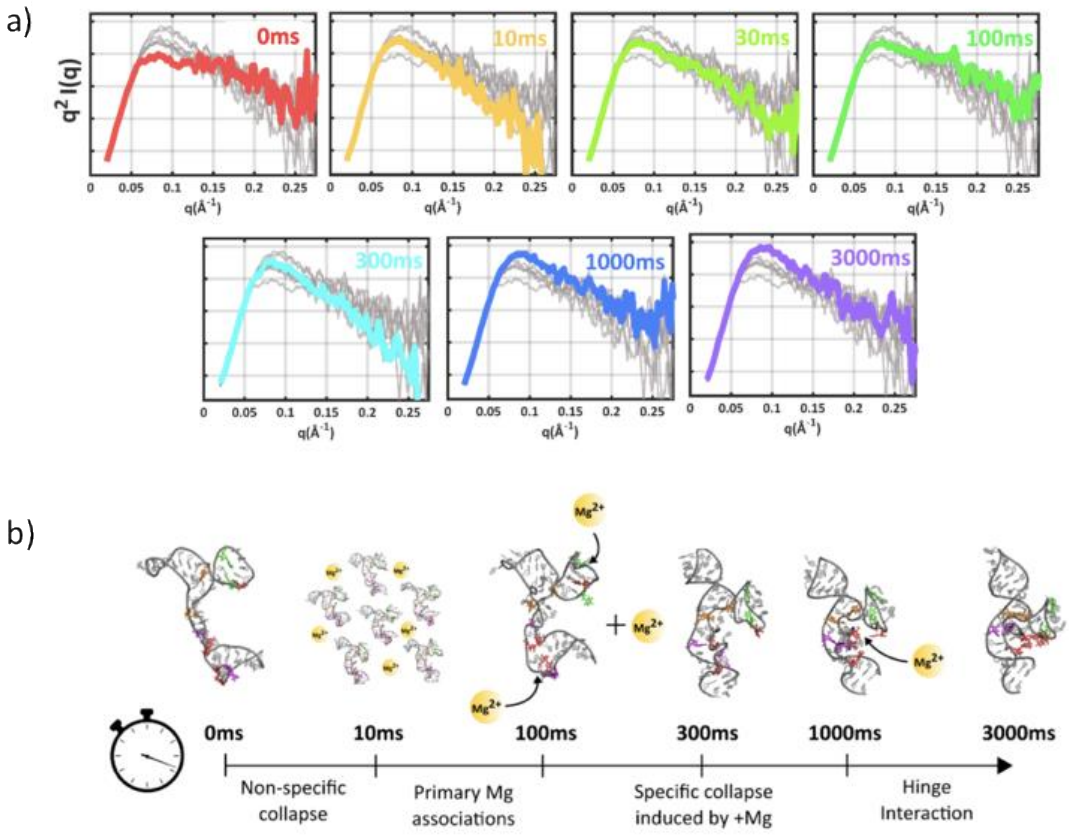

Figure 34. Summary of results from tP5abc experiment. a) Kratky plots of each delay time probed. In each plot, the profiles for all of the other delay times are grayed out in the background to guide the eye to subtle changes between delay times. b) Representative structures chosen by the ensemble modeling technique for each delay time. The orange spheres represent Mg^{2+} ions, and arrows show the location of their suspected interactions with the RNA molecule. Figure adapted from Ref [77].

4.4.6 Summary of rRNA results

The rRNA results from the initial experiment looked very similar to those for tP5abc: the same trends were observed in the Kratky tails at the same delay times. However, when the experiment was repeated at a subsequent beamtime, the results were different. Variations between delay times were much more subtle, and in general the molecule always appeared more compact. Careful comparison of molecules' initial states between the two beamtimes showed a slight difference: at the second beamtime, the rRNA started out a little more compact than in the first. These experiments highlight the rugged landscape of RNA folding. The same molecule, starting from slightly different initial states,

may not follow the same folding pathways. A well characterized, reproducible initial state is essential for understanding the results of these experiments and for comparing with data obtained from other time-resolved methods.

4.5 Outlook and challenges

The new cylindrical SAXS mixers and fully in-vacuum beamline setup allow the acquisition of high quality time-resolved SAXS data from small sample volumes. This increases the number of delay times that can be measured in a given amount of beamtime while decreasing the sample cost per timepoint. Therefore, these advances make time-resolved SAXS a more efficient technique in terms of both time and money.

The beamline setup described in this chapter is challenging and time consuming to assemble, and cannot be put together in advance of the beamtime due to many components being linked by flexible vacuum bellows and the dependence on CHESS-owned motor stacks. The assembly process wastes valuable experimental time if pre-beamtime access to the hutch is not available. Future modifications (discussed in Chapter 5) will make the setup smaller and more portable, and make this technique more accessible for smaller teams or for those with limited beamtime.

This TR-SAXS technique provides new opportunities to observe reactions initiated by small molecules or ions, which can rapidly diffuse across the sample jet. However, many systems involve reactants that diffuse more slowly, resulting in a large timing dispersion and decreasing the occupancies of transient intermediate states. Therefore, there are several interesting reactions, such as those between two proteins or between proteins and nucleic acids, which cannot be studied in this mixer. Additionally, it will not effectively mix viscous solutions such as the cryoprotectant buffers that would be necessary for time-resolved cryoSAXS. Therefore, diffusive mixing technology is limited in application. Chapter 5 describes an adaptation of this mixer, which integrates a chaotic

advection mixing element to handle mixing experiments with systems containing slowly diffusing molecules.

CHAPTER 5

CHAOTIC ADVECTION MIXER FOR LOW SAMPLE VOLUME TIME-RESOLVED SAXS ON SLOWLY DIFFUSING SYSTEMS

The work presented in this chapter was performed in close collaboration with George Calvey. Juraj Knoska (CFEL) made the 3D-printed mixing inserts. Suzette Pabit made the protein samples. Josue San Emeterio created software to control the syringe pumps and switching valves.

Detailed drawings for custom parts described in this chapter can be found at Cornell's eCommons, (http://hdl.handle.net/1813/57588). All custom parts were designed and drawn by George Calvey and me.

5.1 Introduction

5.1.1 Why mix via chaotic advection?

The diffusive mixer presented in Chapter 4 provides great opportunities for high quality time-resolved SAXS data on systems in which one reactant is a very small molecule, such as an ion. These small reactants diffuse quickly across the hydrodynamically focused sample stream to initiate the reaction.

However, a great number of interesting and important biochemical reactions occur between larger molecules, such as two proteins or a protein and a nucleic acid. The diffusion of even a small protein is much slower than an ion (protein diffusion coefficients are ~10^{-11} m^2/s [80], compared to ~10^{-9} for Mg^{2+} [78], [79]). Attempting to use a diffusive mixer to mix in such a slowly diffusing molecule would cause a large timing dispersion, decreasing the occupancy of transient intermediate states.

A second shortcoming of the diffusive mixer is its lack of suitability for samples solvated in a high viscosity buffer, since diffusion rates are inversely proportional to viscosity [81]. For example, the mixer described above cannot be used for the high percentage sucrose solutions necessary for time-resolved contrast variation SAXS, a technique used in the study of protein-nucleic acid interactions. Here, sucrose is added to the solvent until its electron density equals that of the protein. Therefore, scatter from the protein is effectively "blanked," leaving only the scattering from the higher density nucleic acid [82], [83]. A more effective form of mixing is necessary to minimize the timing dispersion when studying viscous systems such as these.

Two other common ways to effectively mix two fluids are mechanical actuation, such as stirring, or induction of turbulent flow. It is difficult to stir samples traveling through the small microchannels needed for a low volume time-resolved SAXS mixer, so this method has low applicability. Turbulent mixers hold more promise. Stopped flow mixers have already successfully been used in time-resolved contrast variation SAXS [82], [83]. However, they require large amounts of sample [20], and the captive molecules are susceptible to radiation damage at longer delay times. Turbulent, continuous flow SAXS mixers also exist [52], [84]. These mixers reduce radiation damage and use less sample than a stopped flow mixer. However, even the most sample-efficient devices still require 2-3 mg of sample per delay time probed [52]. Therefore, turbulent mixers are impractical for many biological reactions of interest which involve expensive molecules or those that are challenging to express in large quantities.

One way to avoid the challenges presented by turbulent mixers is to instead employ a *static mixer*, a device designed to efficiently mix two fluids in the laminar flow regime. A static mixer is composed of a fluidic channel containing carefully arranged geometric elements. These are designed to mix two liquids flowing through the channel by stretching the interfaces between them, splitting the flows apart, and then stacking them to create more interfaces than there were previously [85], [86]. This process, illustrated in Figure 35, is called a baker's transformation for its similarity to the motions of a baker

mixing and kneading dough. Several baker's transformations occur as the fluids travel through a static mixer: the flows are stretched, split, and stacked over and over, so that many alternating thin "strips" of each fluid are formed, and even large molecules or those in viscous solutions can diffuse rapidly across the interfaces. Mixing within this type of device is by nature chaotic: two particles that enter the mixer next to each other may diverge significantly in their paths as they travel through the mixer. Therefore, static mixers are chaotic advection devices.

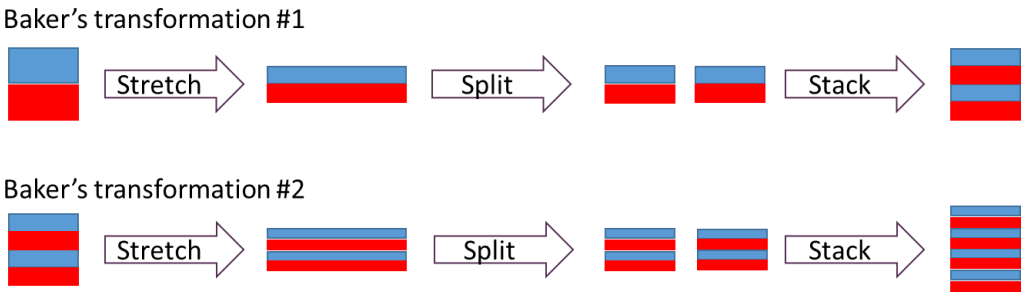

Figure 35. Illustration of the principle behind the baker's transformation. Each set of colored rectangles represents a cross section through a hypothetical mixing device containing a red fluid and a blue fluid, which are to be mixed. With each iteration of the baker's transformation, more interfaces are formed and the length scale of each block of fluid is decreased. Note that no material is lost in this process. A static mixer may produce many baker's transformations. Figure inspired by Ref. [86].

Static mixers are commonly used in the chemical, pharmaceutical, and food industries to blend viscous liquids, or in cases when stirring is undesirable [87]. These successful industrial designs can be scaled down and incorporated into microfluidic channels for efficient, laminar flow mixing of small volumes [87]. Such a device uses significantly less sample than a turbulent mixer, and its continuous flow nature would greatly reduce radiation damage in a SAXS experiment relative to a stopped flow mixer. Therefore, a scaled-down version of a successful industrial static mixer is ideal for a time-resolved SAXS experiment on slowly diffusing molecules.

5.1.2 The Kenics mixer

One of the more easily adaptable of the static mixers is the Kenics design (Chemineer, Dayton, Ohio), shown in Figure 36. In a Kenics mixer, short, helix-shaped elements with alternating left- or right-handedness are arranged in a pipe so that the trailing edge of one helix is perpendicular to the leading edge of the next [87]–[89]. As the fluids to be mixed flow through the pipe they encounter the helical elements, which cause baker's transformations: the flow trajectories are impacted to stretch, fold, and stack the interfaces between the fluids.

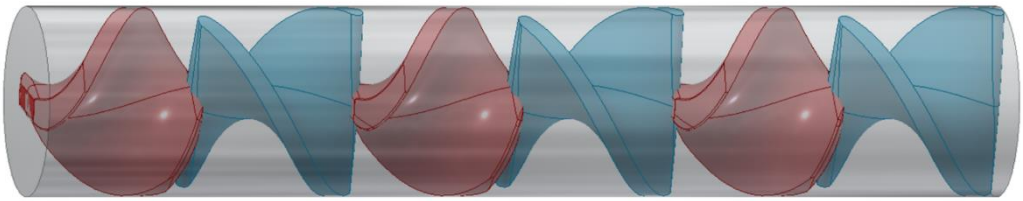

Figure 36. CAD illustration of a Kenics mixer. The cylindrical pipe through which liquid flows is drawn in transparent gray. The alternating colors of the interior helical elements indicate their opposite helicities.

The Kenics mixer is extremely versatile. The aspect ratio, twist angle, and number of helical elements can be modified to optimize the mixer for the fluids of interest [88], [90]. Additionally, the Kenics design does not have the small, clog-prone channels present in scaled-down versions of some other types of industrial static mixers, making it a robust choice for these experiments.

5.2 Mixer design and fabrication

5.2.1 Evolution from the diffusive mixer

Several design elements were critical to the success of the diffusive SAXS mixer described in Chapter 4. First, the relatively large dimensions of the observation capillary allowed the use of a ~50 μm X-ray beam. The high flux of a beam this size (~10^{11} ph/s at Station G1 at CHESS) helped reduce

the acquisition time required to obtain high quality SAXS data relative to the ~μm sized beams commonly used with continuous flow devices. Second, the cylindrical geometry of the mixer allowed the sample flow to be fully sheathed by buffer flow. Sheathing reduced timing dispersion, since all of the sample traveled down the center of the channel rather than some crawling down the walls, and prevented radiation damage. The cylindrical geometry also simplified fabrication: the entire device was composed of robust glass capillaries, with no clean room fabrication required and only simple epoxy steps needed to seal the device. The ideal chaotic advection SAXS mixer preserves all of these qualities, while also including the appropriate number of static mixing elements for efficient mixing of slowly diffusing samples.

A straightforward way to preserve the beneficial characteristics of the previous mixer design while incorporating chaotic advection is to modify the first device to include a "mixing insert" that houses a static mixer. Figure 37 shows a conceptual idea of what such a mixer could look like. Two capillary supply lines, each containing one of the samples to be mixed, feed into the insert where the samples encounter the static mixing elements. The insert (with its attached supply lines) is housed inside of an observation capillary with low background scattering properties. A sheath liquid, such as water or a dilute buffer, flows around the insert to surround the mixed sample flow that leaves the insert. The sheath keeps the mixed flow centered in the observation capillary, reducing its timing dispersion. The complete device is very similar in outward appearance and geometry to the mixer described in Chapter 4, and can be interfaced to the beamline setup detailed there, with only slight modifications. Therefore, the main challenge of building a chaotic advection mixer for SAXS experiments is to design the mixing insert.

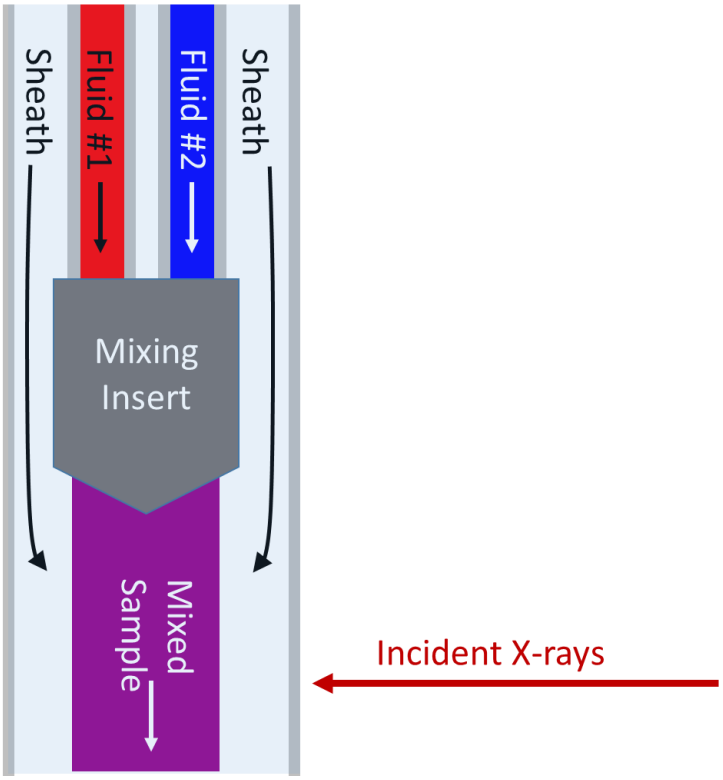

Figure 37. Concept of the chaotic advection mixer design. Two supply capillaries containing the fluids to be mixed (red and dark blue) feed into a mixing insert (gray). The insert combines the two fluids and facilitates a sheath flow (light blue) around the mixed sample (purple).

The requirements for the mixing insert are strict. First, it must contain the static mixer elements required to rapidly and effectively mix the two fluids. Second, the mixed solution must leave the insert with sufficient X-ray pathlength to achieve a good scattering signal. Third, the insert must also be shaped to allow the sheath fluid to flow around it and then to symmetrically surround the sample flow. However, the X-ray pathlength of the sheath cannot be significantly larger than the pathlength of the sample without creating large amounts of background scattering; the shape of the insert must facilitate this thin sheath. Additionally, the entire insert must fit inside the observation capillary. In principle, observation capillaries used for these experiments could be up to several mm in diameter. However, a large diameter capillary necessitates high sample consumption to reduce the timing dispersion, since sample flowing at a given mass flow rate takes longer to transit the X-ray beam in a larger diameter

tube. To keep sample consumption at a realistic level, the inner diameter of the observation capillary, and therefore the outer diameter of the insert, can be no more than ~500-600 µm.

The production of a ~600 µm outer diameter insert with complicated inner geometry containing miniaturized helical elements is daunting. However, recent developments in 3D microfabrication technology make the manufacture of such an insert possible. 3D direct laser writing is a fabrication method that uses two-photon polymerization of photopolymers such as SU8 to create solid parts with heights ranging from a few hundred nanometers to several millimeters, with submicron resolution [91], [92]. This technology is therefore ideal for creating the mixing inserts. Our collaborators in Henry Chapman's lab at the Center for Free Electron Lasers (Hamburg, Germany) have a commercial micro 3D printer (Photonic Professional GT, Nanoscribe GmbH, Stutensee, Germany) which makes use of this technology [93], [94]. Juraj Knoska printed the inserts for us.

The design for the mixing insert can be considered in two parts: the design of the structural part of the insert which interfaces the flows and houses the mixing elements, and the elements themselves. Both are discussed in detail below.

5.2.2 Structural insert design

There are three main roles of the structural part of the insert: it must facilitate a sheath liquid flowing symmetrically around the sample, it must provide ports for supply lines for the two fluids to be mixed, and it must house the Kenics static mixing elements.

Figure 38 a) shows a CAD rendering of the exterior of the 3D printed insert. The insert is designed with centering fins to hold it coaxially inside of the observation capillary. This geometry also allows space for the sheath liquid to flow around the insert, as shown in Figures 38 b) and c). The fins are sized for a 550 µm inner diameter observation capillary.

Figure 38 d) shows a cross sectional view of the insert. On the left are the supply line ports. These ports are each designed to accommodate a 200 μm outer diameter capillary, which can be glued into the insert with UV curable epoxy. Each port has two constricted regions. The first is shaped similarly to the centering spacers described in Chapter 4. It allows the epoxy to flow past while holding the capillary centered in the port. The second constriction is an extremely tight fit around the capillary. This constriction is designed to stop the epoxy flow and prevent it from clogging the insert's inner channels before the epoxy can be cured.

As shown in Figure 38 d), two interior channels direct the fluids from the supply lines to a ~1 mm long, 100 μm diameter channel which houses the Kenics mixing elements, discussed below. At the downstream end of the device, the chamber widens to a diameter of 250 μm, and contains an interior cross-shaped element designed to homogenize the flow so that it emerges from the insert fully developed and at its fully expanded diameter. This allows measurements of the full pathlength reaction mixture to occur with the beam positioned very near to the end of the insert, permitting the study of shorter timepoints.

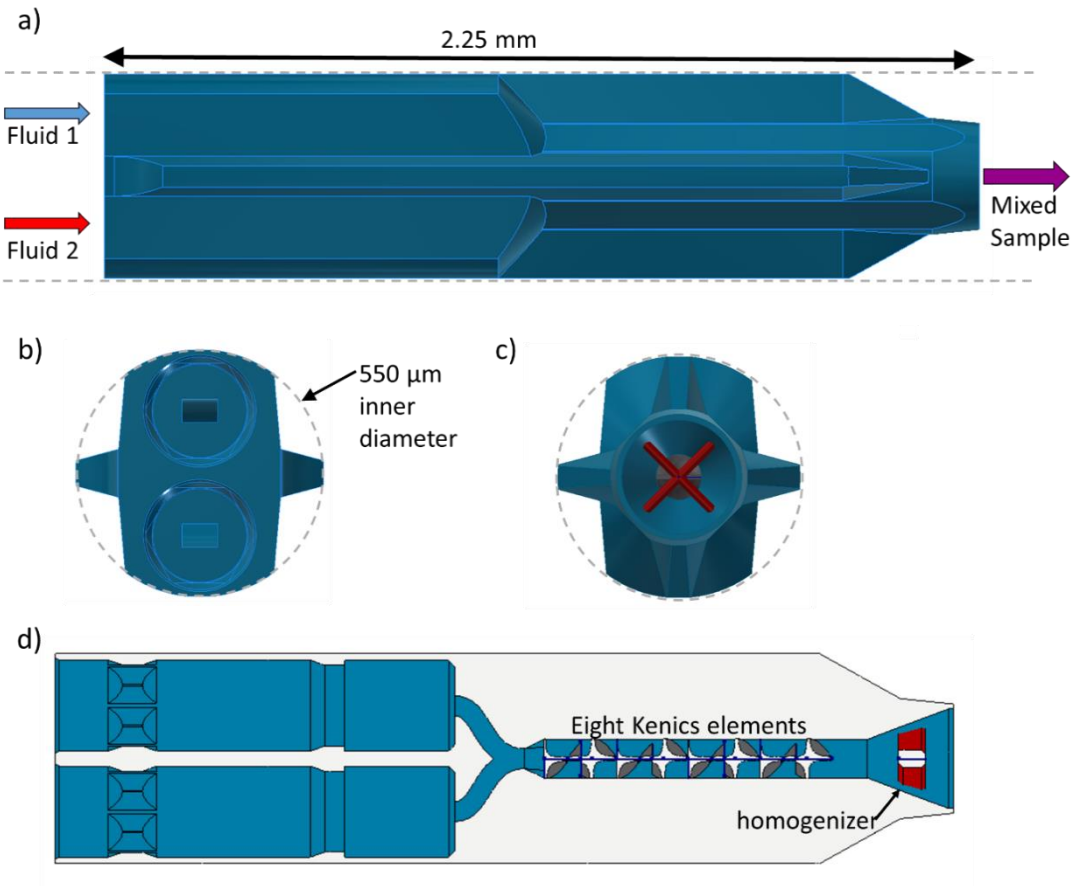

Figure 38. Structural insert design. a) CAD view of the exterior of the device. The observation capillary is shown in dashed gray lines. Arrows indicate flow directions into and out of the device. b) Rear view of the insert, showing the supply line ports. The observation capillary is shown as a dashed gray line. The design of the insert allows the sheath liquid to flow around it. c) View of the insert from downstream. The red, cross shaped element is a flow homogenizer located in the device's outlet. d) Cross-sectional view of the entire insert. The Kenics mixing elements and flow homogenizer are shown in gray and red for visual distinction, but are in reality one piece with the rest of the insert.

5.2.3 Kenics static mixing elements design

At the heart of the mixing insert are the helical mixing elements adopted from the Kenics static mixer. Each helical element produces a baker's transform as the fluids traverse it, stretching, splitting, and stacking the flows to double the number of interfaces and reduce the largest cross-sectional dimension of each of the "strips" of fluid. The more elements present, the smaller these strips become, and the more rapidly a large molecule such as a protein can diffuse across the interface. If the sample

contains typical proteins (diffusion coefficient ~10^{11} m^2/s [80]) in a solution with viscosity similar to or slightly greater than water, and the desired mixing time is <10 ms, there must be enough helical elements to reduce the dimension of the sample "strips" to ~200 nm. In this insert with its ~100 μm diameter mixing channel, this level of mixing is accomplished after eight helical elements. The insert was designed with a channel long enough to incorporate nine elements, to provide an extra factor of safety or to ensure full mixing of more viscous solutions. For the experiments described below, only eight elements were deemed necessary, and the remaining portion of the channel was left empty to provide time for the flow profile to develop before the solution leaves the insert.

To optimize the helical elements, ANSYS Fluent 18.2 (ANSYS, Inc., Canonsburg, Pennsylvania) was used to simulate the baker's transform from helical elements with varying dimensions. There are previous, in depth studies on the optimization of Kenics mixers [88], [90] that guided the selection of parameters to test in these simulations. Mixers were simulated with twist angles of 135º, 158º, and 180º (canonical to Kenics mixers) and aspect ratios of 1.125, 1.3, and 1.5 (the usual Kenics aspect ratio). The simulations also took into account fluids with different viscosities. Helical elements with a twist angle of 135º were found to mix most efficiently per linear distance, in agreement with previous simulations in the literature [88]. According to the literature, this twist angle also has the advantage of reducing the timing dispersion for sample traveling through the mixing elements relative to the canonical 180º twist angle [88]. Our simulations showed the baker's transform to be very robust with respect to both aspect ratio of the blades and viscosity of the fluid. Therefore, the shortest aspect ratio was chosen to allow the elements to fit into the shortest linear space possible and minimize the dead volume of the insert.

Figure 39 shows a cross-sectional view of the Kenics channel at various points throughout the first five helical elements. While the flow through all eight elements was not simulated due to computing constraints, the simulations show the expected behavior: there are about 2^n interfaces after n blades, and the "strip" pattern agrees with simulations in the literature [88].

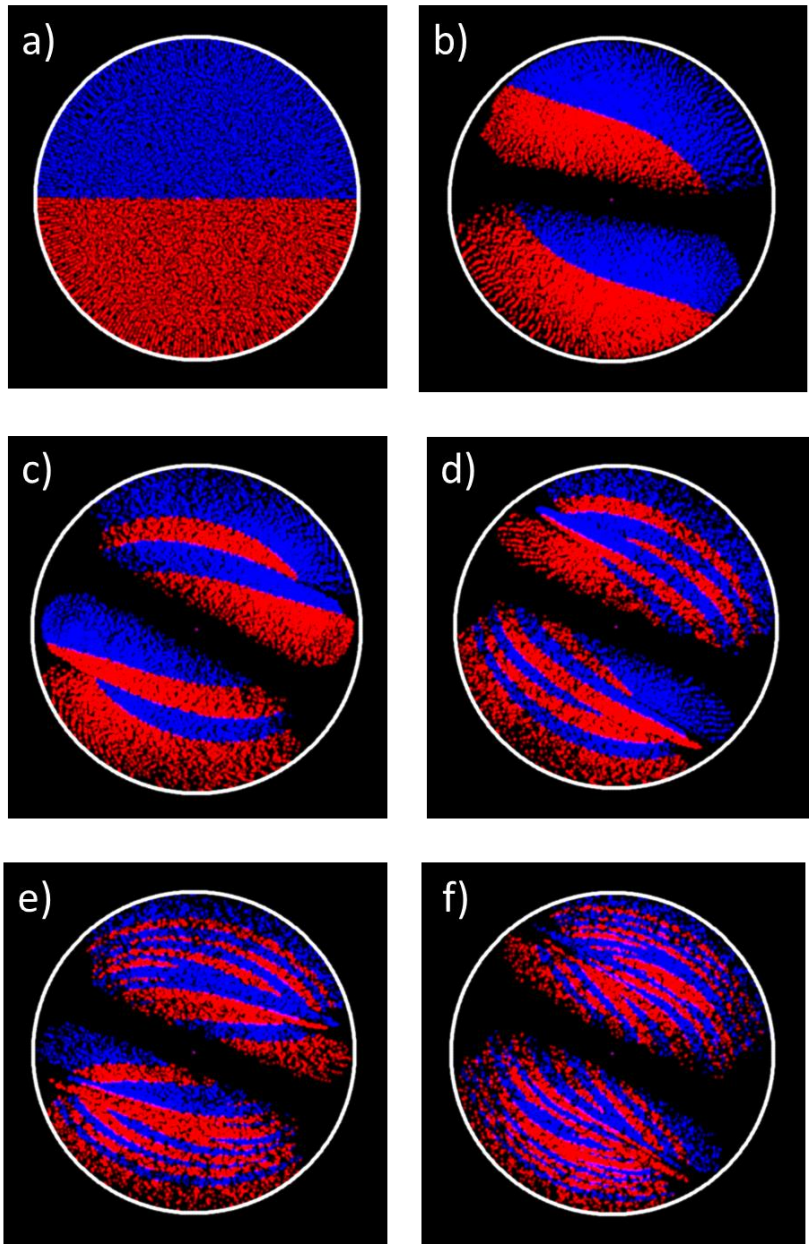

Figure 39. Cross sectional view of the simulated flows at different locations inside a Kenics mixer with twist angle of 135º and aspect ratio of 1.125. Locations are as follows: a) immediately before the flows encounter the first element, b) after one helical element, c) after two elements, d) after three elements, e) after four elements, f) after five elements. These images have been smoothed to increase the apparent size of the streamlines to make them easier to see. This may reduce or eliminate the visibility of thinner striations in the later panels.

5.2.4 Supply line attachment

Mixing inserts were shipped from Germany in their developer solution, PGMEA. Upon arrival, the inserts were briefly transferred to isopropyl alcohol to remove the developer, and then set on a clean watch glass to dry. The inserts must not remain in the isopropyl alcohol for more than a few minutes or they will swell, preventing insertion into the observation capillary.

A schematic of the setup used to facilitate the attachment of the supply lines to the insert is shown in Figure 40 a). Dry inserts were slipped into a 550 µm inner diameter glass tube (1-000-0100, Drummond Scientific Company, Broomall, PA) with a stop inside, so that the inserts were securely held with the supply line ports sticking out of the glass tube. Two, ~24" long capillary tubes with 100 µm inner diameter and 200 µm outer diameter (TSP100200, Polymicro Technologies, Phoenix, AZ) were taped into two vee groves cut into an aluminum block the same distance apart as the supply ports on the insert. This ensured that the capillaries were mounted parallel to each other, and were spaced correctly to enter the insert's ports. The glass tube holding the insert was secured to a mount that allowed coaxial rotation of the tube to position the ports in the correct orientation relative to the capillaries, and the aluminum block was mounted on a three-axis translation stage. The translation stage was used to position the supply lines and drive them forward so that they slid into the ports on the insert. Figure 40 b) shows a picture of the insert and capillaries during alignment.

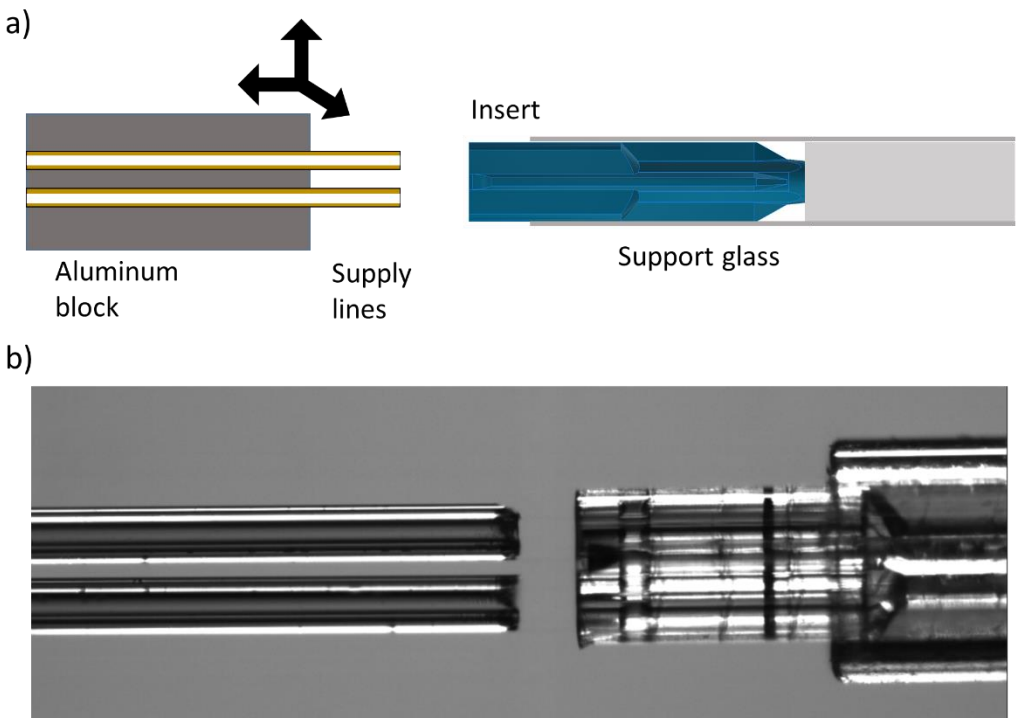

Figure 40. Aligning the supply lines with the insert. a) Schematic of the supply line attachment setup. The 3-axis translation stage allowed the supply lines to be maneuvered so that they slid into the ports on the insert. b) Picture of supply lines that have been aligned to the ports and are ready for insertion into the insert.

After inserting the supply lines into the mixing insert, UV curable epoxy (UV18S, Master Bond, Hackensack, NJ) was wicked into the ports around the supply lines using a piece of glass drawn to a ~100 µm tip as an applicator. Care was taken to avoid getting epoxy on the outside of the insert or creating a large blob of cured epoxy upstream of the insert that would interfere with the passage of the sheath flow around it. When the epoxy reached the second constriction in the supply ports, it was rapidly cured with light from a 365 nm LED (LZ1-30UV00-0000, LED Engin Inc., Marblehead, MA) from both sides to permanently secure the supply lines to the insert. The double-sided cure is important because the insert and capillaries absorb significant amounts of UV light, and epoxy in their shadows will not be cured. Curing simultaneously from both sides eliminates this problem. Figure 41 shows a mixing insert with the supply lines glued in.

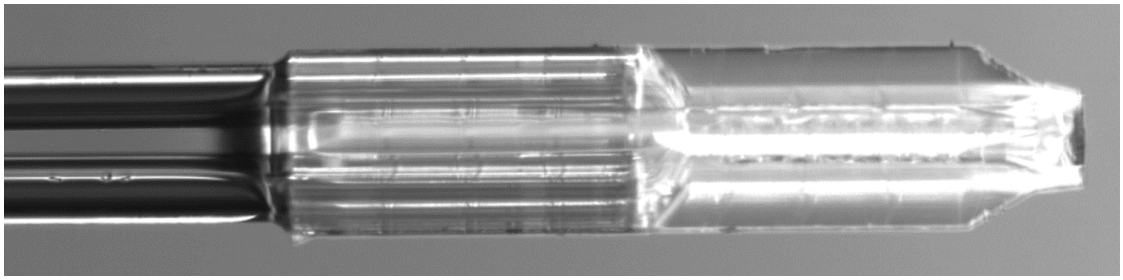

Figure 41. Mixing insert with supply lines glued into the ports.

After the supply lines were glued into the insert, a 20 mm long piece of 550 µm ID, 794 µm OD glass tubing (1-000-0100, Drummond Scientific) was slipped over the upstream ends of the supply lines and positioned so that its closest end was 25 mm upstream of the mixing insert. Low viscosity UV curable epoxy (UV15, Master Bond) was wicked all the way down the glass tube, then cured to create a solid plug inside. This allows a seal to be created around both supply lines with a single microfluidic fitting in the mounting scheme discussed below.

5.2.5 Mixer assembly

A schematic of the assembled mixer is shown in Figure 42 a). While the principle of the mounting apparatus is similar to that described in Chapter 4 (an observation capillary is suspended between a microfluidic tee and microfluidic union, which are used to connect the mixer to the supply and waste lines), the design was improved to make it more robust. Figure 42 b) shows a CAD rendering of the assembled device. Microfluidic tees and unions were manufactured from rectangular pieces of inert PEEK plastic, then secured to specially fabricated brass dovetail carriages that travel over an aluminum support rail. The different metals were chosen to avoid galling and to allow the carriages to slide smoothly without lubrication. The dovetail framework keeps the axes of the microfluidic tee and union parallel to each other, increasing the ease of mixer assembly and alignment in the X-ray beam.

To assemble the device, two short pieces of 1/32” OD, thin wall stainless steel tubing (89935K76, McMaster-Carr, Princeton, NJ) were secured into the downstream end of the PEEK

microfluidic tee and the upstream end of the union with standard 6-32 coned fittings (F-126, IDEX Health and Science, Oak Harbor, Washington). Then, a 2” long piece of 550 µm ID, 610 µm OD borosilicate glass (Code # 1472544, Hilgenberg GmbH, Malsfeld, Germany) to serve as the observation capillary was suspended between the steel tubes, with one end of the glass inside each of the pieces of steel tubing, and glued in place with five-minute epoxy. (Glass was used instead of the polyimide observation capillaries described in Chapter 4 to produce less low q background scatter.)

Once the observation capillary was glued in place, the insert assembly was threaded through the PEEK tee and into the observation capillary, then secured in place with another 6-32 fitting over the epoxy-filled glass tube to create a seal over both supply lines. A sheath supply tube and waste line were attached to the remaining microfluidic ports to finish the mixer assembly. Figure 42 c) shows a picture of a real, completed mixer.

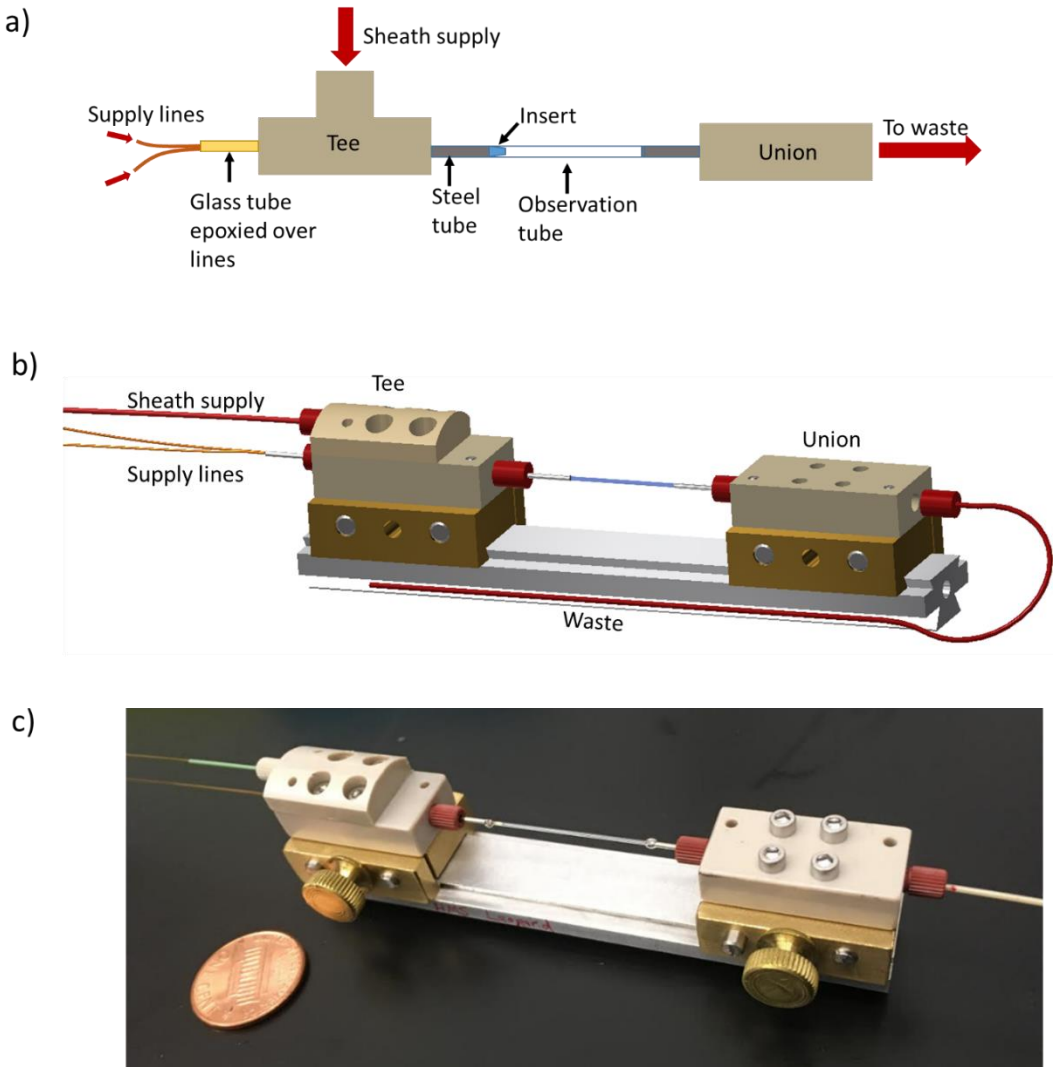

Figure 42. Assembled mixer. a) Schematic showing the assembly principle. b) CAD rendering of the completed device. c) Photo of a real mixer, with penny for scale. See http://hdl.handle.net/1813/57588 for more detailed drawings.

5.2.6 In-lab characterization

Finished mixing devices were characterized in advance of the beamtime using a custom built, long working distance fluorescence microscope, described in Ref [76]. To visualize the flow through the mixer, a solution of 20 µM fluorescent rhodamine 6G dye (R4127, Millipore Sigma, Burlington, MA) was pumped through one of the mixer supply lines, while water was pumped through the other. Water was also used as the sheath flow. A green LED (XPE2, Cree, Inc., Durham, NC) excited the

fluorescence in the device. Images were collected with a CMOS camera (Zyla 5.5, Andor Technology, Belfast, UK) and 10x Mitutoyo infinity corrected long working distance objective (#46-144, Edmund Optics, Barrington, NJ).

Figure 43 shows fluorescent dye leaving the mixing insert, which also fluoresces in the green light. The flow is well centered in the observation capillary and remains so for a distance of over 25 mm beyond the insert. This test was repeated with sample solutions containing 45% sucrose to test the flow characteristics for viscous samples (the sheath remained pure water). No disruption in flow centering was observed.

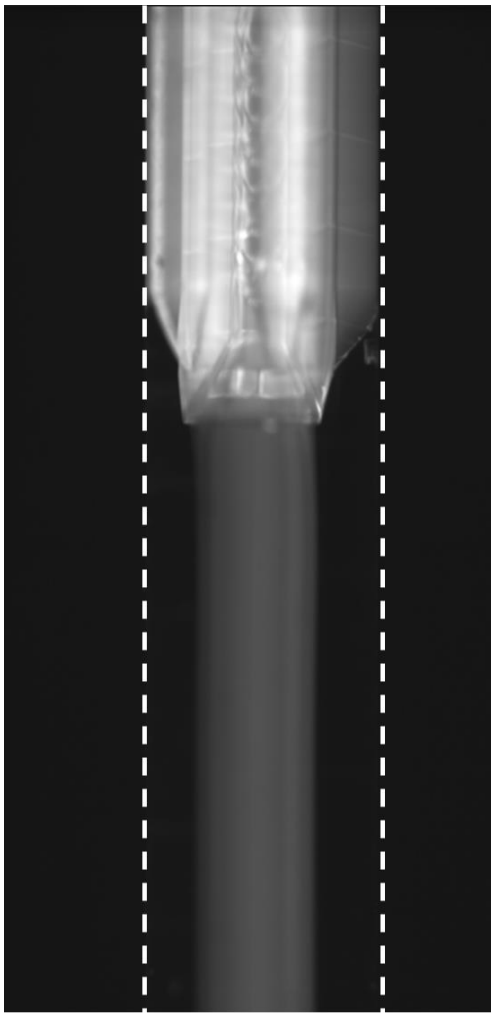

Figure 43. Fluorescence image of dye leaving the insert in a fully assembled device. Flow direction is from top to bottom. The observation capillary is drawn in dashed white lines to help guide the eye.

To characterize mixing within the device, we flowed 20 μM rhodamine through one mixer supply line and 300 mM potassium iodide through the second supply line. Iodide decreases the fluorescence from the dye by providing an alternate, non-radiative pathway for the excited fluorophores [74], [95]. Figure 44 shows a comparison of fluorescence in the mixed flow for the cases when mixing rhodamine and water, and rhodamine and iodide. The fluorescence is much reduced in the case of mixing dye and iodide, and is relatively constant from the point the mixed sample leaves the insert, demonstrating that full mixing occurs inside. The experiment was repeated in 45% sucrose solutions. While iodide quenching is much reduced in sucrose, the observed, smaller changes in

fluorescence agreed with static measurements of water/dye and iodide/dye mixtures in a fluorescence spectrophotometer, giving confidence that the device mixes well even for viscous solutions.

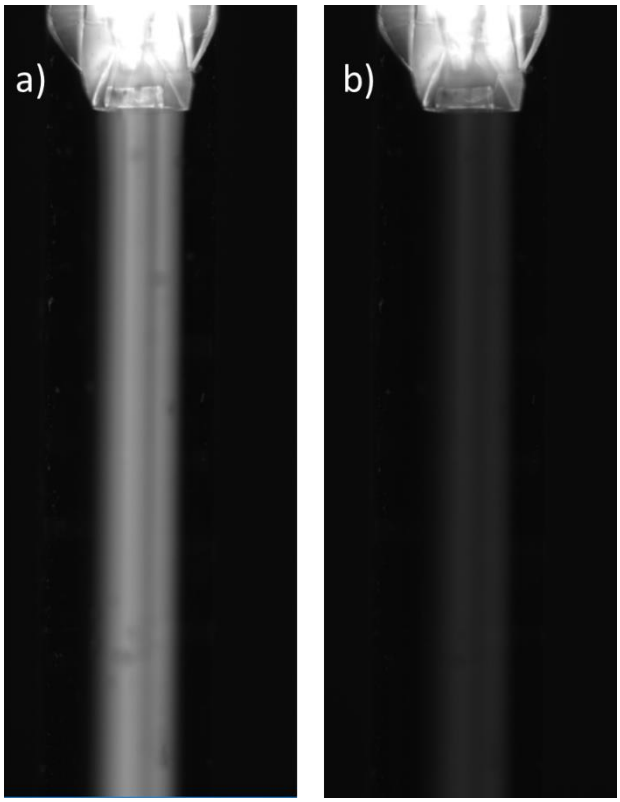

Figure 44. Fluorescence quenching characterization. a) Mixing dye and water. b) Mixing dye and iodide. These images were taken using a preliminary version of the insert with slight differences to the outer shape and flow homogenizing elements that do not affect the mixing.

5.3 Beamline configuration

5.3.1 Custom "scatterless" slits for beam size optimization

Time-resolved chaotic advection mixing experiments were carried out at Station G1 at CHESS, using a setup that built upon the successful elements from the diffusive mixing experiments. Previously, the combination of a commercial "scatterless" tantalum pinhole and homemade germanium guard slit blade described in Chapter 4 produced the small, stable X-ray beam necessary for time-resolved SAXS experiments with low timing dispersion and low background scatter.

The same setup could be used with the chaotic advection mixer. However, one of the apparent drawbacks of the new mixer provides an unexpected opportunity for improvement. The chaotic advection mixer requires ~10 times higher sample flow rates than the diffusive mixer. This makes it possible to use a larger X-ray beam without introducing significant timing dispersion. The bigger beam greatly increases the X-ray flux and reduces the data acquisition time, which minimizes the total amount of sample used and partially compensates for the higher flow rates. This increased X-ray flux (and subsequent sample savings) is especially important for systems solvated in buffers with lower X-ray contrast, such as the sucrose solutions used for time-resolved contrast variation SAXS. Therefore, to utilize the full potential of the chaotic advection mixer, it is important to produce a larger beam than was used previously. The requirements for this beam are strict: if the experiment is to yield high signal-to-noise time-resolved SAXS data with reliable background subtraction, the larger beam must maintain the high stability and low background scattering characteristics observed in the setup described in Chapter 4.

For these mixers, the ideal beam size is ~120 μm wide in the flow direction and ~150 μm wide in the perpendicular direction, representing a good compromise between high X-ray signal and low timing dispersion. A rectangular beam this size contains about nine times more flux than the 50 μm circular beam generated by the scatterless tantalum pinhole (about 10^{12} ph/s with the larger beam) and would reduce the acquisition time, and therefore sample consumption, by the same factor.

Following the success of the homemade germanium guard slit blade described in Chapter 4, a full set of germanium slits was fabricated in-house and used as the beam defining aperture. A dovetail slit mount (design concept by George Calvey) was machined to hold the slits and adjust their separations. Figure 45 shows the design of the slit mount. The mount is composed of an aluminum square, shown in Figure 45 a), in which four dovetail grooves are milled in the shape of a cross, with a through-hole for the beam in the middle. One brass dovetail carriage travels in each slot. The differing metallic natures of the carriages and mount allow the carriages to slide smoothly without galling. Each

brass carriage is topped by a small aluminum piece whose purpose is to hold the slit. There are two styles of these slit-holder pieces. One is taller than the other to prevent the first set of slit-blades from hitting the second at small slit gaps. Each type of carriage assembly is shown in Figure 45 b). The two tall carriages are placed opposite each other in the slit mount.

To make the slit blades, 5 mm x 5 mm squares of 500 μm thick germanium (100) (GEUa050505S2, MTI Corporation, Richmond, CA), were polished to a mirror finish on one edge using an Allied Multiprep 8" polishing wheel (Allied High Tech Products, Inc., Los Angeles, CA). Silicon (100) wafers were diced into 5 mm x 5 mm squares in the Cornell NanoScale Science and Technology Facility by Alex Plumridge, and then similarly polished on one edge.

Each aluminum slit-holder part on top of the carriages has a recessed slot milled into its end at a 5 degree angle. A slit-blade is glued into each recess, as shown in Figure 45 c). The straight edge of the recess allows each square slit-blade to be glued perpendicular to the direction of the carriage's travel. The 5 degree slit-blade mounting angle is designed to reduce grazing incidence scatter off of the edges of the slits, as detailed in Ref [28].

To enable fine positioning of the slit, each dovetail carriage is spring-loaded to reduce backlash, and is driven via a fine thread adjustment screw. The slit gaps are adjustable between several microns and 2.5 mm. For this experiment, the slit gaps were set to 115 microns in the vertical dimension and 140 microns in the horizontal dimension. Figure 45 d) shows a CAD cross section of an assembled, adjusted set of slits to illustrate the clearance between the slit blades and the beam direction. Figures 45 e) and f) show a CAD view and an actual photo of the completed mount.

The slit mount is small and light, and can be positioned near the sample cell as the pinhole was previously. The beneficial characteristics of the pinhole are therefore maintained: the beam-defining aperture is close enough to the sample cell to prevent significant beam expansion between the

slits and the sample, and the low intrinsic scatter of the single crystal slits creates a stable beam that is not greatly sensitive to upstream beam motions and has low background scatter.

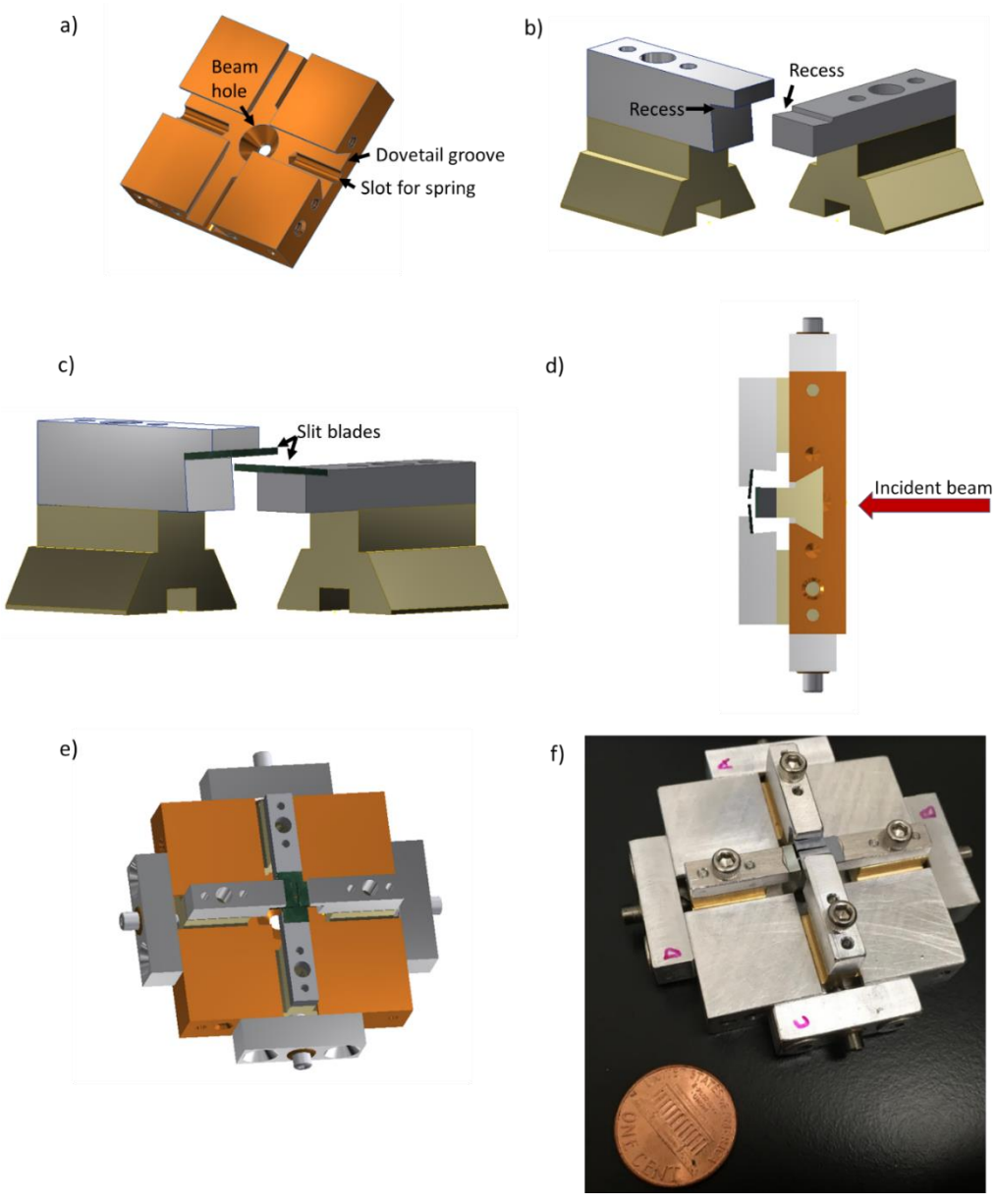

Figure 45. Slit mount design. a) CAD view of the slit mount showing the four dovetail grooves and beam through-hole. Each dovetail groove has a slot at its base to hold the captive spring that loads each of the dovetail carriages. b) CAD view of two dovetail carriages, one with each type of aluminum slit-holding topper. c) Illustration of how the slit-blades are glued to each type of slit-holding topper. b) Sectioned side view of an assembled mount to show the dovetail slots, slit blade clearances, and beam direction. d) Oblique CAD view of a slit mount assembly. e) Corresponding photo. Penny for scale. See http://hdl.handle.net/1813/57588 for details.

To determine the effectiveness of the homemade slits in reducing background scatter, their scatter was compared to that from the standard tungsten G Line slits. Figure 46 a) shows an image of the scattering produced by a single set of the standard G Line slits adjusted to a gap of 115 μm x 140 μm, and Figure 46 b) shows an image of the scattering from one set of homemade germanium slits adjusted to the same size. The germanium slits produce several bright flares, but the overall level of isotropic scattering is lower, resulting in less total low angle background scatter. The germanium does produces excess background fluorescence at the 11.28 keV beam energies used for these experiments. However, both the bright jets and fluorescence were greatly reduced by introducing a second set of homemade guard slits set to a width of 220 μm in the vertical direction and 275 μm in the horizontal direction, as shown by the scattering image in Figure 46 c).

The choice of material for the guard slit blades was a tradeoff between highly attenuating germanium and non-fluorescing silicon. To reduce fluorescence created by the guard slits, only one of the four guard slit blades was fabricated from germanium: the top vertical blade, which shields the majority of the detector from parasitic scatter and benefits the most from high X-ray attenuation. The horizontal and bottom blades were fabricated from silicon, which does not block the flares from the beam defining aperture as well. However, since the detector images mostly collect scatter in the upward direction, the main goal of the other three guard slits is to prevent parasitic scatter from the beam-defining slits from hitting the sides of the sample cell and creating excess background scatter. The silicon is sufficiently attenuating for this purpose. Images were masked to eliminate the horizontal flares and to utilize only the upward scatter, as discussed in Chapter 4. Figure 46 d) shows integrated scattering profiles from all three tested slit conditions. The homemade scatterless slit pair reduces background scattering at all angles.

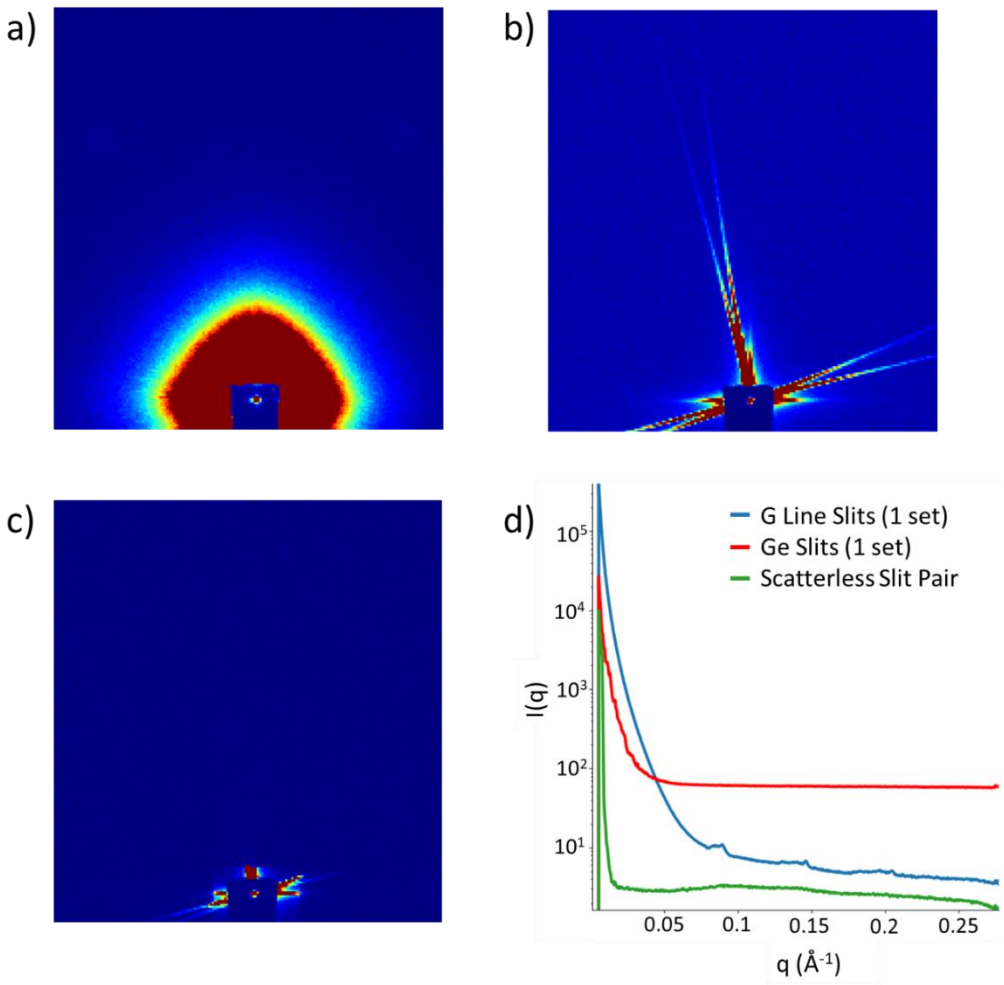

Figure 46. Comparison of scattering from different slit configurations. All images and profiles are normalized by the transmitted beam intensity. a) Image of scattering produced by one set of standard G Line slits. b) Image of scattering produced by one set of homemade Ge slits set to the same size as the standard slits in a). c) Image of scattering produced by the homemade scatterless slit pair. d) Integrated scattering profiles from all three conditions. In all cases, there is no sample cell in the beam, and all measured scattering comes from the slits themselves.

When using the homemade scatterless slit pair, the lowest reliable q value is ~0.01 Å^{-1}. This is an improvement over the previous setup, which was only usable down to 0.02 Å^{-1}. By reducing this minimum reliable q value, the slits allow the study of slightly larger complexes, which is beneficial for a mixer designed to study interactions between two biomolecules.

5.3.2 Beamline hardware

The beamline hardware setup is similar to that described in Chapter 4, with small changes to increase the ease of use and facilitate the positioning of the homemade slit sets. A second 6” x 6” x 6” cubic vacuum chamber (P106861 frame, P106862 blank wall, P106863 KF-40 walls, and P106869 viewing window plate, Ideal Vacuum Products, Albuquerque, New Mexico Ideal Vacuum Products, Albuquerque, NM) was purchased and coupled to the first chamber with an Ideal Vacuum P106870 Multicube Coupling Kit to provide extra space to manipulate the slits and mixer in vacuum. Figure 47 a) and b) show a CAD overview of the modified beamline setup as well as an actual photo.

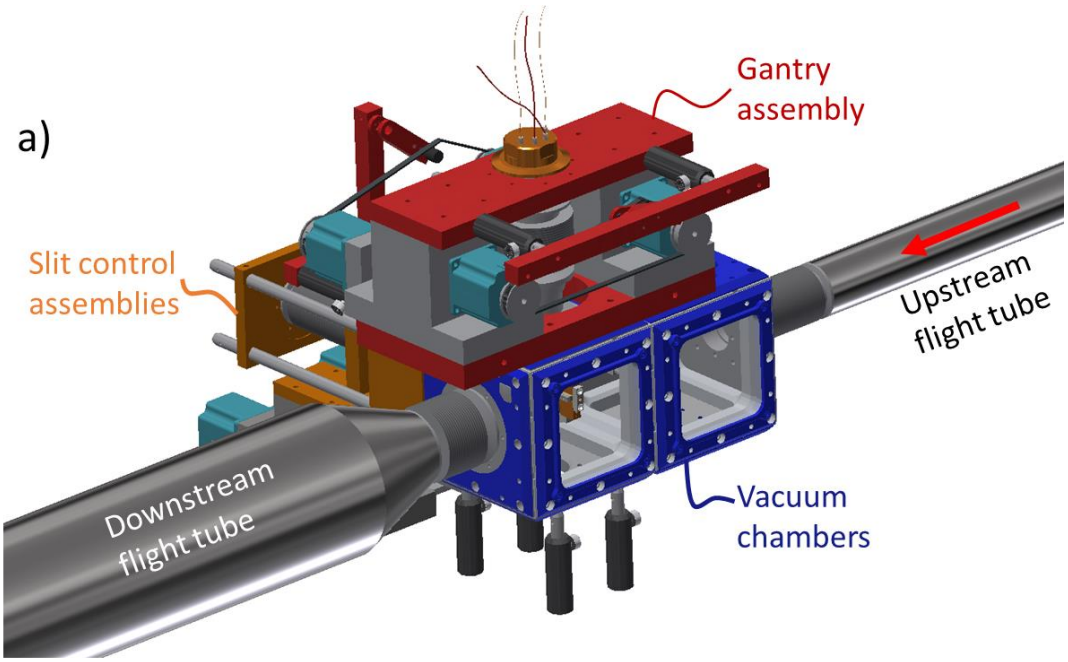

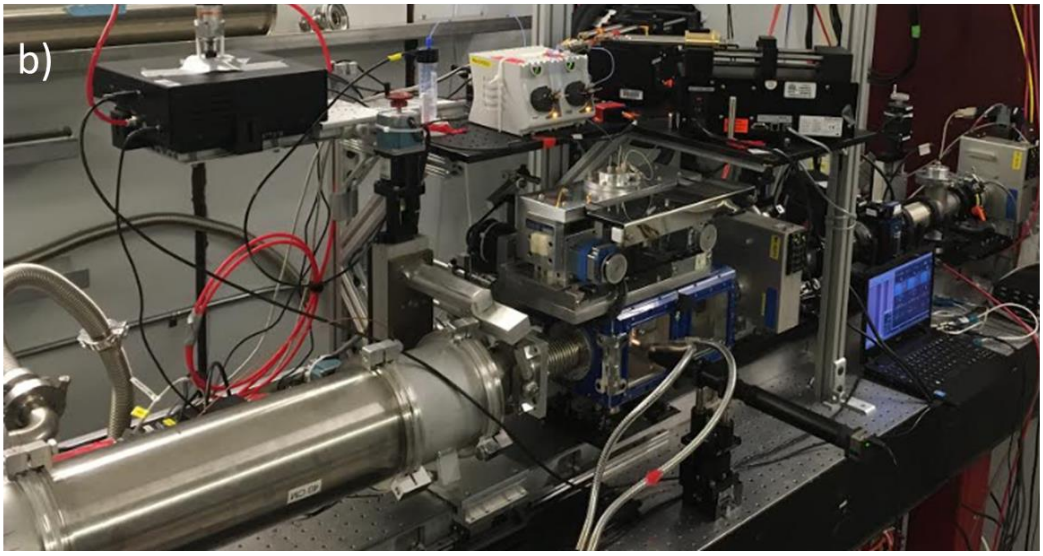

Figure 47. Overview of the beamline setup. a) CAD view with parts color coded by function. Red parts are associated with the gantry. Orange parts are associated with the slit control system. The vacuum cubes are shown in blue. b) Photo of the setup during beamtime. See http://hdl.handle.net/1813/57588 for detailed drawings.

Figure 48 a) shows a detailed picture of the locations of the slit sets and mixer inside the cubic vacuum chamber. The upstream chamber holds the beam-defining slits, while the downstream cube holds the guard slits and the mixer. Figure 48 b) shows a picture of the interior of the downstream

chamber. The mixer is controlled by the same gantry setup as used previously, with the dovetail mixer mount rigidly connected to the gantry via an optics post. Figure 48 c) details the mixer attachment to the gantry. The slit mounts are each positioned via the mechanism discussed for the guard slit-blade in Chapter 4.

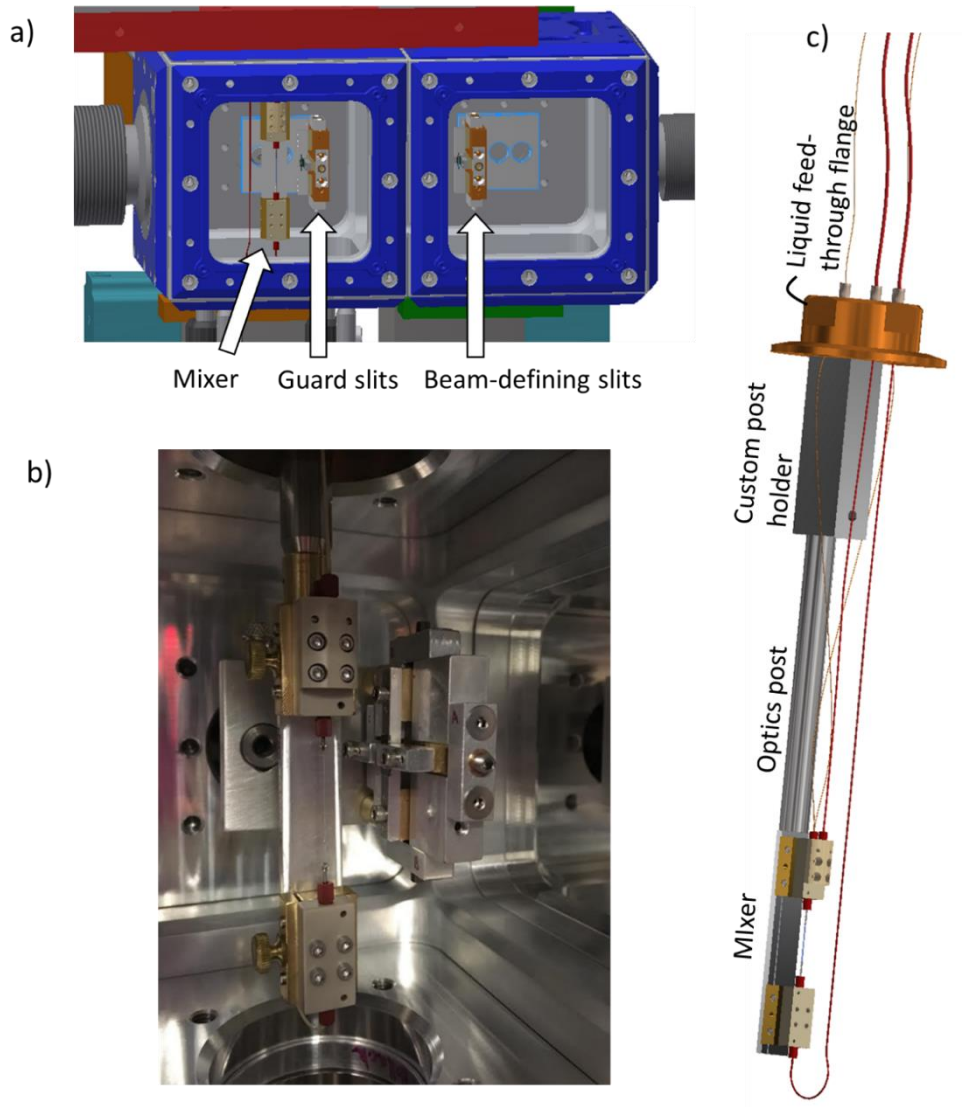

Figure 48. Detail of the inside of the sample chambers. a) CAD view showing location of the slits and mixer. b) Photo of the downstream chamber showing the mixer and guard slits. c) CAD illustration of the attachment of the mixer to the gantry. See http://hdl.handle.net/1813/57588 for more detailed drawings.

To configure the beamline, the hardware alignment proceeded similarly to that described in Chapter 4. The cubic vacuum chambers and gantry system were first positioned so that the beam passed through the center of the chambers and was intercepted by the semi-transparent molybdenum beamstop at the end of the downstream flight tube, with no apertures or mixer present. Then, the beam-defining aperture was placed in the upstream vacuum chamber and scanned into position to maximize the counts measured through the semi-transparent beamstop. Next, the guard slits were inserted and centered horizontally relative to the beam-defining slits. They were positioned vertically to block out the most possible parasitic slit scatter without clipping the main beam.

The mixer was inserted into the chamber and first scanned in horizontally, to find the center of the observation channel, then vertically, to find the bottom of the insert. The mixer was then translated vertically so that the beam passed through the correct portion of the observation capillary to measure the desired delay time (delay times and lengths are detailed below).

5.3.3 Flow control

A schematic of the fluid delivery system is shown in Figure 49. Two high pressure syringe pumps (PHD 4400, Harvard Apparatus, Holliston, MA) and stainless steel high pressure syringes (70-2269 and 70-2267, Harvard Apparatus) were used to drive the flow to the two mixer supply lines. This was necessary due to the high pressures needed to drive solutions 10-15 times the viscosity of water, such as the sucrose solutions used for time-resolved contrast variation experiments, through the small inner diameter mixer supply lines. One pump held the two syringes containing the samples to be mixed; the other held two syringes containing the corresponding buffers. Two high pressure switching valves (MXP7970-000, IDEX Health & Science, Oak Harbor, Washington) were placed immediately downstream of the syringe pumps. Each valve had one inlet connected to one sample syringe, a second inlet connected to its corresponding buffer syringe, and its outlet connected to a mixer supply line. Therefore, by selecting flow from one inlet or the other, the switching valves were used to toggle the

fluid supply to the mixer between buffer and sample to facilitate the acquisition of background images. The valves and pumps were computer controlled (credit: Josue San Emeterio) to ensure that each syringe pump turned on and off depending on the status of the switching valves, preventing overpressurization of the syringes.

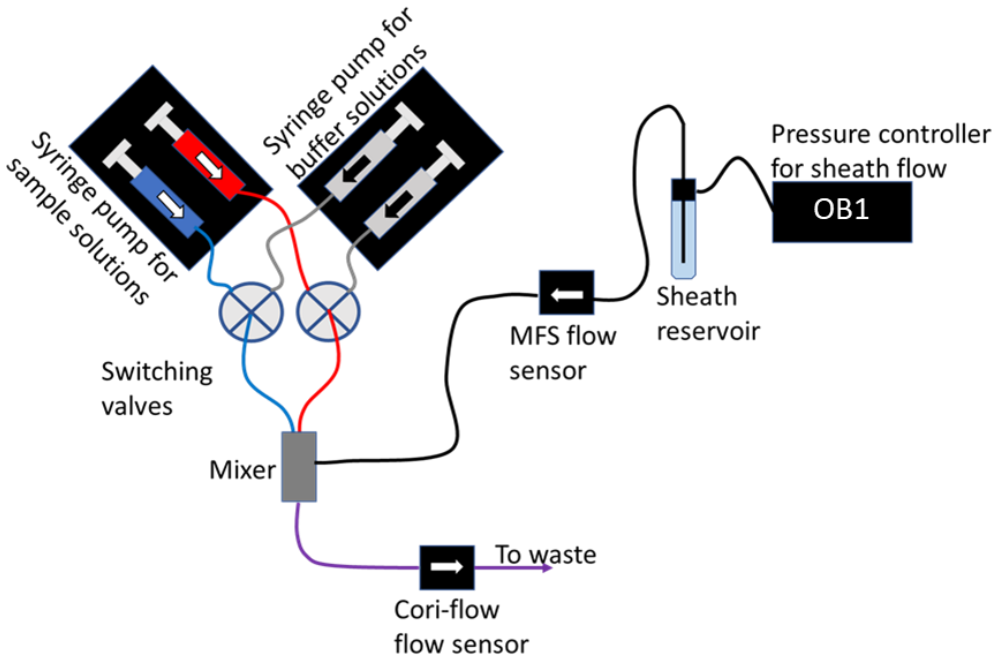

Figure 49. Schematic of the flow path.

The sheath flow was driven by a multichannel pressure controller (OB1, 0-8000 mbarr range, Elveflow, Paris, France), and the sheath flow rate measured with flow sensors (MFS3 or MFS4 depending on flow conditions, Elveflow). The majority of the pressure drop in the sheath flow path occurred between the reservoir and the mixer. This necessitated the use of helium gas to drive the sheath flow. Attempts to use nitrogen produced dissolved gas in the reservoir that came out of solution in the mixer to form large bubbles and disrupt the centered flow there.

The flow through the waste line of the device was monitored by a second sensor that simultaneously measured the total mass flow rate and the solution density, giving a very accurate

reading of the total volumetric flow rate (ML120V00 Mini Cori-flow, Bronkhorst USA Inc, Bethlehem, PA). This flow sensor, in combination with the upstream MFS flow sensor on the sheath supply line, was used to calculate the flow rates from the syringe pump and to ensure that the syringes had reached their final operating pressure before acquiring data. It is important that the downstream Cori-flow flow sensor measures both mass flow and density to report the volumetric flow rate, rather than the simpler thermal diffusivity volumetric flow measurement that the upstream MFS flow sensors do. While the MFS flow sensor provides accurate readings for water, extensive calibrations would be necessary to accurately measure flow rates from with mixed solutions with various thermal diffusivities, depending on the sample constitution. The Cori-flow flow sensor does not require calibrations, greatly simplifying the experiment.

Figures 50 a) and b) show pictures of the device mixing both water-based and sucrose-based solutions inside the vacuum chamber, with flows driven by the system described above.

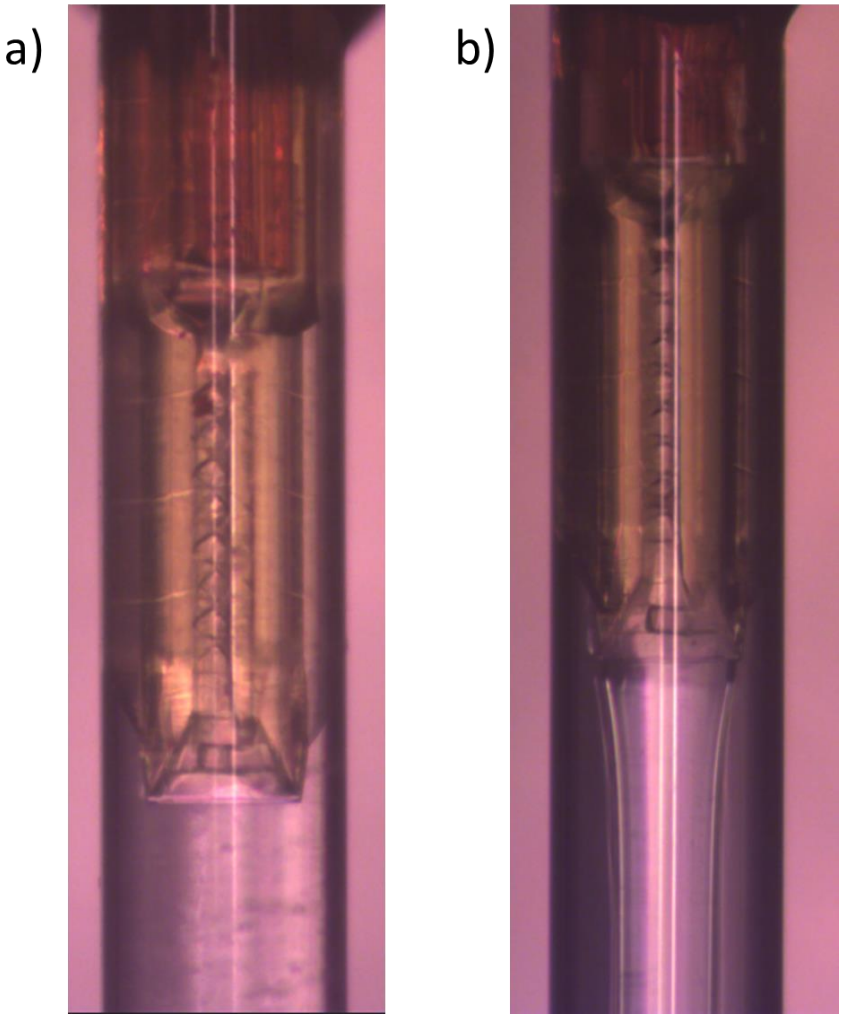

Figure 50. Images of a mixer in the vacuum chamber. The illumination and the angle of the insert in the channel are ideal for viewing the interior helical Kenics elements. a) The device mixing solutions that contain no sucrose. b) The device mixing solutions containing 48% sucrose, with a water sheath. The sucrose flow is visible due to the difference in index of refraction between sucrose and water.

5.4 Overview of time-resolved SAXS with the chaotic advection mixer

As a proof of principle for the device, the chaotic advection mixer was employed examine the binding of trypsin, a protein found in the digestive system of many vertebrates, and its inhibitor aprotinin, also known as BPTI (bovine pancreatic trypsin inhibitor). This system is well studied, with crystal structures known for each constituent protein as well as for the complex, and therefore served as an ideal test system for this mixer.

This experiment was carried out at Station G1 at CHESS, with a beam energy of 11.28 keV and the improved beamline setup described above. A Pilatus 100K detector (Dectris, Baden, Switzerland) was used to collect scattering images.

5.4.1 A note about sheathed flow and reactant concentrations

In the chaotic advection mixing device, the two samples are mixed in a 1:1 ratio, and are completely mixed inside the insert. Once the solution leaves the insert, no further mixing occurs. Large, slowly diffusing protein and nucleic acid molecules stay mostly confined to the center stream as they travel through the device. Therefore, their concentration remains relatively constant in measurements at different delay times. Small reactant molecules such as ions can diffuse out of the sample stream and into the sheath, changing the concentration of these elements at different delay times. If the concentration of a small molecule is critical to the reaction, it should be present in the sheath flow to prevent diffusion, with the added consideration that the upstream MFS flow sensor may need to be re-calibrated. These experiments used a water sheath flow.

5.4.2 Choosing flow parameters for the chaotic advection mixer

When choosing flow parameters for the chaotic advection mixer, we must first consider how to define the delay time in this device. All mixing occurs inside of the insert. However, some of the molecules "see" their binding partners immediately upon entering the insert and can start to react; others may not encounter their binding partners until the last helical element of the insert. Therefore, a sample is considered to be "mixed" (delay time = 0 ms) in half the time it takes for the sample to traverse the insert, with the total time in the insert factored into the uncertainty for each measured delay time. This is most likely a conservative overestimate of the mixing time, since the furthest downstream portion of the insert does not significantly contribute to mixing.

Figure 51 provides a graphical example of how delay time is defined in the device. Consider the case of a desired measurement with 30 ms delay time, and flow parameters such that the sample travels through the insert in 10 ms. In this case the mixing time is considered to be 5 ms, and an uncertainty of ±5 ms is combined with those from beam smearing and flow dispersion when calculating the uncertainty in the measured delay time. 5 ms out of the total 30 ms delay time is then considered to occur inside the insert. The beam should be positioned so that the sample has traveled outside of the insert for 25 ms.

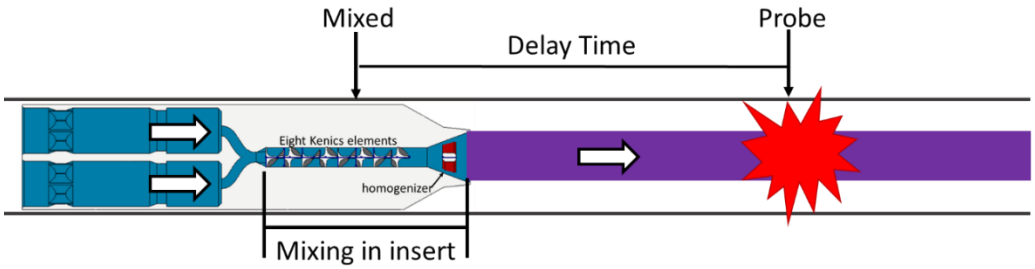

Figure 51. Schematic showing the definition of delay time in the chaotic advection mixer.

A MATLAB script was written by George Calvey to calculate the additional delay time, beam smearing, and flow uncertainty for sample traveling down the observation capillary. The script first divides the sample jet into small (several cubic micron) elements, and calculates the delay times for each individual element, taking into account flow dispersion. Then, the delay times for all elements of the sample that would intersect a 120 µm x 150 µm X-ray beam centered at a given probe distance were averaged to give the overall delay time for that probe position. The standard deviation in the delay times for all of these elements provides a measurement of uncertainty that accounts for both beam smearing and the flow dispersion. To calculate the total uncertainty for each delay time, this standard deviation is added in quadrature with the mixing time uncertainty described above.

Four different flow conditions were employed to measure timepoints ranging from 10 ms to 2 s. Several delay times can be measured at more than one flow condition; the choice of flow condition

is often a compromise between lower uncertainty (higher sample flow rates) and less sample consumed (lower flow rates). For each sample flow condition, the sheath flow rate was calculated so that it would keep the sample jet width constant at a 250 μm X-ray pathlength. Table 2 provides a summary of the delay times and uncertainties attainable with each flow condition, as well as the beam position relative to the end of the insert. Delay times presented in the table are evenly spaced on a logarithmic scale to make it easier to plot quantities such as R_g across a range of delay times. The delay times measured in the experiments are color coded according to the system probed.

Table 2. Summary of flow rates, uncertainties, and beam distance for various delay times at each of the four flow ranges. Uncertainties should be read as ± values. For example, the shortest delay time for the high flow range is 10 ± 3 ms. Delay times highlighted in blue were probed during the experiment.

High Flow (5 ms mixing time)

Sample 1: 60 µL/min Sample 2: 60 µL/min Sheath: 204 µL/min

Delay Time (ms)	*Uncertainty (ms)*	*Beam distance (µm)*
10	3	306
12.5	3	408
16	3	551
20	3	715
25	3	920
32	3	1205

Mid Flow (10 ms mixing time)

Sample 1: 30 µL/min Sample 2: 30 µL/min Sheath: 102 µL/min

Delay Time (ms)	*Uncertainty (ms)*	*Beam distance (µm)*
32	6	544
40	6	711
50	6	922
63	6	1187
79	7	1521
100	8	1941

Table 2, continued

Low Flow (15 ms mixing time)

Sample 1: 20 µL/min Sample 2: 20 µL/min Sheath: 68 µL/min

Delay Time (ms)	*Uncertainty (ms)*	*Beam distance (µm)*
50	8	581
63	9	758
79	9	980
100	10	1260
126	11	1613
158	12	2056
200	14	2616
251	17	3319
316	21	4205
398	24	5316

Snail Flow (30 ms mixing time)

Sample 1: 10 µL/min Sample 2: 10 µL/min Sheath: 34 µL/min

Delay Time (ms)	*Uncertainty (ms)*	*Beam distance (µm)*
398	29	2609
501	34	3311
631	42	4194
794	52	5308
1000	64	6709
1259	80	8472
1585	100	10692
2000	126	13487

5.4.3 Sample consumption and data acquisition times

Due to the greatly increased X-ray flux (larger beam size) and longer sample pathlength of this mixer, high signal-to-noise time-resolved data could be obtained in 100 seconds of data acquisition per sample scan. This allowed the measurement of many more delay times than was feasible with the diffusive mixer. For example, for the trypsin + aprotinin system, eleven distinct time points were measured, with one of these measured three separate times for repeatability assessment. The entire data series took about three hours to complete. Additionally, even though this series probed three delay times at high flow conditions, only about 1.2 mL of sample was consumed. An average of ~0.4 mg of trypsin and ~0.2 mg of aprotinin were consumed per delay time, which is an order of magnitude less sample than needed for "sample-saving" turbulent mixers [52]. In a second experiment not detailed here, which did not use any high flow conditions, nine delay times (and one repeat) were measured using only 700 total µL of each sample! The sample consumption per delay time, ~70 µL, is only about twice the volume required for a static sample in a standard SAXS setup. The entire dataset was collected in under two hours. This improves greatly on the throughput of the previous time-resolved setup, where most of a day was required to measure fewer than ten timepoints.

5.4.4 Assessment of mixer repeatability

The repeatability of the chaotic advection mixer was assessed with the same two tests used for the diffusive mixer. In the first test, the delay time of interest was probed, then the mixer was re-positioned, and a different delay time measured. Then, the mixer was returned to its original location so that the first delay time could be probed again. This test was repeated several times throughout the beamtime, using two different systems of interest. In the most stringent of these tests, not only was the mixer translated back and forth to measure other delay times, but the flow conditions were changed from low flow to snail flow and back before taking the second trial measurement. This test was yielded the repeatable profiles shown in Figure 52 a). The second test is to compare scattering profiles obtained

from the same delay time at different flow conditions. These profiles also agreed well and are shown in Figure 52 b).

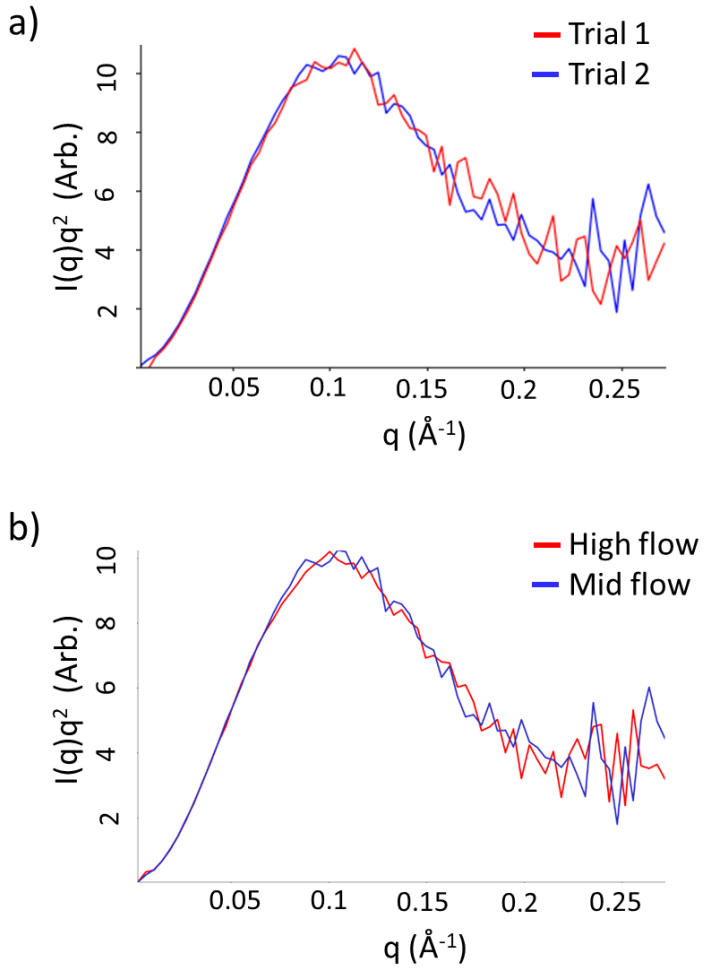

Figure 52. Repeatability assessment. a) Two scattering profiles from the same delay time, in this case, 32 ms at the mid flow condition, taken in two trials. b) Scattering profiles from the 32 ms delay time at both high and mid flow conditions.

5.4.5 Measurement of static endpoints

In addition to the time-resolved data, the starting and ending states of each reaction were assessed using a modified device to acquire static, sheathed flow SAXS data. The modified device had no mixing insert and only one supply line, a 75 µm inner diameter capillary that was held centered in

the observation capillary with the polyimide centering spacers discussed in Chapter 4. Sample or buffer solution was pumped through this supply line using the Harvard syringe pumps and one switching valve was used select between the sample and buffer. Water served as a sheath flow. For these static experiments, the sample and sheath flow rates were both ~5 μL/min and ~7 μL/min, respectively.

5.5 Time-resolved SAXS of the trypsin + aprotinin system

The trypsin + aprotinin system has been well studied in crystallography, and crystal structures of each individual molecule and the complex are known [96], as shown in Figure 53. The molecules are commercially available and easy to prepare, and while trypsin does autolyze, this behavior can be greatly slowed by preparing the solution in a buffer containing calcium [97]. In this buffer, autolysis did not significantly change the trypsin concentration during the few hours necessary to collect the time-resolved SAXS data.

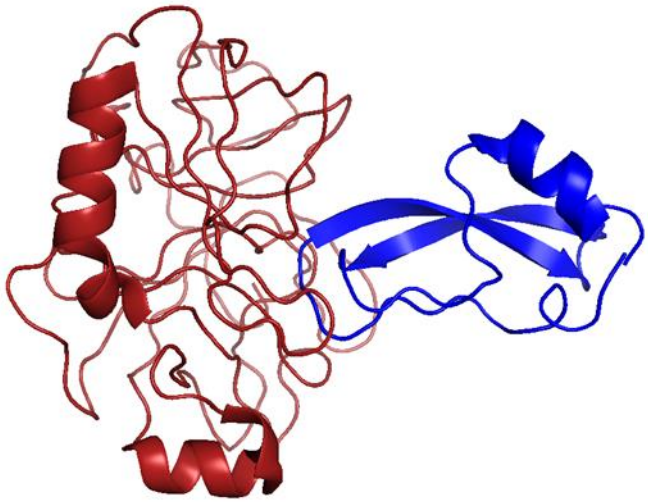

Figure 53. Crystal structure of the trypsin (red) + aprotinin (blue) complex, from PDB 2ptc. This crystal structure is from Ref [96], and was downloaded from the Protein Data Bank [3] and visualized with PYMOL [98].

A trypsin concentration of 4 mg/mL was chosen for these experiments as a compromise between signal strength and avoiding interparticle interference effects. Aprotinin was prepared at a concentration of 1.73 mg/mL, which is 30% greater than the ratio recommended in a previous X-ray and neutron study of the complex [99]. This higher concentration was chosen to increase the rate of complex formation and was picked as the highest allowable aprotinin concentration for which aggregation was not observed in the static SAXS data.

Figure 54 shows a comparison of CRYSOL curves generated from the crystal structures in Ref [96] with the static SAXS data from this beamtime. The shapes of the curves agree well, giving confidence in the profiles of the initial and final states of the reaction. All plots were produced using BioXTAS RAW [100]. The axis labels were subsequently enlarged for clarity.

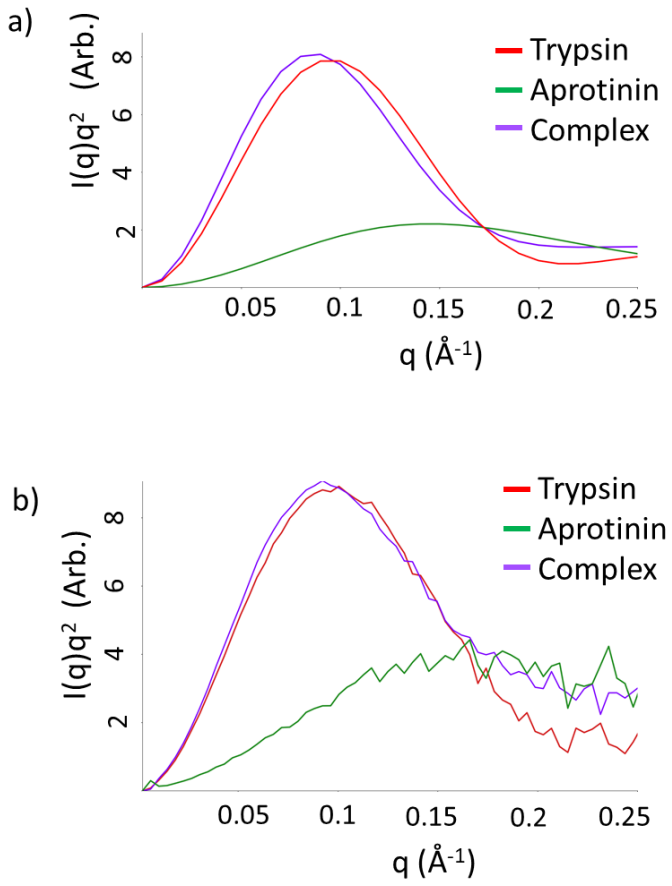

Figure 54. Comparison of computed scattering profiles from crystal structures with static SAXS data. a) CRYSOL curves generated from PDBs 1PT0 (trypsin), 4PTI (aprotinin) and 2PTC (complex). These crystal structures are from Ref [96] and were downloaded from the Protein Data Bank [3]. b) Static SAXS profiles measured in the modified setup described above.

Time-resolved measurements were acquired for the following delay times: High flow = 10 ms, 16 ms and 32 ms. Mid flow = 32 ms and 100 ms. Low flow = 50 ms, 158 ms and 251 ms. Snail flow = 398 ms, 631 ms, 1s and 2 s. Figure 55 shows an overview of the time-resolved data, together with the static endpoints. The initial state shown here is the sum of static scattering profiles from trypsin alone and aprotinin alone. This summed curve approximates the scattering profile in the case that both species are present but unbound. Only seven delay times are plotted for ease of visualization, however, scattering profiles for all delay times trend monotonically from the initial to final states. Figure 56 further highlights the scattering profiles at each of these seven delay times to increase the ease of

following the trends. The earliest delay time measured, 10 ms, is very similar to the initial state but already displays small changes. At a delay time of 2 s, the final complex has formed, and the profile matches the static data.

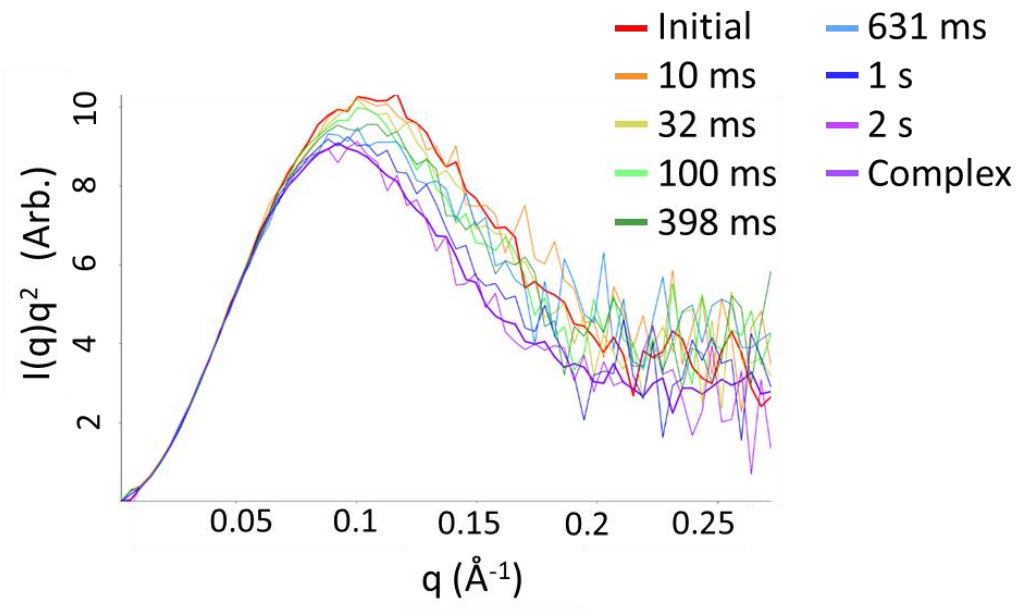

Figure 55. Summary of time resolved data on the trypsin + aprotinin system, with the initial and final static profiles included for reference. The Kratky plots are scaled to match at low *q* to guide the eye to the changing progression.

Figure 56. Detailed view of time-resolved scattering profiles. a) Initial and final states, from static data, are plotted in red and purple, respectively. The time-resolved scattering profiles are plotted in light gray. b)-h) In the subsequent panels, one time-resolved profile is highlighted in green. The other profiles remain grayed out to help with the visualization of the location of each delay time in the progression. The following profiles are highlighted: b) 10 ms, c) 32 ms, d) 100 ms, e) 398 ms, f) 631 ms, g) 1 s, h) 2 s.

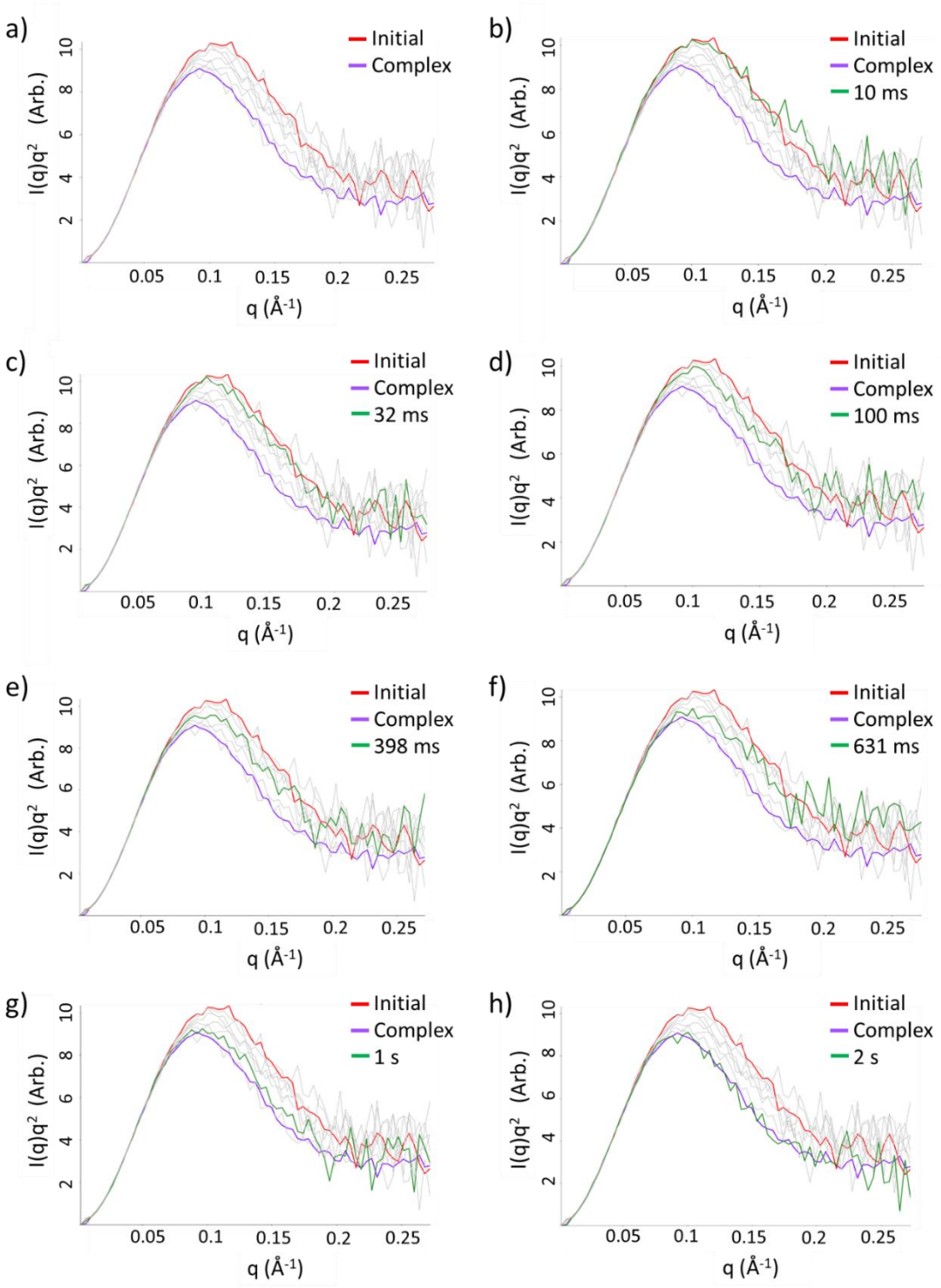
a)
Initial
Complex
b)
Initial
Complex
10 ms
c)
Initial
Complex
32 ms
d)
Initial
Complex
100 ms
e)
Initial
Complex
398 ms
f)
Initial
Complex
631 ms
g)
Initial
Complex
1 s
h)
Initial
Complex
2 s
I(q)q² (Arb.)
q (Å⁻¹)
0.05
0.1
0.15
0.2
0.25
2
4
6
8
10

Analysis of the time-resolved data is ongoing. Future analysis with singular value decomposition techniques will attempt to extract the binding rate from this SAXS data.

5.7 Successes and future improvements

The chaotic advection mixer described in this chapter is a great advancement in high signal-to-noise, low sample volume mixing for SAXS studies of biomolecule association and reactions in viscous solutions. The sample volume consumed is an order of magnitude less than the most efficient turbulent SAXS mixer [52]. In the mid-to-low flow conditions, each delay time consumes only a little more than twice the necessary sample volume for standard static SAXS measurements. Additionally, the ability to use a larger beam allows faster data acquisition. It is possible to take several datasets with multiple delay times in a short amount of beamtime. This device is immediately applicable to many interesting binding systems.

In the future, a specialized “long delay time” mixer with a longer sample path length will be used. This will reduce the diffusion of reactants into the sheath, keeping their concentrations more uniform at all delay times.

Additionally, a planned upgrade to the beamline setup will greatly increase the ease of use while minimizing setup time. The motorized CHESS XZ stages that make up the gantry and position the two sets of slits will be replaced by three specially designed walls for the vacuum chambers, each of which contain a 3-axis translation stage (P108478, Ideal Vacuum Products, Albuquerque, NM). These stages can be driven by small, lightweight motorized linear actuators (TRA series, Newport Corporation, Irvine, CA) that are permanently attached to the walls. This upgrade will make the setup much small, lighter, and portable. It will be possible to assemble everything in advance of the beamtime, saving

valuable experimental time during the experiment. It will also become feasible to perform experiments at other synchrotron sources which may not have readily available motorized XZ stages for incorporation into user assemblies.

CHAPTER 6

CONCLUSION AND FUTURE WORK

The three new methodologies described in this thesis push the limits of small-angle X-ray scattering experiments, allowing data collection from smaller sample volumes, with higher signal to noise, in shorter amounts of time. This opens the door to studying samples that are difficult or expensive to produce in large quantities.

The silicon cryoSAXS sample cells discussed in Chapter 3 allow the measurement of static SAXS data from a couple of microliters of sample, with no observable radiation damage. Further improvements to the sample cells are needed to reduce stresses upon cooling and eliminate fractures. Additionally, chemical compatibility between the samples and cryoprotectants must be explored. An off-line method for diagnosing aggregation issues upon freezing and other unfavorable interactions would increase the probability of a successful cryoSAXS beamtime.

The diffusive mixer and beamline setup presented in Chapter 4 revolutionizes time-resolved SAXS experiments by allowing the use of a larger, stable beam than was previously possible with a continuous flow device. More datasets can be acquired in a shorter amount of time, increasing the efficiency of time-resolved beamtimes. Additionally, the low sample consumption makes this mixer applicable to a wide variety of molecules. The beamline setup, with its single crystal pinhole and guard slit blade, eliminates the need for standard tungsten slits which produce large amounts of background scatter, and which the user may not have the flexibility to configure themselves. In this way, the user gains more control over the beam conditions and experimental setup. In the future, this mixer and associated setup could be used to study a wide variety of interactions between biomolecules and small reactants such as ions. Experiments probing RNA folding in the presence of magnesium are very well suited for this mixer.

Finally, the chaotic advection mixer described in Chapter 5 provides a robust way to study interactions between two larger biomolecules, such as between two proteins or between proteins and nucleic acids. The ability to use an even larger, higher flux beam increases the throughput of this mixer relative to the diffusive device, partially compensating for the higher required sample flow rates. The mixer can effectively mix viscous sucrose solutions for time-resolved contrast variation SAXS. In the future, a modified device with larger sample pathlength will be fabricated for long delay time measurements, minimizing the diffusion of small reactants out into the sheath. The beamline setup will also receive upgrades, discussed above, to make it portable for use at other synchrotrons. Future experiments in collaboration with other Pollack Lab members will study viral capsid assembly, nucleosome core particles, and portions of the spliceosome, among many other interesting and important biological systems.

REFERENCES

[1] N. R. C. (US) C. on R. O. in Biology, “Molecular Structure and Function,” in *Opportunities in Biology*, 1989, pp. 39–76.

[2] J. D. Watson and F. H. C. Crick, “Molecular structure of nucleic aids: A structure for deoxyribose nucleic acid,” *Nature*, vol. 171, no. 4356, pp. 737–738, 1953.

[3] H. M. Berman *et al.*, “The Protein Data Bank.,” *Nucleic Acids Res.*, vol. 28, no. 1, pp. 235–242, 2000.

[4] M. Egli, “Diffraction Techniques in Structural Biology,” *Curr. Protoc. Nucleic Acid Chem.*, vol. 41, p. 7.13.1-7.13.35, 2010.

[5] E. F. Garman, “Developments in X-ray Crystallographic Structure Determination of Biological Macromolecules,” *Science*, vol. 343, pp. 1102–1108, 2014.

[6] M. Schüler *et al.*, “Structure of the ribosome-bound cricket paralysis virus IRES RNA,” *Nat. Struct. Mol. Biol.*, vol. 13, no. 12, pp. 1092–1096, 2006.

[7] S. Jonic and C. Vénien-Bryan, “Protein structure determination by electron cryo-microscopy,” *Curr. Opin. Pharmacol.*, vol. 9, pp. 636–642, 2009.

[8] P. R. L. Markwick, T. Malliavin, and M. Nilges, “Structural Biology by NMR: Structure, Dynamics, and Interactions,” *PLoS Comput. Biol.*, vol. 4, no. 9, p. e1000168, 2008.

[9] H. D. T. Mertens and D. I. Svergun, “Combining NMR and small angle X-ray scattering for the study of biomolecular structure and dynamics,” *Arch. Biochem. Biophys.*, vol. 628, pp. 33–41, 2017.

[10] D. Marion, “An Introduction to Biological NMR Spectroscopy,” *Mol. Cell. Proteomics*, vol. 12, pp. 3006–3025, 2013.

[11] D. I. Svergun and M. H. J. Koch, “Small-angle scattering studies of biological macromolecules in solution,” *Rep. Prog. Phys.*, vol. 66, pp. 1735–1782, 2003.

[12] A. G. Kikhney and D. I. Svergun, “A practical guide to small angle X-ray scattering (SAXS) of flexible and intrinsically disordered proteins,” *FEBS Lett.*, vol. 589, pp. 2570–2577, 2015.

[13] E. E. Lattman, “Small angle scattering studies of protein folding,” *Curr. Opin. Struct. Biol.*, vol. 4, pp. 87–92, 1994.

[14] L. Pollack, “SAXS studies of ion-nucleic acid interactions.,” *Annu. Rev. Biophys.*, vol. 40, pp. 225–242, Jan. 2011.

[15] L. Pollack *et al.*, “Compactness of the denatured state of a fast-folding protein measured by submillisecond small-angle x-ray scattering,” *Proc. Natl. Acad. Sci.*, vol. 96, pp. 10115–10117, 1999.

[16] L. Pollack *et al.*, “Time Resolved Collapse of a Folding Protein Observed with Small Angle X-Ray Scattering,” *Phys. Rev. Lett.*, vol. 86, no. 21, pp. 4962–4965, 2001.

[17] L. Pollack, “Time resolved SAXS and RNA folding.,” *Biopolymers*, vol. 95, no. 8, pp. 543–549, 2011.

[18] S. Kuwamoto, S. Akiyama, and T. Fujisawa, “Radiation damage to a protein solution, detected by synchrotron X-ray small-angle scattering: dose-related considerations and suppression by cryoprotectants.,” *J. Synchrotron Rad.*, vol. 11, pp. 462–468, 2004.

[19] S. S. Nielsen, M. Møller, and R. E. Gillilan, “High-throughput biological small-angle X-ray scattering with a robotically loaded capillary cell.,” *J. Appl. Cryst.*, vol. 45, pp. 213–223, 2012.

[20] I. Grillo, “Applications of stopped-flow in SAXS and SANS,” *Curr. Opin. Colloid Interface Sci.*, vol. 14, no. 6, pp. 402–408, 2009.

[21] D. K. Putnam, E. W. Lowe, and J. Meiler, “Reconstruction of Saxs Profiles From Protein Structures,” *Comput. Struct. Biotechnol. J.*, vol. 8, no. 11, p. e201308006, 2013.

[22] A. Bergmann, D. Orthaber, G. Scherf, and O. Glatter, “Improvement of SAXS measurements on Kratky slit systems by Gobel mirrors and imaging-plate detectors,” *J. Appl. Cryst.*, vol. 33, pp. 869–875, 2000.

[23] L. K. Bruetzel *et al.*, “A Mo-anode-based in-house source for small-angle X-ray scattering measurements of biological macromolecules A Mo-anode-based in-house source for small-angle X-ray scattering measurements of biological macromolecules,” *Rev. Sci. Instrum.*, vol. 87, p. 25103, 2016.

[24] R. Fischetti *et al.*, “The BioCat undulator beamline 18ID: A facility for biological non-crystalline diffraction and X-ray absorption spectroscopy at the Advanced Photon Source,” *J. Synchrotron Rad.*, vol. 11, pp. 399–405, 2004.

[25] P. Pernot *et al.*, “Upgraded ESRF BM29 beamline for SAXS on macromolecules in solution,” *J. Synchrotron Rad.*, vol. 20, pp. 660–664, 2013.

[26] J. S. Pedersen, “A flux- and background-optimized version of the NanoSTAR small-angle X-ray scattering camera for solution scattering,” *J. Appl. Cryst.*, vol. 37, pp. 369–380, 2004.

[27] M. A. Graewert and D. I. Svergun, “Impact and progress in small and wide angle X-ray scattering (SAXS and WAXS).,” *Curr. Opin. Struct. Biol.*, vol. 23, pp. 748–754, 2013.

[28] Y. Li, R. Beck, T. Huang, M. C. Choi, and M. Divinagracia, “Scatterless hybrid metal-single-crystal slit for small-angle X-ray scattering and high-resolution X-ray diffraction,” *J. Appl. Cryst.*, vol. 41, pp. 1134–1139, 2008.

[29] C. Cantor and P. Schmimel, *Biophysical Chemistry Part II: Techniques for the study of biological structure and function*. New York: W. H. Freeman and Company, 1980.

[30] R. Welty and K. B. Hall, “Nucleobases undergo dynamic rearrangements during RNA tertiary folding,” *J. Mol. Biol.*, vol. 428, no. 22, pp. 4490–4502, 2016.

[31] D. A. Jacques and J. Trewhella, “Small-angle scattering for structural biology - Expanding the frontier while avoiding the pitfalls,” *Protein Sci.*, vol. 19, pp. 642–657, 2010.

[32] D. Eliezer, K. Chiba, H. Tsuruta, S. Doniach, K. O. Hodgson, and H. Kihara, “Evidence of an associative intermediate on the myoglobin refolding pathway,” *Biophys. J.*, vol. 65, pp. 912–917, 1993.

[33] R. Das *et al.*, “The fastest global events in RNA folding: Electrostatic relaxation and tertiary collapse of the tetrahymena ribozyme,” *J. Mol. Biol.*, vol. 332, pp. 311–319, 2003.

[34] J. Lipfert and S. Doniach, “Small-angle X-ray scattering from RNA, proteins, and protein complexes.,” *Annu. Rev. Biophys. Biomol. Struct.*, vol. 36, pp. 307–327, 2007.

[35] H. B. Stuhrmann, “Interpretation of small-angle scattering functions of dilute solutions and gases. A representation of the structures related to a one-particle-scattering function,” *Acta Cryst.*, vol. A26, pp. 297–306, 1970.

[36] P. Chacón, F. Morán, J. F. Díaz, E. Pantos, and J. M. Andreu, “Low-resolution structures of proteins in solution retrieved from x-ray scattering with a genetic algorithm,” *Biophys. J.*, vol. 74, pp. 2760–2775, 1998.

[37] P. Chacón, J. F. Díaz, F. Morán, and J. M. Andreu, “Reconstruction of protein form with X-ray solution scattering and a genetic algorithm.,” *J. Mol. Biol.*, vol. 299, no. 5, pp. 1289–1302, 2000.

[38] D. I. Svergun, “Restoring Low Resolution Structure of Biological Macromolecules from Solution Scattering Using Simulated Annealing,” *Biophys. J.*, vol. 76, pp. 2879–2886, 1999.

[39] D. Franke and D. I. Svergun, “DAMMIF, a program for rapid ab-initio shape determination in small-angle scattering,” *J. Appl. Cryst.*, vol. 42, pp. 342–346, 2009.

[40] H. L. Carrell, H. Hoier, and J. P. Glusker, “Modes of binding substrates and their analogues to the enzyme D-xylose isomerase,” *Acta Cryst.*, vol. D50, pp. 113–123, 1994.

[41] J. B. Hopkins*, A. M. Katz*, S. P. Meisburger, M. a. Warkentin, R. E. Thorne, and L. Pollack, “A microfabricated fixed path length silicon sample holder improves background subtraction for cryoSAXS,” *J. Appl. Cryst.*, vol. 48, pp. 227–237, 2015. (* co-first authors)

[42] J. Lamb and L. W. Kwok, “Reconstructing Three-Dimensional Shape Envelopes from Time-Resolved Small-Angle X-Ray Scattering Data Reconstructing Three-Dimensional Shape Envelopes from Time-,” vol. 41, pp. 1046–1052, 2008.

[43] D. Svergun, C. Barberato, and M. H. Koch, “CRYSOL - A program to evaluate X-ray solution scattering of biological macromolecules from atomic coordinates,” *J. Appl. Cryst.*, vol. 28, pp. 768–773, 1995.

[44] P. Bernadó, E. Mylonas, M. V. Petoukhov, M. Blackledge, and D. I. Svergun, “Structural characterization of flexible proteins using small-angle X-ray scattering,” *J. Am. Chem. Soc.*, vol. 129, pp. 5656–5664, 2007.

[45] S. P. Meisburger *et al.*, “Breaking the radiation damage limit with Cryo-SAXS.,” *Biophys. J.*, vol. 104, no. 1, pp. 227–236, 2013.

[46] C. M. Jeffries, M. A. Graewert, D. I. Svergun, and C. E. Blanchet, “Limiting radiation damage for high-brilliance biological solution scattering: Practical experience at the EMBL P12 beamline PETRAIII,” *J. Synchrotron Rad.*, vol. 22, pp. 273–279, 2015.

[47] W. M. Garrison, “Reaction Mechanisms in the Radiolysis of Peptides, Polypeptides, and Proteins,” *Chem. Rev.*, vol. 87, pp. 381–398, 1987.

[48] J. B. Hopkins and R. E. Thorne, “Quantifying radiation damage in biomolecular small-angle X-ray scattering,” *J. Appl. Cryst.*, vol. 49, pp. 880–890, 2016.

[49] A. Martel, P. Liu, T. M. Weiss, M. Niebuhr, and H. Tsuruta, “An integrated high-throughput data acquisition system for biological solution X-ray scattering studies.,” *J. Synchrotron Rad.*, vol. 19, pp. 431–434, 2012.

[50] X. Hong and Q. Hao, “Measurements of accurate x-ray scattering data of protein solutions using small stationary sample cells,” *Rev. Sci. Instrum.*, vol. 80, p. 14303, 2009.

[51] L. Pollack and S. Doniach, “Time-Resolved X-ray Scattering and RNA Folding,” *Methods Enzymol.*, vol. 469, pp. 253–268, 2009.

[52] R. Graceffa *et al.*, “Sub-millisecond time-resolved SAXS using a continuous-flow mixer and X-ray microbeam,” *J. Synchrotron Rad.*, vol. 20, pp. 820–825, 2013.

[53] E. F. Garman, “Radiation damage in macromolecular crystallography: What is it and why do we care?,” *Acta Cryst.*, vol. D66, pp. 339–351, 2010.

[54] M. Karuppasamy, F. Karimi Nejadasl, M. Vulovic, A. J. Koster, and R. B. G. Ravelli, “Radiation damage in single-particle cryo-electron microscopy: effects of dose and dose rate,” *J. Synchrotron Rad.*, vol. 18, pp. 398–412, 2011.

[55] R. J. Southworth-Davies, M. A. Medina, I. Carmichael, and E. F. Garman, “Observation of Decreased Radiation Damage at Higher Dose Rates in Room Temperature Protein Crystallography,” *Structure*, vol. 15, pp. 1531–1541, 2007.

[56] M. H. B. J. Kam, Z; Koch, “Fluctuation x-ray scattering from biological particles in frozen solution by using synchrotron radiation,” *Proc. Natl. Acad. Sci. U. S. A.*, vol. 78, no. 6, pp. 3559–3562, 1981.

[57] H. Iwamoto, “Quality evaluation of quick-frozen biological specimens by simultaneous microbeam SAXS/WAXS recordings.,” *J. Synchrotron Rad.*, vol. 16, pp. 336–345, 2009.

[58] A. Fowler and M. Toner, “Cryo-injury and biopreservation.,” *Ann. N. Y. Acad. Sci.*, vol. 1066, pp. 119–135, 2005.

[59] B. Wu, A. Kumar, and S. Pamarthy, “High aspect ratio silicon etch: A review,” *J. Appl. Phys.*, vol. 108, p. 51101, 2010.

[60] K. E. Bean, “Anisotropic Etching of Silicon,” *IEEE Trans. Electron Devices*, vol. ED-25, no. 10, pp. 1185–1193, 1978.

[61] A. Holke and H. T. Henderson, “Ultra-deep anisotropic etching of (110) silicon,” *J. Micromech. Microeng.*, vol. 9, pp. 51–57, 1999.

[62] V. Dwivedi, R. Gopal, and S. Ahmad, “Fabrication of very smooth walls and bottoms of silicon microchannels for heat dissipation of semiconductor devices,” *Microelectron. J.*, vol. 31, pp. 405–410, 2000.

[63] Y. Ezoe *et al.*, “Micropore x-ray optics using anisotropic wet etching of (110) silicon wafers.,” *Appl. Opt.*, vol. 45, no. 35, pp. 8932–8938, 2006.

[64] G. Kaminsky, “Micromachining of silicon mechanical structures,” *J. Vac. Sci. Technol. B*, vol. 3, no. 4, pp. 1015–1024, 1985.

[65] B. Kim and D. D. Cho, “Aqueous KOH Etching of Silicon (110): Etch Characteristics and Compensation Methods for Convex Corners,” *J. Electrochem. Soc.*, vol. 145, no. 7, pp. 2499–2508, 1998.

[66] P. Pal, K. Sato, and H. Hida, “MEMS components with perfectly protected edges and corners in Si{110} wafers,” in *2011 International Symposium on Micro-NanoMechatronics and Human Science*, 2011, pp. 55–59.

[67] W. Kern and J. E. Soc, “The Evolution of Silicon Wafer Cleaning Technology,” *J. Electrochem. Soc.*, vol. 137, no. 6, pp. 1887–1892, 1990.

[68] T. C. Huang, H. Toraya, T. N. Blanton, and Y. Wu, “X-ray powder diffraction analysis of silver behenate, a possible low-angle diffraction standard,” *J. Appl. Cryst.*, vol. 26, pp. 180–184, 1993.

[69] W. F. Rall, “Factors Affecting the Survival of Mouse Embryos Cryopreserved by Vitrification,” *Cryobiology*, vol. 24, pp. 387–402, 1987.

[70] G. M. Fahy, D. R. MacFarlane, C. A. Angell, and H. T. Meryman, “Vitrification as an Approach to Cryopreservation,” *Cryobiology*, vol. 21, pp. 407–426, 1984.

[71] Y. Rabin, P. S. Steif, K. C. Hess, J. L. Jimenez-Rios, and M. C. Palastro, “Fracture formation in vitrified thin films of cryoprotectants.,” *Cryobiology*, vol. 53, pp. 75–95, 2006.

[72] S. Yavin and A. Arav, “Measurement of essential physical properties of vitrification solutions.,” *Theriogenology*, vol. 67, pp. 81–89, 2007.

[73] C. U. Kim, R. Kapfer, and S. M. Gruner, “High-pressure cooling of protein crystals without cryoprotectants,” *Acta Cryst.*, vol. D61, pp. 881–890, 2005.

[74] J. Knight, A. Vishwanath, J. Brody, and R. Austin, “Hydrodynamic Focusing on a Silicon Chip: Mixing Nanoliters in Microseconds,” *Phys. Rev. Lett.*, vol. 80, no. 17, pp. 3863–3866, 1998.

[75] H. Y. Park *et al.*, “Achieving uniform mixing in a microfluidic device: hydrodynamic focusing prior to mixing.,” *Anal. Chem.*, vol. 78, pp. 4465–4473, 2006.

[76] G. D. Calvey, A. M. Katz, C. B. Schaffer, and L. Pollack, “Mixing injector enables time-resolved crystallography with high hit rate at X-ray free electron lasers,” *Struct. Dyn.*, vol. 3, p. 54301, 2016.

[77] A. Plumridge*, A. M. Katz*, G. D. Calvey*, R. Elber, and S. Kirmizialtin, “Revealing the distinct folding phases of an RNA three-helix junction,” *Nucleic Acids Res.*, p. gky363, 2018. (* co-first authors)

[78] D. G. Miller, J. A. Rard, L. B. Eppstein, and J. G. Albright, “Mutual Diffusion Coefficients and Ionic Transport Coefficients Iij of MgCl-H2O at 25 C,” *J. Phys. Chem*, vol. 88, no. 23, pp. 5739–5748, 1984.

[79] Y.-H. Li and S. Gregory, “Diffusion of ions in sea water and in deep-sea sediments,” *Geochim. Cosmochim. Acta*, vol. 38, pp. 708–714, 1974.

[80] M. Young, P. Carroad, and R. Bell, “Estimation of diffusion coefficients of proteins,” *Biotechnol. Bioeng.*, vol. 22, pp. 947–955, 1980.

[81] R. Zwanzig, “On the relation between self-diffusion and viscosity of liquids,” *J. Chem. Phys.*, vol. 79, no. 9, pp. 4507–4508, 1983.

[82] Y. Chen *et al.*, “Revealing transient structures of nucleosomes as DNA unwinds,” *Nucleic Acids Res.*, vol. 42, no. 13, pp. 8767–8776, 2014.

[83] Y. Chen *et al.*, “Asymmetric unwrapping of nucleosomal DNA propagates asymmetric opening and dissociation of the histone core,” *Proc. Natl. Acad. Sci.*, vol. 114, no. 2, pp. 334–339, 2017.

[84] S. V Kathuria *et al.*, “Advances in turbulent mixing techniques to study microsecond protein folding reactions,” *Biopolymers*, vol. 99, no. 11, pp. 888–896, 2013.

[85] E. Saatdjian, A. J. S. Rodrigo, and J. P. B. Mota, “On chaotic advection in a static mixer,” *Chem. Eng. J.*, vol. 187, pp. 289–298, 2012.

[86] S. Wiggins and J. M. Ottino, “Foundations of chaotic mixing,” *Phil. Trans. R. Soc. Lond. A.*, vol. 362, no. 1818, pp. 937–970, 2004.

[87] A. Bertsch, S. Heimgartner, P. Cousseau, and P. Renaud, “Static micromixers based on large-scale industrial mixer geometry,” *Lab Chip*, vol. 1, pp. 56–60, 2001.

[88] O. S. Galaktionov, P. D. Anderson, G. W. M. Peters, and H. E. H. Meijer, “Analysis and optimization of Kenics static mixers,” *Int. Polym. Proc.*, vol. 18, no. 2, pp. 138–150, 2003.

[89] D. M. Hobbs and F. J. Muzzio, “The Kenics static mixer: A three-dimensional chaotic flow,” *Chem. Eng. J.*, vol. 67, pp. 153–166, 1997.

[90] E. S. Szalai and F. J. Muzzio, “Fundamental Approach to the Design and Optimization of Static Mixers,” *AIChE J.*, vol. 49, no. 11, pp. 2687–2699, 2003.

[91] S. Maruo, O. Nakamura, and S. Kawata, “Three-dimensional microfabrication with two-photon-absorbed photopolymerization,” *Opt. Lett.*, vol. 22, no. 2, pp. 132–134, 1997.

[92] K. S. Lee, D. Y. Yang, S. H. Park, and R. H. Kim, “Recent developments in the use of two-photon polymerization in precise 2D and 3D microfabrications,” *Polym. Adv. Technol.*, vol. 17, pp. 72–82, 2006.

[93] F. Niesler and M. Hermatschweiler, “Two-Photon Polymerization - A Versatile Microfabrication Tool,” *Laser Tech. J.*, vol. 3, pp. 44–47, 2015.

[94] F. Niesler and M. Hermatschweiler, “Additive Manufacturing of Micro-sized Parts Trend of miniaturization is driver for 3D laser lithography,” *Laser Tech. J.*, vol. 5, pp. 16–18, 2014.

[95] Q. S. Hanley, V. Subramaniam, D. J. Arndt-Jovin, and T. M. Jovin, “Fluorescence Lifetime Imaging: Multi-point Calibration, Minimum Resolvable Differences, and Artifact Suppression,” *Cytometry*, vol. 43, pp. 248–260, 2001.

[96] M. Marquart, J. Walter, J. Deisenhofer, W. Bode, and R. Huber, “The geometry of the reactive site and of the peptide groups in trypsin, trypsinogen and its complexes with inhibitors,” *Acta Cryst.*, vol. B39, pp. 480–490, 1983.

[97] T. Vajda and A. Garai, “Comparison of the effect of calcium(II) and manganese(II) ions on trypsin autolysis,” *J. Inorg. Biochem.*, vol. 15, pp. 307–315, 1981.

[98] “The PyMOL Molecular Graphics System.” Schrodinger, LLC.

[99] K. Kawamura *et al.*, “X-ray and neutron protein crystallographic analysis of the trypsin-BPTI complex,” *Acta Cryst.*, vol. D67, pp. 140–148, 2011.

[100] S. S. Nielsen *et al.*, “BioXTAS RAW , a software program for high-throughput automated small-angle X-ray scattering data reduction and preliminary analysis,” *J. Appl. Cryst.*, vol. 42, pp. 959–964, 2009.